Final work : Structural modeling of propeller for multi-disciplinary design optimization

Auteur : Sharma, Manthan
Promoteur(s) : Hillewaert, Koen
Faculté : Faculté des Sciences appliquées
Diplôme : Master en ingénieur civil en aérospatiale, à finalité spécialisée en "turbomachinery aeromechanics (THRUST)"
Année académique : 2021-2022
URI/URL : https://www.tudelft.nl/lr/appu; http://hdl.handle.net/2268.2/15869

THRUST Master of Science, 30 credits

KTH Royal Institute of Technology,
Stockholm, Sweden, 2022.

University of Liege,
Liege, Belgium, 2022.

Academic Year 2021-2022

Master Thesis Report

Structural modeling of propeller for multi-disciplinary design optimization

Final work carried out with a view to obtaining the master's degree "Civil Engineer in Aerospace, specialized in turbomachinery aeromechanics (THRUST)" by Manthan Sharma

University of Liège - Faculty of Applied Sciences

Structural modeling of propeller for multi-disciplinary design optimization

Master Thesis

by

Manthan Sharma

to obtain the degree of Master of Science,
at the University of Liège,
to be defended publicly on Monday September 5, 2022.

Student number: S213917
Project duration: March 1, 2022 – August 30, 2022
Thesis committee:

Dr. ir. T. Sinnige,	TU Delft, Supervisor
Ir. M. van Sluis,	TU Delft, Daily Supervisor
Prof. Dr. K. Hillewaert,	Supervisor, University of Liège
Prof. Dr. G. Dimitriadis,	University of Liège

An electronic version of this thesis is available at `http://matheo.uliege.be/`.

Abstract

Aircraft propellers have been an essential propulsion source since the origins of aviation. In order to allow aviation to continue and remain a viable means of mass transportation, the aircraft of tomorrow should become more energy-efficient, have less greenhouse gas emissions and have a lower noise signature. Due to their high propulsive efficiency and the introduction of electric propulsion in aviation, there is a renewed interest in propeller design. However, conventional propellers are often considered noisy compared to turbofan engines. On top of that, further propulsion integration into the air-frame, for instance, Boundary Layer Ingestion, results in additional sources of propeller noise due to increased non-uniform inflow. In order to meet the challenges mentioned and develop novel energy-efficient propellers with a low acoustic footprint, a multi-disciplinary framework is being developed to optimize the propeller design. Present work focuses on the structural analysis of the propeller blade in a steady rectilinear flight operation to predict the blade stresses and ensure that the optimized blade can withstand the aerodynamic and centrifugal loads.

The structural model is based on the Euler-Bernoulli beam theory for bending loads and the Saint-Venant theory for torsional loads in the blade. The proposed low-level structural model is more robust, fast, and efficient in terms of computational time and power than structural FEM simulations and can thus be easily integrated into a multi-disciplinary design optimization framework, including aerodynamics and aeroacoustics. The model is sensitive to changes in the blade's planform (chord, twist, and sweep) and airfoil geometry. In addition, to build confidence in the results the low-fidelity model was validated against high-fidelity structural (Fluid-Structure interaction) simulations of the propellers in both propulsive and regenerative regimes.

The sensitivity analysis was performed using various geometrical and operational parameters such as advance ratio, propeller pitch, and blade sweep. Expected outcomes from the sensitivity study were achieved, concluding that the centrifugal loads dominates over aerodynamic loads, and further consolidating the structural model and demonstrating that the low-level model performs satisfactorily in estimating the stress distribution. The proposed structural model serves as the foundation for aeroelastic analysis, which includes unsteady aerodynamic loadings, which were not considered in the current work.

Keywords: Propellers, Low-fidelity, Structures, Swept blades, FEM, design optimization

Acknowledgments

The development of the research project and submission of the thesis report finishes the two year-long THRUST masters. This program gave me an international experience at KTH University (Sweden) and University of Liège (Belgium) during the studies and the development of the thesis at Technical University of Delft (Netherlands).

I'd want to express my gratitude to Dr. Tomas Sinnige and Martijn van Sluis for accepting me into the Flight Propulsion and Performance research group, and being my supervisors at TU Delft. I'd also want to thank Jatinder Goyal, Dr. Jurij Sodja, and Dr. Gabriel Margalida from the research group for their technical advice and useful input. Finally, thanks to my friends and new acquaintances at TU Delft that I met during my research and who made everything engaging and fun.

I'd also want to thank Professor Hillewaert Koen and Professor Grigorios Dimitriadis from University of Liege for being my supervisors. They were very interested in it from the start and made all of their facilities and materials available to help me out with research topic.

Special gratitude to my parents, family, and closest friends for their emotional and psychological support during the difficult times. Finally, I'd want to thank all of my THRUST classmates (Prachurjya, Teja, Alexandre, Cèsar, Lucía, and Jorge) for the last two years. They had been fantastic colleagues during my master's program in Stockholm and Liège, and it was wonderful to have them in that intense experience.

Manthan Sharma
Delft, August 2022

Contents

1 Introduction **1**
- 1.1 Thesis Aim and Objectives . . . 4
- 1.2 Stakeholders . . . 4
- 1.3 Outline . . . 4

2 Background of propeller aerodynamics and structures **7**
- 2.1 Terms and definitions . . . 7
- 2.2 Propeller Aerodynamics . . . 8
  - 2.2.1 Propeller Blade Loadings . . . 8
  - 2.2.2 Aerodynamic Performance Indicators . . . 9
- 2.3 BEM Model . . . 11
  - 2.3.1 General Theory . . . 11
- 2.4 BEM model Implementation . . . 12
- 2.5 Sweep in the propeller blades . . . 15
- 2.6 Propeller Structural Module . . . 16
  - 2.6.1 Previous Structural Studies . . . 16

3 Structural Analysis of Propeller Blade **21**
- 3.1 Assumptions of the structural model . . . 21
- 3.2 Cross-sectional Mechanical Properties . . . 22
- 3.3 Torsional Stress evaluation . . . 22
  - 3.3.1 Rectangular Approximation of Airfoil . . . 22
  - 3.3.2 Numerical Solution to Airfoil : Saint-Venant theory . . . 23
- 3.4 Cantilever Beam Model . . . 27
  - 3.4.1 Aerodynamic Moments . . . 27
  - 3.4.2 Centrifugal Moment . . . 28
  - 3.4.3 Estimation of Stress . . . 29

4 Model Verification and Validations **33**
- 4.1 Propeller Blade Geometry . . . 33
- 4.2 High Fidelity Simulation Setup . . . 35
  - 4.2.1 CFD Simulations . . . 37
  - 4.2.2 Structural Simulation - FEM . . . 38
- 4.3 Low Fidelity Model Verification . . . 41
  - 4.3.1 Propulsive Regime . . . 43
  - 4.3.2 Regenerative Mode . . . 44

5 Sensitivity Study of Structural Performance **49**
- 5.1 Varying Advance Ratio . . . 49
  - 5.1.1 Global and Local Bending Moments . . . 50
  - 5.1.2 Stress Distribution at hub . . . 51
  - 5.1.3 Stress distribution on propeller blades . . . 51
- 5.2 Varying Reference Pitch Angle . . . 53
  - 5.2.1 Global and Local Bending Moments . . . 55
  - 5.2.2 Stress Distribution at Hub . . . 56
  - 5.2.3 Stress distribution on propeller blades . . . 56
- 5.3 Varying Sweep Angle . . . 58
  - 5.3.1 Global and Local Moments . . . 60

6 Conclusions **63**
6.1 Conclusions 63
6.2 Recommendations 64

A Blade Cross sections **69**

B Sensitivity Results Contour plots: Advance Ratio **71**

C Sensitivity Results Contour plots: Propeller Pitch **77**

D Sensitivity Results Contour plots: Blade Sweep **83**

E Post Processing Python Script with TecPlot ® **87**

Nomenclature

Acronyms

BEM	Blade Element Momentum
CFD	Computational Fluid Dynamics
FEM	Finite Element Method
FPP	Flight Performance and Propulsion
FS	Factor of Safety
MCA	Mid Chord Alignment
RANS	Reynolds-Averaged Navier-Stokes

Sub and Superscripts

0	Reference Section
1	Effective
∞	freestream
θ	Tangential Component
$\xi\,\eta,\zeta$	Local Coordinate Axis
ax	axial
$c/4$	Quarter Chord
c	centrifugal Component
cen	Centroid
cp	center of pressure
eq	Equivalent
i	Radial section of propeller
LE	Leading Edge
Q	Torque Component
s	Exit of streamtube
T	Thrust Component
tgt	tangential

Variables

α	Angle of attack
$\bar{u}$	Prandtl's displacement function
β	Pitch Angle of airfoil
ΔV	Change in Velocity
$\dot{m}$	Mass flow rate
η	Propeller Efficiency
η_p	Propulsive Efficiency
Γ	Airfoil Boundary
γ	Blade Sweep Angle
Ω	Rotational Velocity
Φ	Prandtl's stress function
ϕ	Inflow Angle
ρ	Density of Fluid
σ	Axial Stress
τ	Shear Stress
Θ	Angular Displacement
A	Area of cross section
a	Axial Inflow Factor
b	Swirl Inflow Factor
c	Chord Length
C_d	Drag Coefficient
C_l	Lift Coefficient
C_P	Power Coefficient

C_Q	Torque Coefficient
C_T	Thrust Coefficient
D_p	Diameter of the propeller
e	unit vector in local Coordinate
F	Force
G	Shear Modulus of Rigidity
I	Moment of Inertia
I_t	Torsional moment of Inertia
J	Advance Ratio
M	Bending Moment
Ma	Mach Number
N	Vertical Force
n	Angular Frequency
p	Pressure
R	Radius of propeller
Re	Reynolds Number
t	thickness
V	Velocity of fluid
x	Ratio of location of Center of pressure
D	Drag Force
L	Lift Force
Q	Torque Force
r	radial distance of the section
T	Thrust Force

List of Figures

1.1 Propulsive efficiency for different forms of aircraft propulsion[2] . . . 1
1.2 Normalized energy cost of Northwest U.S. electricity versus U.S. Jet A-1[5] . . . 2
1.3 Airbus A400m propeller blades in Paris Airshow, 2009 . . . 3
1.4 Comparison of baseline blade (left) with the other optimum blades (right) by Pagano et al. [10] . . . 3
1.5 Research Outline . . . 5

2.1 Basic Terminology of the propeller blade, adapted from Weick [11] . . . 8
2.2 Propeller blade diagram[12] . . . 8
2.3 Performance Graph - Relation between advance ratio and key aerodynamic performance parameters[13] . . . 10
2.4 Typical Propeller performance and efficiency curves with advance ratios . . . 10
2.5 Velocity triangles of fixed-pitch propeller in propulsive and regenerative mode[12] . . . 11
2.6 Representation of actuator disk theory, showing contracting streamtube and the actuator disk . . . 12
2.7 Blade section at a radius r . . . 13
2.8 Flowchart for BEM model . . . 15
2.9 Definition of mid chord alignment[20] . . . 16
2.10 Maximum Tensile Stresses in the propeller blade, adapted from Weick [11] . . . 17
2.11 Cantilever Beam Model, adapted from Carlton [16] . . . 17
2.12 Stress Distribution with chordwise coordinate at 30% of radial section, adapted from Carlton [16] . . . 18
2.13 Different types of marine propeller used for FEM studies[26] . . . 19

3.1 Rectangle of equivalent geometric properties[29] . . . 23
3.2 Case Example: NACA 2412 . . . 25
3.3 Case Example: NACA 2440 . . . 26
3.4 Location of Center of Pressure[34] . . . 27
3.5 Illustration of the radial vectors originating from aerodynamic and centrifugal forces . . . 29
3.6 Local Coordinate System at radial section r . . . 30
3.7 Hub section ($r = 0.2R$) in Local Coordinate System (LCS) . . . 31
3.8 Solution of ∇u on the airfoil section . . . 32

4.1 Propeller Models[14] . . . 34
4.2 Radial distribution of pitch and chord of XPROP blades . . . 34
4.3 CAD Geometry of XPROP propeller . . . 35
4.4 XPROP blade from the low fidelity model β_0 =20° . . . 36
4.5 XPROP blade from the low fidelity model β_0 =30° . . . 36
4.6 Numerical Domain and Boundary Conditions[14] . . . 37
4.7 CFD Results for XPROP in propulsive regime $J = 1.2$ . . . 38
4.8 CFD Results for XPROP in Regenerative regime ($J = 1.9$) . . . 39
4.9 Imported Loads on the propeller blade . . . 39
4.10 Imported Loads on the propeller blade $J = 1.2$ . . . 40
4.11 Hub Surface mesh . . . 41
4.12 Mesh Independence Study . . . 42
4.13 XPROP converged mesh . . . 42
4.14 Validation Process for the low fidelity structural model . . . 43
4.15 Aerodynamic Load validations for XPROP in propulsive regime . . . 43
4.16 Equivalent von-Mises Stress in Propulsive Regime: Centrifugal Loadings . . . 44

4.17 Equivalent von-Mises Stress in Propulsive Regime: Aerodynamic Loading 45
4.18 Equivalent von-Mises Stress in Propulsive Regime: Combined Loading 45
4.19 Equivalent von-Mises Stress in Regenerative Regime: Centrifugal Loadings 46
4.20 Equivalent von-Mises Stress in Regenerative Regime: Aerodynamic Loading 47
4.21 Equivalent von-Mises Stress in Regenerative Regime: Combined Loading 47

5.1 Variation of maximum von-Mises stress with varying advance ratios 50
5.2 Varying aerodynamic loading with advance ratio 50
5.3 Variation of Global Moments for varying advance ratios 51
5.4 Variation of Local Bending Moments for varying advance ratios 52
5.5 Hub profile in the local Cartesian system 52
5.6 Variation of the von-Mises stress in Local axis with varying advance ratios J 53
5.7 Stress Distribution on the propeller blade with varying advance ratios J 54
5.8 Maximum von-Mises stress on radial sections with varying Reference pitch 55
5.9 Varying aerodynamic loading with propeller pitch 55
5.10 Variation of Global bending moments with propeller pitch 56
5.11 Variation of Local bending moments with propeller pitch 57
5.12 Variation of the hub stress with varying propeller pitch 57
5.13 Stress Distribution on the propeller blade with varying propeller pitch β_0 59
5.14 Maximum von-Mises stress on radial sections with varying Sweep angle 60
5.15 Variation of Global Moments with varied sweep γ_0 60
5.16 Variation of Local Moments with varying sweep $\gamma_0 =$ 61
5.17 Variation of the hub von-Mises stress in Local axis with sweep 61
5.18 Stress Distribution on the propeller blade with varying sweep 62

A.1 Blade cross sections at 25 radial sections of XPROP propeller (untwisted) 70

B.1 von-Mises stress contours with $J = 0.6$ 72
B.2 von-Mises stress contours with $J = 0.7$ 72
B.3 von-Mises stress contours with $J = 0.8$ 73
B.4 von-Mises stress contours with $J = 0.9$ 73
B.5 von-Mises stress contours with $J = 1.0$ 74
B.6 von-Mises stress contours with $J = 1.1$ 74
B.7 von-Mises stress contours with $J = 1.2$ 75

C.1 von-Mises stress contours with $\beta_0 = 15$ 78
C.2 von-Mises stress contours with $\beta_0 = 17.5$ 78
C.3 von-Mises stress contours with $J = 20$ 79
C.4 von-Mises stress contours with $\beta_0 = 22.5$ 79
C.5 von-Mises stress contours with $\beta_0 = 25$ 80
C.6 von-Mises stress contours with $\beta_0 = 27.5$ 80
C.7 von-Mises stress contours with $\beta_0 = 30$ 81

D.1 von-Mises stress contours with $\gamma_0 = 0$ 84
D.2 von-Mises stress contours with $\gamma_0 = 5$ 84
D.3 von-Mises stress contours with $\gamma_0 = 10$ 85
D.4 von-Mises stress contours with $\gamma_0 = 15$ 85
D.5 von-Mises stress contours with $\gamma_0 = 20$ 86
D.6 von-Mises stress contours with $\gamma_0 = 25$ 86

List of Tables

3.1 Mesh Properties of the case example 24

3.2 Solver Properties for the case example 27

3.3 Coefficients for the Poisson's Equation 27

4.1 XPROP: Operating conditions for propulsive and regenerative mode 35

4.2 Material Properties of Structural Steel, ANSYS ® 39

4.3 Mesh Independence Study 41

4.4 Comparison of High-fidelity and low-fidelity maximum stresses 46

5.1 Operating points with varied advance ratio 49

1

Introduction

Aircraft propellers have always been an important part of research since the dawn of aviation. The Wright brothers' successful powered flight in 1903 was made possible by a propeller engine. Propellers became an important source of propulsive devices to power aircraft in the four decades that followed. Turbojet and turbofan engines were invented near the end of World War II. For the majority of passenger aircraft, these continue to be the best source of aircraft propulsion. However, rising fuel prices and increased environmental awareness have increased demand for engines that are more fuel efficient. The high propulsive efficiency of propellers, combined with the introduction of electric propulsion in aviation, sparked renewed interest in propeller design.

Higher propeller efficiencies can be explained using the following equations:

$$T = \dot{m}\Delta V \tag{1.1}$$

$$\eta_p = \frac{2}{2 + \Delta V / V_\infty} \tag{1.2}$$

From the equation 1.1, the thrust force T for the propeller is solely due to change in momentum and, therefore the pressure difference contribution is not required. Equation 1.2, provides the propulsive efficiency η_p, which becomes highest for a small increment in the velocity of accelerated flow. Hence, the highest efficiency is produced with a high mass flow goes through a slight increment in flow velocity, instead of low mass flow rate with high increment of velocity. Consequently, it can be said that a large propeller with a large mass flow rate, leads to a higher propulsive efficiency. Figure 1.1 illustrates the propulsive efficiencies of a turboprops and high bypass turbofan engines. As a result of high potential propulsive efficiency, there has been a renewed rise in the use of turboprops in aviation.[1]

With the increasing awareness towards the environment and the Environmentally Responsible Aviation (ERA) goals proposed by NASA[3] and the European Commission,[4] a shift towards the Electric and Hybrid Propulsion has been observed. In the past decade, aircraft concepts using electricity for

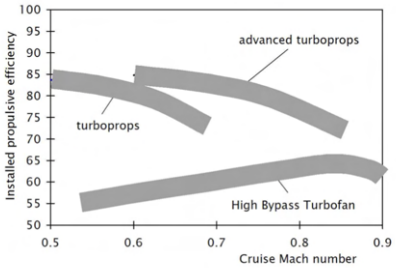

Figure 1.1: Propulsive efficiency for different forms of aircraft propulsion[2]

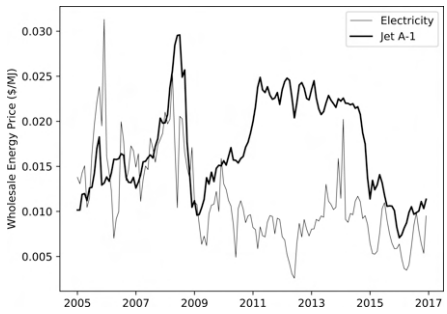

Figure 1.2: Normalized energy cost of Northwest U.S. electricity versus U.S. Jet A-1[5]

some or all of their propulsive power have captured the great attention in the popular press.[5] NASA's Subsonic Fixed Wing program established aggressive goals for energy consumption, nitrogen oxides (NOx), and noise for three generations of airplanes extending out to the 2030s.[6] The benefits of electrification can be broken down into two categories: first, lower operating costs for current missions when compared to conventional aircraft, and second, entirely new capabilities that could lead to the opening of lucrative new markets. The use of electricity instead of jet fuel, a decrease in the amount of energy consumed overall, or lower maintenance costs can all result in lower operating costs. Figure 1.2 shows that, over the last ten years, jet fuel has been more expensive than electricity, though the difference has been less prominent in recent years.

Apart from high propulsive efficiencies, propellers have the unique advantage of being easily scaled and coupled to multiple electric motors on an aircraft. As a result, a propeller can easily power all types of electric and hybrid electric aircraft, such as small passenger planes, drones, or unmanned aerial vehicles (UAV). There are numerous examples of novel electric aircraft concepts available, ranging from distributed propulsion to a single propeller configuration.
The casing and nacelle of a turbofan engine reduce the axial Mach number at rotor, allowing a high flight velocity. Furthermore, the casing also helps to contain noise emissions produced by the entire propulsor. However, propeller blades are not surrounded by a casing, they are subject to freestream velocity, which can result in flight velocity limitations and a significant noise emissions. High Mach numbers at the propeller blade tip cause a large amount of drag, limiting flight speed. To complicate problems, high tip Mach numbers can cause a lot of noise from the propeller. Because there is no casing, direct noise is emitted to the observer. These can cause significant sleep disturbances and other psychological effects in a large number of people. To use a propeller in aircraft propulsion, research is being conducted to mitigate both the cruise speed limitations and extensive noise emissions. Both constraints can be mitigated to some extent by optimizing the propeller blades. Previous researches has shown that propeller noise can be reduced along with maximizing the propeller aerodynamic performances.[7–9] A reduction of noise emissions can be achieved by using advanced blade design methods. Typically, a certain amount of variable blade sweep is incorporated in advanced propeller blade designs, which is both beneficial for reducing noise emissions and for increasing the speed limit of propeller aircraft.[7] Figure 1.3 shows the swept propeller blades used by Airbus A400m aircraft.

Previously, optimization studies with varying objectives, constraints, and aerodynamic/aeroacoustic models were carried out. For each of these optimization studies, an isolated propeller was assumed. The resulting blade geometries in these studies differed in shape due to these differences in approach, emphasizing the importance of accurate numerical models and a well-defined optimization framework. Numerous approaches in numerical model and optimization studies resulted in optimistic results with a optimum propeller blade geometry, with a better aerodynamic performances and a reduction in noise emissions with the help of swept blades in the propellers. Higher-fidelity models draw attention because of their accuracy in computing results. However, using higher-fidelity models in propeller optimization frequently results in high computational times. Pagano et al. [10] used the BEM model coupled with the more advanced CFD model, to optimize the propeller blade with a blade sweep. Figure 1.4 shows the blade geometry of the optimum blade generated by Pagano et al. [10].

Throughout the optimization studies, an attempt is made to find the best propeller design for maximum aeroacoustic and aerodynamic performance. The selection of an aerodynamic and aeroacoustic

Figure 1.3: Airbus A400m propeller blades in Paris Airshow, 2009

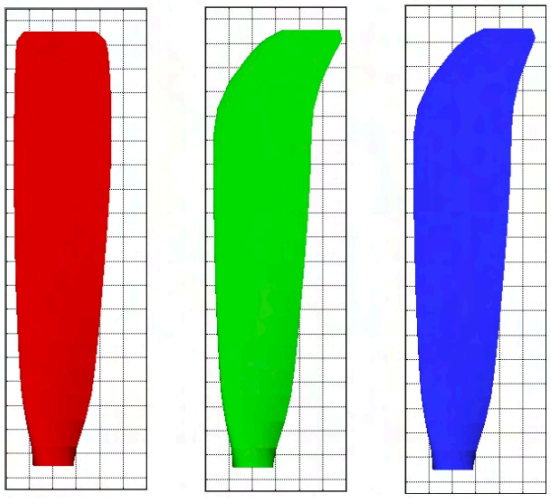

Figure 1.4: Comparison of baseline blade (left) with the other optimum blades (right) by Pagano et al. [10]

model is critical for generating the best blade geometry. However, in addition to the aerodynamic and aeroacoustic models, the coupling of structural models is critical to ensure blade stability and that the blade can withstand the high centrifugal and aerodynamic loadings of the propeller. To generate thrust, the propeller is operated at extremely high rotational speeds, can go up to 30000 RPM depending upon the size and diameter of the propeller; therefore, it is critical to ensure that the blade is capable of sustaining such high loads; otherwise, the propeller blade may experience structural failure, resulting in a catastrophic flight operation. The optimum blade generated in figure 1.4 can be used to demonstrate why a structural model must be coupled with aerodynamic and aeroacoustic optimization. Optimal blades have a sudden increase in sweep angles towards the tip, which can result in a stress concentration zone where the blade sweep begins. If the propeller is operated at a higher rotational speed, the maximum stress in the stress concentration zone can exceed the allowable maximum stress of the material, resulting in crack initiation in the propeller structure and, eventually, structural failure of blade. In this thesis, a low fidelity structural model is proposed that, along with the aerodynamic and aeroacoustic models, can be employed later in optimization studies to generate optimal swept blades that can operate in the required range. A low fidelity structural model can predict maximum stress during flight operation while using limited processing time and power, and it can be easily coupled with other optimization studies such as aerodynamic and aeroacoustic models. Before using low-order methods in optimization studies, a rigorous verification procedure is required to build confidence in these models. It is possible to obtain high fidelity structural results by using a verification method that combines CFD and FEM propeller results, and it is possible to determine whether these low order numerical tools are suitable for use in optimization studies. As a result, design advancements may make the propeller more appealing as a propulsion device for an all-electric aircraft, drone, or a turboprop.

1.1. Thesis Aim and Objectives

As previously discussed, changing the blade planform: chord, blade sweep, twist, and airfoil geometry is a promising design step for reducing propeller noise and emissions. However, in order to ensure the design safety of blades, a structural model must be included in the optimizations. As a result, the primary goal of this thesis is stated as follows:
" To built a low-fidelity structural model of the propeller mechanical loadings to be used in an optimization study."
The objectives of the thesis is summarized as follows:

- To establish a methodology for developing a low fidelity structural model based on analytical equations to evaluate stress variations in an isolated propeller blade.
- To evaluate and compare the stress distribution on the propeller blade caused by aerodynamic and centrifugal loadings.
- To determine the effect of the propeller blade's sweep, pitch angle and advance ratio on the stress developing on the blade.
- To validate and compare the results of the given low fidelity analytical model with the high fidelity FEM software.

1.2. Stakeholders

The present thesis is done in coordination with the Flight Propulsion and Performance (FPP) research group in the Faculty of Aerospace Engineering at Technical University of Delft. The thesis is part of the project conducted within the framework of the research project APPU (Advanced Propulsion and Power Unit).

1.3. Outline

The thesis report is divided into four parts, as shown in the figure 1.5. Part I covers the introduction in Chapter 1 and background theory on propeller aerodynamics and structural module including the influence of sweep on the propeller blades in the chapter 2. Then, part II discusses the methodology and structural model proposed for the analysis in Chapter 3 This part is largely based upon the literature study in the preparation of this thesis. In the part III, verification and validations are first presented in the

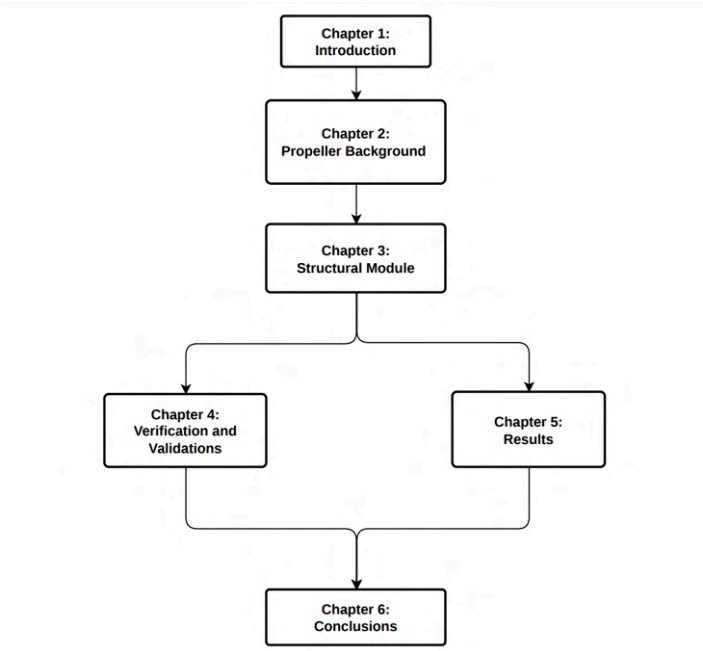

Figure 1.5: Research Outline

chapter 4, and the sensitivity study results by varying physical parameters are presented in the chapter 5. Finally in the part IV, this thesis is concluded in the chapter 6, in which conclusions, recommendations and scope of future studies are stated.

In addition to the main results, some of the results which eventually did not contributed to the research are also presented in the Appendix. These results can be used as a reference for future work.

2

Background of propeller aerodynamics and structures

In this chapter, some basics of the propeller aerodynamics, performance and structural analysis are provided, and past studies are shortly discussed. The basics of the propeller are discussed in section 2.1. Aerodynamics and flow over the propeller are discussed in section 2.2, while more discussions on the structural investigations and previous studies are provided in the section 2.6.

2.1. Terms and definitions

A propeller is a device for providing a force or thrust, at the expense of power generated by a motor, for driving a craft of some type through a fluid medium, such as air or water. In order to provide this thrust, the propeller must set a mass of the fluid in motion in a direction opposite to that of the craft being propelled.[11] The force which drives the aircraft forward, is the reaction obtained due to certain mass of air pushed backwards by the propeller. This backward moving air is called as slip-stream and it has a certain kinetic energy due to its motion which represents a loss. Other losses includes loss due to friction of air on the blade surface, and hence, the thrust power developed by the propeller is always lower than the power delivered by the engine/motor to the propeller. The ratio of the power transferred as thrust to the power developed by the engine is the propulsive efficiency and it is the most important goal of the propeller design to obtain a high propulsive efficiency. Before moving forward into in depth analysis of the propeller blade, it is necessary to know the basic terminology of the propeller blades. Figure 2.1 helps to explain the terms used for the propeller blades.

1. Diameter (D) Diameter of the circle swept by the blade tips.
2. Pitch (p) This refers to the advancement in a single revolution of the propeller. A propeller since it operates in the fluid, can have different airspeed, hence, pitch is usually not fixed. However, advancement per revolution is the fundamental importance and is known as the effective pitch.
3. Boss of the propeller is central part of propeller where hub is mounted.
4. Hub is the metal fitting inserted to the propeller which helps in mounting the blade to the shaft
5. Root of the blade is part of the blade near the hub.
6. Aspect Ratio is the radius of the tip of the blade, with the maximum width of the blade.
7. **Pitch Angle** (β) The acute angle between the chord of the propeller cross section and a plane perpendicular to the axis of rotation of the propeller.
8. Rake or Tilt of the propeller blade is defined as the mean angle which the line joining the centers of area of the sections makes with a plane perpendicular to the axis of rotation.

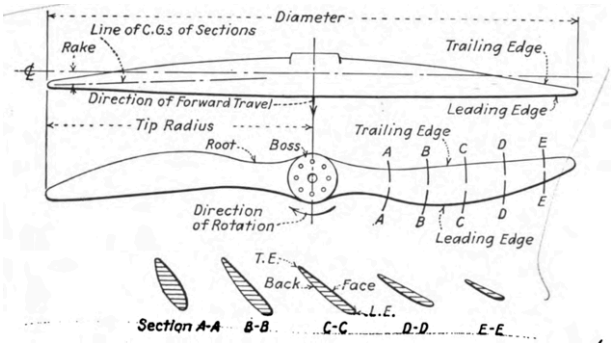

Figure 2.1: Basic Terminology of the propeller blade, adapted from Weick [11]

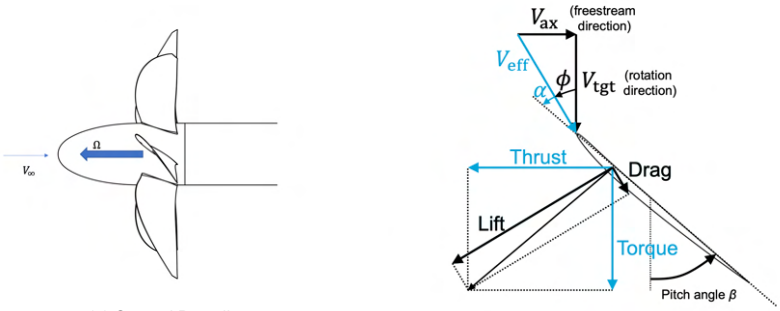

(a) General Propeller

(b) 2D blade section at radial distance r

Figure 2.2: Propeller blade diagram[12]

2.2. Propeller Aerodynamics

Main objective of a propeller in the aircraft is to provide a force, which can be thrust to fly an aircraft or lift to operate a drone for example. A propeller should operate at the highest propulsive efficiency, i.e. a propeller should be able to produce a maximum amount of force while using the least power input. In this section, the mechanisms of generating the thrust forces and key performance parameters are discussed.

2.2.1. Propeller Blade Loadings

Thrust is generated by a set of propeller blades, each blade can be considered as a lifting surface which provides the lift and drag to the body. In the figure 2.2, a 2D blade section of a propeller at a radial distance r is depicted. The propeller experience a combination of translation (due to the wind speed) and rotation, as a consequence propeller blade experiences an angle of attack α, from the airflow, which ultimately results in Lift and Drag forces on the section of blade. The thrust and torque forces on the blade are the consequences of the Lift and Drag forces, on the propeller blade sections.

Velocity triangle can also be observed in the figure 2.2, where V_{ax} is the axial or freestream velocity and V_{tgt} is the tangential or rotational velocity in the direction of rotation of the blade. The angle between the axial and the tangential velocity is known as inflow angle and is denoted as ϕ. The difference between the pitch angle (β) and the inflow angle (ϕ) is the angle of attack (α) of the blade section. Due to the angle of attack of flow and airfoil as a lifting surface, Lift (dL) and Drag forces (dD) are generated, which in turn, generated Thrust(dT) and Torque(dQ) forces.

Equation 2.10 gives relations from the velocity triangle in a 2D blade section of a propeller blade.

$$\begin{aligned} V_{\text{eff}} &= \sqrt{V_{\text{ax}}^2 + V_{\text{tgt}}^2} \\ \phi &= \tan^{-1}\left(\frac{V_{\text{ax}}}{V_{\text{tgt}}}\right) \\ \alpha &= \beta - \phi \end{aligned} \tag{2.1}$$

Thrust and Torque can be related to the lift and drag forces, with the relations 2.11

$$\begin{aligned} \mathrm{d}L &= \frac{1}{2}\rho V_{\text{eff}}^2 C_l(\alpha, Re, Ma)c \\ \mathrm{d}D &= \frac{1}{2}\rho V_{\text{eff}}^2 C_d(\alpha, Re, Ma)c \\ dT &= dL\cos\phi - dD\sin\phi \\ dQ &= (dL\sin\phi + dD\cos\phi)r \end{aligned} \tag{2.2}$$

In 3D representation of the blade, loading of the entire blade along the radius is considered. As the blade is rotating about the center, the local rotational velocity of the blade increases with radial coordinate. Point of maximum loading of propeller blade is generally at around 70% of the radius, dependent on the operating conditions and propeller geometry.

2.2.2. Aerodynamic Performance Indicators

The key Aerodynamic performance indicators includes propulsive power, shaft power and the propeller efficiency. These parameters represents the output power, input power and the efficiency of the propeller. The blade pitch angle β along with the operating conditions determines the performance parameters. The operating conditions of the propeller is determined using advance ratio (J) of the propeller with D as the diameter, V_∞ as the freestream velocity and n denoting the angular frequency of rotation of propeller.

$$J = \frac{V_\infty}{nD} \tag{2.3}$$

For a given blade pitch β, the advance ratio is a scalable variable for which the performance parameters of the propeller can be defined. These key parameters are usually defined in the non dimensionalized forms, which are as shown in the equations 2.4 - 2.7. The thrust and power are non-dimensionalized with respect to the dynamic pressure relative to the tip speed of propeller.

$$C_T = \frac{T}{\rho_\infty n^2 D^4} \tag{2.4}$$

$$C_Q = \frac{Q}{\rho_\infty n^2 D^5} \tag{2.5}$$

$$C_P = 2\pi C_Q \tag{2.6}$$

$$\eta = J\frac{C_T}{C_P} \tag{2.7}$$

However, in the case of optimization studies, Thrust is non dimensionalized with freestream velocity and hence, a new performance parameter is defined as T_C. The advantage of using T_C is that the parameter provides a comparison between the different propeller designs, and operating conditions for a given disk loading.

$$T_C = \frac{T}{\rho_\infty V_\infty^2 D^2} \tag{2.8}$$

The propeller performance are defined by the key performance indicators described in the equation 2.3 - 2.8, and by the radial loading distribution in the propeller blades. Depending upon the performance, propeller are distinguished into two broad categories - Fixed pitch propellers and fixed speed propellers. For a fixed pitch propeller, the propeller operates on a constant pitch with a controllable rotational speed,

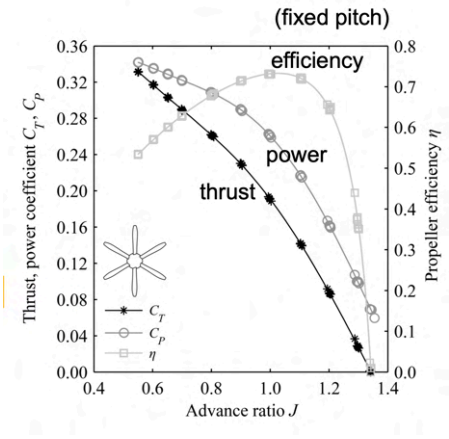

Figure 2.3: Performance Graph - Relation between advance ratio and key aerodynamic performance parameters[13]

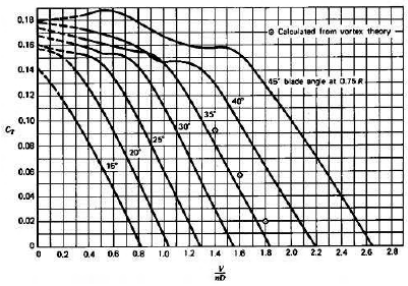

(a) Propeller performance curves with advance ratios

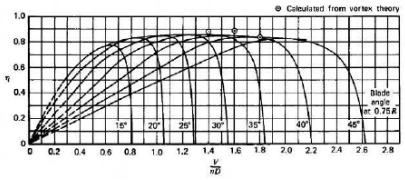

(b) Propeller Efficiency curves with advance ratios r

Figure 2.4: Typical Propeller performance and efficiency curves with advance ratios

while for the fixed speed propeller, rotational velocity remains constant, while pitch can be changed depending upon the flight. In the case of constant pitch propeller, the key performance parameters depends only upon the rotational speed of the propeller and flight velocity.

The relation between key performance parameters, and the advance ratio for the case of fixed pitch propellers are depicted in the figure 2.3. With increase in advance ratio, there is an increase in axial/tangential velocity ratio ($\frac{V_\infty}{V_{tgt}}$), which consequently, increases the inflow angle. Now, since pitch angle is constant, angle of attack experienced by the blade section decreases, which results in decrease in Thrust force by the propeller blade. When the advance ratio, becomes too small, the thrust and power starts to flatten out due to the non linearity in propeller induction with advance ratio, and eventually resulting in flow separation as seen in the left side of the figure 2.3. This mechanism can be seen analogous to the stall of an aircraft wing, where flow is separated due to high angle of attack.

In the case of fixed speed propellers, the rotational speed of a propeller is constant and the pitch can be controlled. The advantage of a fixed speed propeller is that the propeller can be optimized for the single operation during the flight. Moreover, pitch can be controlled in such a way that propeller is maintained at a maximum efficiency during the different phases of the flight. Therefore, in such propellers, the aerodynamic performance of the propeller is dependent on both advance ratios and the pitch angle, which can be changed during the flight. Therefore, the thrust and power coefficients of propeller are dependent on two variables, and a performance graph becomes a performance map, which is given in the figure 2.4. In this plot power coefficient is plotted as a function of thrust coefficient, advance ratio and pitch. Using the performance map, propeller efficiency can be optimized my matching correct pitch with the flight conditions.

A propeller can also be used to generate a negative net torque during the descent and landing phases of a flight mission by changing the pitch and rotational speed of the propeller until the angle

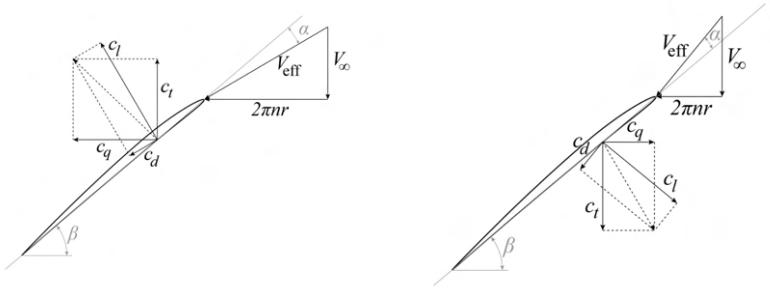

(a) Propulsive Regime

(b) Regenerative Regime

Figure 2.5: Velocity triangles of fixed-pitch propeller in propulsive and regenerative mode[12]

of attack at the blade sections is negative. The electric motor can function as a generator and can be used to harvest the energy as a result of the negative torque produced.[14] This state is known as the regenerative regime, where the propeller pitch is changed to produce negative thrust and torque, which can help slow the aircraft during landing and additionally generate the energy that can be harvested subsequently. Design optimizations by Pipistrel for small electric trainer aircraft trainer led to energy savings by 19 percent.[15] Figure 2.5 illustrates the fixed pitch propeller blade sections in the propulsive (positive thrust) and regenerative (negative thrust) modes.

2.3. BEM Model

In this section, the blade element momentum (BEM) theory to compute thrust and torque forces is presented. The blade element momentum theory is a fast method to compute aerodynamic and flow analysis, but it has its own limitations. However, it is required that the BEM solution shows at least a dependency or sensitivity to sweep.[8] The implementation of a basic BEM model is discussed here, which is also used as an input to the structural analysis to compute stress and deformations. It is important to note that the implementation of BEM is not the primary scope of the present work, and hence, it is only used as an input for the structural analysis. In order to have a correct aerodynamic loads, especially for the case of swept blades, it is urged to use updated BEM model for the swept propeller blades.

2.3.1. General Theory

The BEM theory is commonly used in the applications for wind turbines and propeller analysis. The blade element momentum theory combines two theories, the momentum theory and the blade element theory.

Actuator Disk Theory

Actuator disk theory is commonly known as the classical momentum theory. In this theory, a steam tube through an actuator disk, such as propeller is considered. It was introduced by Rankine in 1865.[16] Figure 2.6 depicts the contracting stream tube used in the research to explain this theory. The stream-tube is contracting so as to increase the axial velocity of the stream. The bernoulli's theory is used throughout the streamtube to compute flow properties. The thrust is generated by the actuator disk due to the momentum difference between far upstream and far downstream of the streamtube. This momentum difference created an instantaneous increase in the total pressure at the actuator disk. The main assumptions of the actuator disk are as follows:

- Freestream is assumed to be steady, inviscid and incompressible.
- Flow passing through the streamtube is separated from the rest of the flow by well defined stream-tube.
- Rotation of the flow is neglected
- There is a uniform velocity profile across the disk and stream-tube.

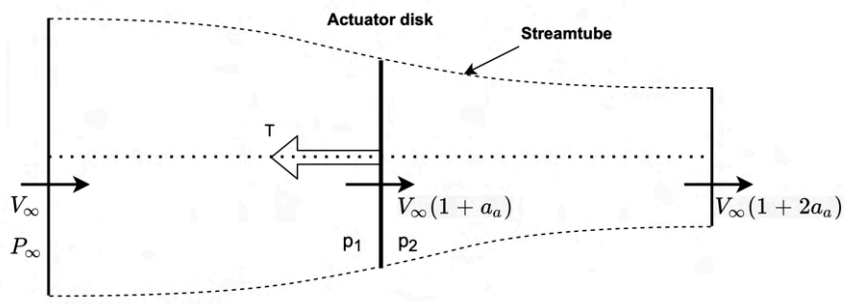

Figure 2.6: Representation of actuator disk theory, showing contracting streamtube and the actuator disk

Blade Element Theory
Blade element theory, combined along with Actuator disk model results in BEM model for the prediction of aeroforces in the propeller. In this theory, it is assumed that the streamtube in the figure 2.6, is divided into several streamtube control volumes, and as a consequence, the propeller blade is divided into several sections of width dr. In Blade element theory, relevant two dimensional force can be determined by using the shape of element and the angle of attack α. Figure 2.2b shows a 2D blade element at a certain angle of attack α and Thrust dT and Torque forces dQ are determined from the velocity v_∞.
By combining blade element theory and momentum theory, following assumptions has to be made

- Momentum increase in each of the annular streamtube is a result of thrust and torque forces generated by the blade elements.
- Radial interaction effect between blade elements and annular streamtubes is neglected.
- The assumption of uniform velocity and loading over the actuator disk is no longer valid. However, by subdividing the actuator disk into smaller annuli, the assumption can still remain valid, considering the individual annuli.

Therefore, in each of the individual annuli over the disk a constant loading is assumed. This assumption enables an assessment of the radial distribution of the thrust and torque forces over the propeller blade. Due to the two dimensional analysis of blade elements, the effects of vortices leaving the root and tip of the propeller blade which induces a velocity fields, are not considered in the Blade Element Momentum Theory. Therefore, Prandtl's loss correction factor needs to be applied while using the BEM-model to correct for the loss.

2.4. BEM model Implementation

In the current study, a classical and basic BEM model implementation has been used for prediction of aerodynamic forces based on the works of Geng et al. [17] and Liu and He [18]. The classical implementation of Blade element and Momentum Theory is provided in this section. It is important to note that the primary objective of current thesis is not to develop a model for BEM and hence, the basic BEM model is used for the present study. Hence, a classical and basic BEM model has been implemented here, without the estimation of losses and correction method for the sweep in blades.
The present BEM model does not include secondary effects, such as induced flow fields on the propeller due to the tip vortex and rotation in flow induced by angular acceleration due to propeller rotation. It also assumes a breakdown for extreme conditions for example, when the flow on the blade is stalled. For the simplicity of the model, XFoil convergence at low angle of attack is implemented for the evaluation of Lift and Drag coefficients, in order to predict Thrust and Torque forces, and the lift and drag coefficients at an angle of attack α is given by

$$\begin{aligned} C_l &= f(\alpha, Re, Ma) \\ C_d &= f(\alpha, Re, Ma) \end{aligned} \tag{2.9}$$

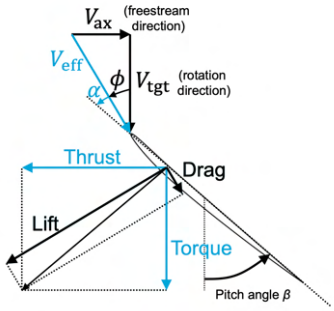

Figure 2.7: Blade section at a radius r

Blade Element Subdivision
Each of the propeller blade can be subdivided into a number of discrete sections. Each of the section is analyzed independently, and it is affected by only axial and angular velocity and the induced flow from the other section is neglected.
A section of a blade at radius r is shown in the figure 2.7.

The flow on the blade can considered to be consisting of the following:

- V_0 Axial flow velocity (Free stream velocity)
- V_2 Angular flow velocity (Tangential velocity)
- V_1 Effective Velocity

As the propeller blade is set at a pitch angle (β), the local velocity field will see an angle of attack, α, which in turn will result in Lift and Drag that can be calculated using 2D airfoil properties. The thrust and torque components are considered to be normal and parallel to the propeller disk, and can be computed with the help of lift and drag forces.

Equation 2.10 gives relations from the velocity triangle in a 2D blade section of a propeller blade.

$$\begin{aligned} V_1 &= \sqrt{V_0^2 + V_2^2} \\ \phi &= \tan^{-1}\left(\frac{V_0}{V_2}\right) \\ \alpha &= \beta - \phi \end{aligned} \tag{2.10}$$

Thrust and Torque per section can be related to the lift and drag forces, with the relations 2.11

$$\begin{aligned} \mathrm{d}L &= \frac{1}{2}\rho V_{\mathrm{eff}}^2 C_l c \\ \mathrm{d}D &= \frac{1}{2}\rho V_{\mathrm{eff}}^2 C_d c \\ dT &= dL\cos\phi - dD\sin\phi \\ dQ &= (dL\sin\phi + dD\cos\phi)r \end{aligned} \tag{2.11}$$

Total Thrust and Torque forces by the propeller of N blades can be given by equation 2.12

$$\begin{aligned} T &= \frac{1}{2}\rho V_1^2 c\,(C_L\cos(\phi) - C_D\sin(\phi))\,N\cdot dr \\ Q &= \frac{1}{2}\rho V_1^2 c\,(C_D\cos(\phi) + C_L\sin(\phi))\,N\cdot dr \end{aligned} \tag{2.12}$$

Inflow Factors

The major complexity in the application of this theory arises in calculating the velocity components of the streamtube near actuator disk. The axial component V_0 can be considered roughly equal to the freestream velocity (forward velocity of aircraft V_∞) but, is increased by a factor due to contracting streamtube. Tangential velocity V_2 can be roughly equal to blade's rotating velocity (Ωr), but is reduced due to swirling nature of propeller. In order to evaluate V_0 and V_2 correctly, axial momentum & angular momentum needs to be balanced to predict the induced flow effects on the blade element.
Assumed velocities can be given by equation 2.13, where a represents the axial inflow factor and b is the angular inflow or swirl factor.

$$\begin{aligned} V_0 &= V_\infty + aV_\infty \\ V_2 &= \Omega r - b\Omega r \end{aligned} \tag{2.13}$$

Angular and Axial Momentum Conservation

The principle of conservation of flow momentum can be applied in both axial and circumferential directions. For the axial direction, the change in momentum along the streamtube starting upstream of propeller disk, passing through the propeller section and exiting the stream tube, must be equal to the thrust generated by the element. Neglecting the unsteady effects due to the propeller's rotation, and streamtube area equivalent to area of propeller disk swept, thrust can be given as

ΔT = Change in Momentum flow rate through tube at disk
= Mass flow rate in tube × Change in velocity along tube

$$\Delta T = \rho \cdot 2\pi r \cdot dr \cdot V_0 \times (V_s - V_\infty) \tag{2.14}$$

Applying Bernoulli's equation and conservation of momentum, from freestream to face disk and to face disk to far downstream and balancing it with thrust, the exiting velocity from the streamtube can be determined, and is given by:

$$V_s = V_\infty(1 + 2a) \tag{2.15}$$

Substituting the exit velocity and inlet velocity into 2.14, Thrust can be given by

$$\begin{aligned} \Delta T &= 2\pi r\rho V_\infty(1 + a)\,(V_\infty(1 + 2a) - V_\infty) \cdot dr \\ &= 4\pi r\rho {V_\infty}^2(1 + a)a \cdot dr \end{aligned} \tag{2.16}$$

Similarly, angular momentum can also be conserved, with the help of torque generated by the blade element. ΔQ = Change in angular Momentum flow × r ; = Mass flow rate in tube × Change in circumferential velocity × r

$$\Delta Q = \rho.2\pi r.dr.V_0 \times \left(V_{\theta(\text{ slipstream })} - V_{\theta(\text{ freestream })}\right) \times r \tag{2.17}$$

Similar to the axial momentum, by conservation of angular momentum in the part from upstream to the disk and disk to the far downstream, angular velocity is computed, and is given by:

$V_{\theta(\text{ slipstream })} = 2b\Omega r$ and $V_{\theta(\text{ freestream })} = 0$

$$\begin{aligned} \Delta Q &= 2\pi r\rho V_\infty(1 + a)(2b\Omega r)r.dr \\ &= 4\pi r^3 V_\infty(1 + a)b\Omega.dr \end{aligned} \tag{2.18}$$

Hence, now there is a system of non-linear equations 2.12, 2.13,2.16 and 2.18, containing four primary unknowns T,Q,a and b. An iterative solution to this system of non linear equations, can be provided to evaluate the properties.

Iterative Solution

To start the solution, some value of the inflow factor a and swirl factor b is assumed. This is used in turn, to evaluate the flow angle of the blade and angle of attack of the airfoil from equation 2.13, and later it is used in equation 2.12 to determine the Thrust and Torque by the blade elements. These approximated values of Thrust and Torques are used again to find a improved estimates of the inflow factors with the equation 2.16 and 2.18.
The process is iterated until the values of a and b converges with a certain specified tolerance, to predict the correct torque and thrust forces.

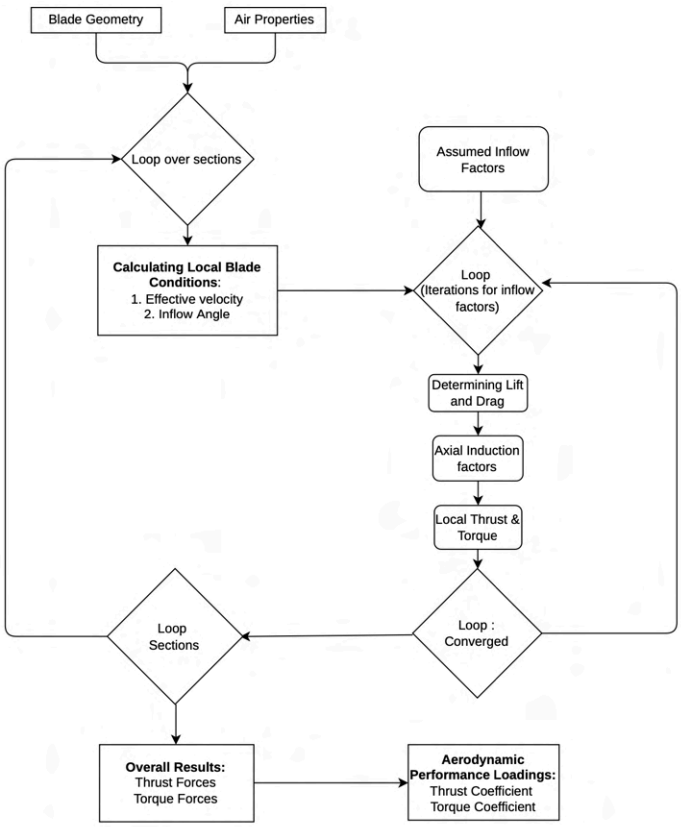

Figure 2.8: Flowchart for BEM model

Figure 2.8 gives a flowchart for the implementation of BEM model, which predicts the thrust and torque of the propeller blade. Overall torque and thrust can be found by summing up the results of all the radial blade elements. The performance indicators of the propeller blade can be evaluated according to the equations 2.4 - 2.7.

2.5. Sweep in the propeller blades

Mid chord alignment is the offset between the mid chord point and the pitching axis at each blade element as defined by Hanson [19]. Mid chord alignment is an important factor in the blade design as it can improve the aero-acoustics as well as the aerodynamic performance of the propeller engine. It is therefore, an important factor and needs to be defined in the propeller geometry. A fully dependent design variable is the blade sweep angle $\gamma(r)$. The calculation of this parameter is important for the structural model as well, as it has a great influence on the centrifugal moment of the propeller. The blade sweep angle is defined as the angle between the mid chord of two adjacent blade elements, as shown in equation 2.19.The relation between the mid-chord alignment and the blade sweep angle at a blade element is illustrated in figure 2.9. In the given figure, the blade section is swept backwards with respect to an adjacent blade section. It means that blade is swept backwards when it has a positive MCA and a positive blade sweep.

$$\gamma_i = \tan^{-1}\left(\frac{MCA_{i+1} - MCA_i}{r_{i+1} - r_i}\right) \tag{2.19}$$

Usually, in the case of aircraft wings, sweep is defined with the quarter chord sweep angle. In BEM Theory by Gur and Rosen [21] the quarter chord sweep angle is used to determine the effect of blade

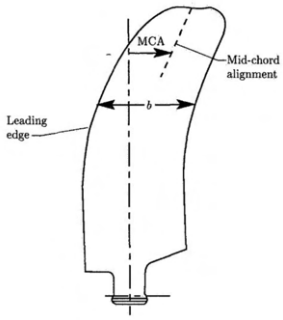

Figure 2.9: Definition of mid chord alignment[20]

sweep on aerodynamic performance. However, here in this project, mid chord is used to define the sweep as the leading edge and the trailing edge of the blade needs to be averaged. Burger [8] explains in detail the importance of using the mid chord sweep instead of a quarter chord.

2.6. Propeller Structural Module

Designing a propeller for both high aerodynamics and aeroacoustic performance can be a tedious process. The change in design can lead to lowering the noise emissions but also, the propulsor efficiency. Hence, an optimization study needs to be done for the design of a propeller with high aerodynamic and aeroacoustic performance. Such multidisciplinary studies were done earlier by.[7,17] However, after having a closer look at the optimized blade, it was observed that blade is not feasible structurally. It leads to high internal stresses, deformations and vibrations during the operation of propeller. Therefore, a low fidelity structural model needs to be built and used in the optimization code, to find the blade feasible to use in propeller.

2.6.1. Previous Structural Studies

In this section, previous studies related to structural modelling of propeller are discussed. As this model needs to be used for the multidisciplinary propeller optimization, there is a focus on integration of the aerodynamic and structural models, and evaluating the stresses at various sections of the blade.
The structural modeling of propellers dates back to the early 1900s, when the first flight was achieved using propeller blades. In the first works of Weick [11], a steady rectilinear flight is considered, such that the loads purely aerodynamic and centrifugal. The propeller blade is modeled as a cantilever beam, in which the stress at any cross section depends on the loads on the blade from the section to the tip of blade. The loading on the section were due to the aerodynamic and centrifugal forces and the bending moments were evaluated, to compute the stresses at each sections. It is interesting to note that, the stresses were generally over-predicted, as the propeller blades generally, got deflected and changed their geometrical shapes. Due to this, there were changes in the stress values which were predicted in the first works. Figure 2.10 depicts the affects of the deflection on the blade stresses computed using cantilever beam theory.

With the introduction of new turbojet and turboprop engines later in the twentieth century, the emphasis shifted away from aircraft propellers. However, in the case of marine transport, the marine propellers became more popular, there was a heavy focus on them. There is a strong connection between aircraft and marine propellers that dates back to the development of Blade element momentum theory for marine propellers by Rankine in 1865. As a result, marine propeller models were also researched and examined for structural modeling of blades. The structural model from Carlton [16] uses Cantilever beam method, with the radial distribution of thrust and torque forces, as shown in the figure 2.11 by equivalent loads at center of action.

The bending moment due to hydrodynamic loads around the radius (r_0) are evaluated using the thrust and torque forces, in which F_T and F_Q are integrated forms of thrust and torque forces with a and b as there respective center of actions as shown in the figure 2.11. Through the centroid of the

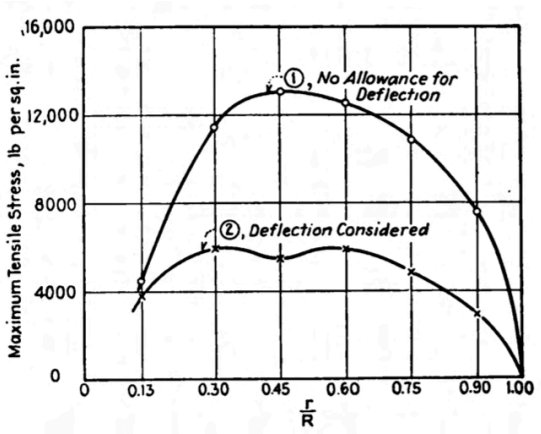

Figure 2.10: Maximum Tensile Stresses in the propeller blade, adapted from Weick [11]

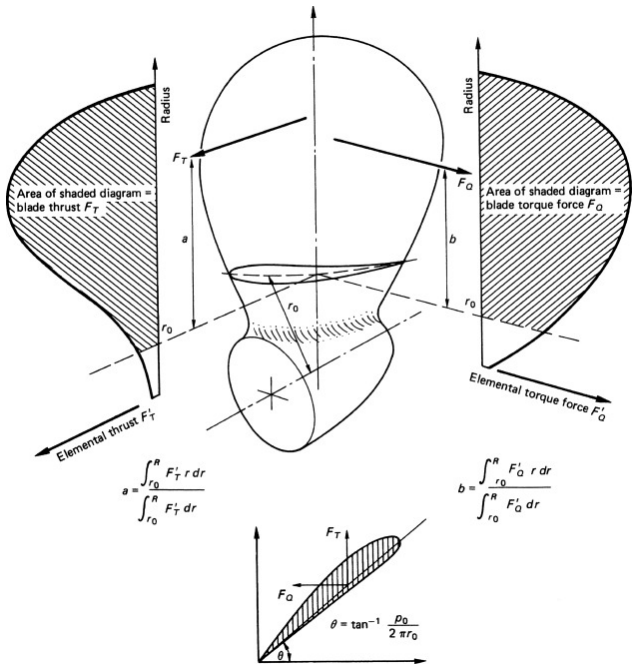

Figure 2.11: Cantilever Beam Model, adapted from Carlton [16]

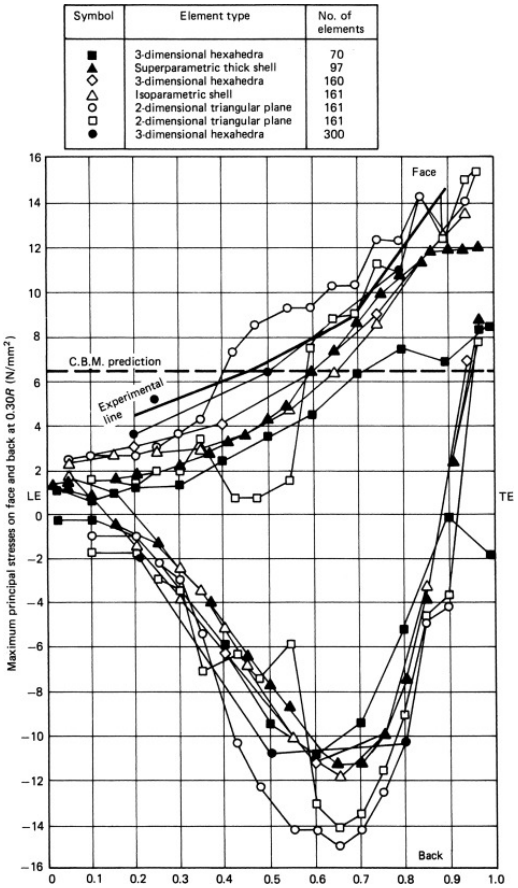

Figure 2.12: Stress Distribution with chordwise coordinate at 30% of radial section, adapted from Carlton [16]

section, centrifugal loads are considered and centrifugal moments are evaluated. Hence, total moment is evaluated due to combination of both hydrodynamic and centrifugal loads, and in turn, stresses in the sections can be computed using the above moments. It is important to note that the shear and torsional stresses are neglected in both of the above analysis.
With the advancements in the computer technology, intensive research efforts led to the development of finite element theory using the shell theory[22,23] and later using plate elements initially and then more recently isoparametric and superparametric solid elements. The principal advantage of these methods over cantilever beam methods is that they evaluate the stresses and strains over a much greater region of the blade than can the simpler methods, assuming that it is possible to define the aerodynamic blade loadings accurately.[24,25] Furthermore, it can produce a stress criterion, to develop blade stress distribution which can be correlated with the model and full scale measurement.

While using the finite element analysis, the choice of element is critical if valid results are to be obtained. It is insufficient to arbitrarily use the formulations as with the various finite elements results can vary marginally. A study on a marine propeller was performed in ITTC,[27] in which the results from finite element computations from six organizations, using seven different finite element formulations of the problem, were compared to experimental results at model scale. The propeller chosen for the study was a 254 mm diameter, $72°$ biased skew design propeller C of taken from Carlton [26] as shown in the figure 2.13 The model was subjected experimentally to point loading at $0.7R$ and 50% of chordal location, and was instrumented with 4 sets of strain gauge at the root section of the blade on the pressure side at $0.3R$. Figure 2.12 demonstrates the results from the finite element formulations and a comparison with the experimental study. A cantilever beam calculation for the same loading is also shown, which corresponds to the highest stress obtained from the cantilever beam model at the same

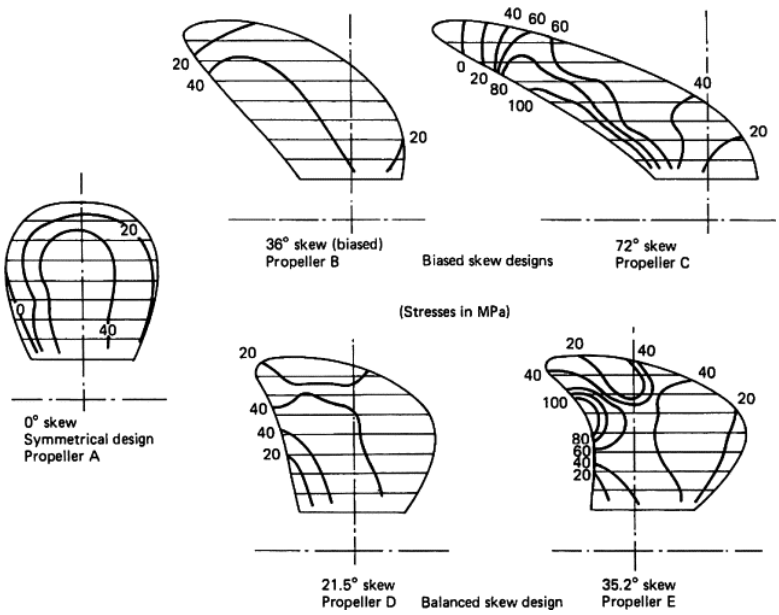

Figure 2.13: Different types of marine propeller used for FEM studies[26]

radial section of the blade ($0.3R$). The figure 2.12 also demonstrates that the cantilever beam model, underpredicts the magnitude of the loadings especially, in the root section of highly skewed blades.

The low-fidelity structural models have been heavily used in previous research for propeller design optimizations. Sodja et al. [28] used a mathematical model based on extended - Blade Element momentum model for propeller aerodynamics and Euler-Bernoulli beam theory coupled with Saint-Venant theory to account for bending and torsion, respectively. This results in a quick and robust propeller analysis model capable of dealing with high aspect ratio propeller blade design for flexible blades. Although, the structural model presented in nonlinear for the treatment of geometry of the blade axis, the constitutive relations between stress and strains remains to be linear. This model thus, provides an optimized geometry for the blade axis of propeller blades, which can have a much higher curvature as compared to the linear geometry models. Maximum equivalent von-mises stress was considered as the parameter of optimization in the propeller design algorithm, along with the blade deformations.

MacNeill [29] presented a propeller optimization study for Unmanned Aerial Vehicles (UAVs). The blade element momentum theory model was used to predict propeller aerodynamics and evaluate aerodynamic loadings, and a structural model was implemented as an integral part of the propeller blade design optimization to ensure that each propeller blade can withstand the stresses from these loadings. A three-dimensional Euler-Bernoulli beam theory and a finite element model were used to create an accurate and efficient structural model. The propeller blade axis is discretized into a series of spanwise elements by the finite element beam model, and the loads from the aerodynamic model are imported on the aerodynamic centers of the propeller blade sections. At each blade section, a local Cartesian coordinate system was established, areas and moments of inertia were calculated about the principal axis, and a finite element model was used to determine final stresses and displacements in the blades. To evaluate the torsional stresses, an equivalent rectangle method was used, which considers an equivalent rectangle to that of an airfoil with the same cross section area and chord length but new thickness depending on the airfoil's area of cross section. Torsional stress is calculated directly using the rectangle and torsional moments relations. Finally, the equivalent von-mises stress is calculated using the finite element model's bending stresses and the rectangular approximations' torsional stresses, and the maximum von-mises stress is calculated, and the maximum von-mises stress is compared to allowable tensile stress and considered as a parameter for design optimization.

Based on these studies and low-fidelity models, a similar cantilever beam model for a swept blade can be proposed, with the maximum von-mises stress used as a design optimization parameter. To evaluate stress distribution over the blade, Euler-Bernoulli beam theory and Saint-Venant theory for

torsion can be combined. For accurate stress distributions, a finite element model can be built to discretize the partial differential equations from Saint-Venant theory and consequently, evaluating shear stress. The structural model is proposed in the next chapter considers Sodja et al. [28] as the reference, and a similar model for swept blades is proposed.

3

Structural Analysis of Propeller Blade

In this section, the structural modelling part will be introduced and explained for a propeller blade. Assumptions of the structural model are described in section 3.1. In the section 3.2, non-dimensionalization of the airfoil is briefly explained to evaluate the structural properties, followed by a framework to evaluate torsional shear stresses and Saint-Venant theory which is presented in the section 3.3. Finally the cantilever beam model is presented in the section 3.4, with is used for the low-fidelity structural model.

Calculation of the stress in a propeller blade, due to the complex design of the blade is difficult problem. A general blade can have a varying twist, airfoil profile, sweep in blade and distributed chord length. Moreover, a distributed aerodynamic loads and centrifugal loads appear on the blade as it rotates with high speeds.

In a general propeller blade, the three main types of loadings are :

1. Loads due to aerodynamic forces (Thrust and Torque Forces).
2. Loads due to centrifugal forces.
3. Loads due to gyroscopic and inertia forces due to unsteady motion.

In the analysis for a steady flight, the loadings are limited to only aerodynamic and centrifugal loads. Loads due to gyroscopic and other inertia forces are small compared with the air and centrifugal loads, and a propeller which is strong enough to endure the latter two types of loads for an indefinite period of time is also strong enough to stand the slightly higher total loading during the relatively short periods in which the gyroscopic and other inertia forces act.[11]

In the low fidelity structural modelling, Euler Bernoulli beam theory is used to predict the stress and deformations along the blade. This needs to be further validated with a finite element analysis of the blade which was done using ANSYS Static Structural Module to compare and contrast the results of the low fidelity model.

3.1. Assumptions of the structural model

- For the structural model, a solid propeller blade composed of isotropic and homogeneous material with constant density in all directions is assumed.
- The structural analysis neglects centrifugal and aerodynamic twisting forces, implying that the propeller is designed for steady rectilinear flight. The current analysis does not take gyroscopic inertial loads or unsteady aerodynamic loads into account.
- The resultant aerodynamic loading (thrust and torque) is computed from the low fidelity BEM model, and these forces are assumed to be perpendicular to the propeller chord. Aerodynamic and inertial loads are both considered static, resulting in constant stress over time.
- The Euler–Bernoulli beam theory is employed to account for the bending stress, and the Saint-Venant principle is utilized to account for the torsional loads. This theory has proven to work for aspect ratios of 10 or higher and has been previously used in blades design.[28,29]

- Airfoils are stacked to form a propeller blade and twist along the Pitch Change Axis (PCA), which is fed into the model as input. Airfoils are stacked with the centroid (Center of mass) in a straight line for the current model of straight blades.
- It is assumed that the propeller blade does not experience significant deflections and that the geometry of the blades does not alter significantly as the blade experience high stress.
- The investigation of an isolated propeller blade is assumed implying that the interactions between multiple propeller blades are ignored, resulting in aerodynamic loads due to a single propeller blade only.

Propeller blade considered in the current project can be thought of as a slender, pretwisted cantilever beams of a variable cross section depending upon the airfoil profile and properties including twist, chord and sweep angle of the blade. This is also assumed to be built out of a homogeneous and isotropic elastic material. It was also assumed that the blade is in the undeformed state and the deformations will not affect the stress significantly. All the stresses in the blade are expected within the elastic limit of the material in all things.

3.2. Cross-sectional Mechanical Properties

Blade cross section is input given by the user specifying the NACA profile, or directly importing the airfoil coordinates. The cross sections are also scaled uniformly in the size. In order to simplify and compute the structural properties of the airfoil, a unit cross section of airfoil was introduced, and the airfoil chord length was used as a normalization parameter. Non-Dimensional coordinates were introduced as $\bar{\eta} = \frac{y}{c}$ and $\bar{\xi} = \frac{x}{c}$, which allows to compute the important cross sectional properties, namely, domain area, principal moment of inertia, and torsional moment of inertia in non dimensional form.

The airfoil profile is taken as an input from `XFoil` software. Furthermore using the interpolation function in MATLAB ®, airfoil is broken down into 101 discrete points on X axis ($\bar{\eta}$ axis) and 101 discrete points corresponding to the pressure and suction surface each. Hence, the each airfoil profile is taken as 201-sided polygon from the airfoil. The cross sectional properties are further calculated in non dimensionalized coordinates as:

$$\bar{A} = \int_{\bar{A}} \mathrm{d}\bar{A}; \quad A = c^2 \bar{A} \tag{3.1}$$

$$\bar{I}_\eta = \int_{\bar{A}} \bar{\zeta}^2 \, \mathrm{d}\bar{A}; \quad I_\eta = c^4 \bar{I}_\eta \tag{3.2}$$

$$\bar{I}_\zeta = \int_{\bar{A}} \bar{\eta}^2 \, \mathrm{d}\bar{A}; \quad I_\zeta = c^4 \bar{I}_\zeta \tag{3.3}$$

$$\bar{I}_t = -4 \int_{\bar{A}} \bar{u} \, \mathrm{d}\bar{A}; \quad I_t = c^4 \bar{I}_t \tag{3.4}$$

$\bar{u}$ is the Prandtl's stress function, which is also calculated in the non dimensional form, which will be explained in the next subsection.

3.3. Torsional Stress evaluation

Due to the presence of a several moments on each airfoil cross section, there is a also a moment which provides a torsion to the airfoil. It is the component of the moment in the direction of blade axis, which tries to "twist" the blade section. In the present work, two different approaches were presented to determine the torsional stress in simply connected pre-twisted cantilever beam, which is subjected to constant torque at particular section.

3.3.1. Rectangular Approximation of Airfoil

The calculation of shear stress present in a non symmetric propeller blade can be a tedious task, due to complexities in the airfoil profile. In the first approach, for the simplicity in calculations, the blade cross section is transformed into a rectangle of the equivalent geometric properties as shown in the figure 3.1.

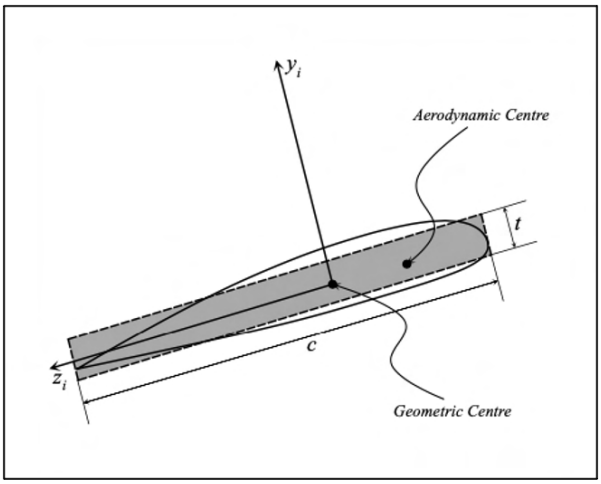

Figure 3.1: Rectangle of equivalent geometric properties[29]

The chord length of the cross section is kept constant while the thickness of the rectangular section in found by keeping area as of airfoil cross section. The shear stress present in the rectangular cross section due to a torque is given by:

$$\tau = \frac{VQ_{shear}}{It} \tag{3.5}$$

Here, τ is the shear stress in the cross-section at a point located a certain distance y' from the neutral axis. The stress is assumed to be constant across the width of cross section. Shear force is represented by V, I represents the moment of inertia of the cross section about neutral axis and t denotes the approximated thickness of cross-section. Q_{shear} denotes the area-centroid shear term, and is given by $Q_{shear} = \bar{y}'A'$ and A' is the area of cross-section above or below where t is measured. After solving the maximum shear stress due to torsion in a rectangular cross section is given by Roark et al. [30]

$$\tau_{\max} = \frac{3M_T}{8\left(\frac{c}{2}\right)\left(\frac{t}{2}\right)^2}\left[1 + 0.6095\frac{t}{c} + 0.8865\left(\frac{t}{c}\right)^2 - 1.8023\left(\frac{t}{c}\right)^3 + 0.9100\left(\frac{t}{c}\right)^4\right] \tag{3.6}$$

Here, T is the torsional moment applied to a cross-section. The maximum shear stress occurs at the midpoint of the longer sides of the rectangle.

3.3.2. Numerical Solution to Airfoil : Saint-Venant theory

The resistance of materials gives the theoretical relationships only for torsion of a symmetric sections like rectangles, circles etc. But, for an aircraft, most of the structures are non symmetric including the wing, fuselage, drift, spars, blades, blade of a helicopter, and others involving the field of mechanical engineering.[31]

For a general propeller blade, accurate approach to solve the torsional stress in the non-symmetric airfoil cross section of the beam is to use the finite element method and discretize the airfoil to solve for the stress function. In the present work a numerical calculation program was developed using in-build MATLAB ®functions to discretize given NACA profiles. The boundary conditions is specified to be of Dirichlet condition. Finite element analysis is complicated due to the problems in 2 dimensions are described in the form of partial differential equations. The contour Γ of the domain Ω in two dimensions is in general a curve.[32] The finite elements can have a simple geometric shapes that can be used as an approximation to the data field in two dimensions, in general. Therefore, the airfoil geometry is meshed into smaller geometric shapes and the approximations of the solution of partial differential equations are seeked along with the approximation of the field given by a meshed finite element.

The opportunity to represent the geometry of the collective area by finite element method makes it valid and a practical tool for solving boundary value problems.[33] In the case of torsion of non symmetric cross

Maximum Element size	0.01
Minimum Element size	0.005
Mesh Gradation	1.5
Geometric Order	Quadratic

Table 3.1: Mesh Properties of the case example

section, the differential equation is a second order, linear and elliptic type with the boundary conditions of the first order of Dirichlet in arbitrary planar domain. The partial differential equations are given by:

$$\frac{\partial^2 \Phi}{\partial x^2} + \frac{\partial^2 \Phi}{\partial y^2} = -2G\theta; \quad \Phi = 0 \quad \text{on} \quad \Gamma \tag{3.7}$$

$$\tau_{xz} = \frac{\partial \Phi}{\partial x}, \tau_{yz} = -\frac{\partial \Phi}{\partial y} \tag{3.8}$$

$$M_t = 2 \int \Phi(x, y) dx dy \tag{3.9}$$

In order to find out the torsional stress, four unknowns ϕ, τ_{xy},τ_{xz},Θ needs to be calculated using the above equations. Subsequently, Prandtl introduced the concept of solving a problem of torsion with the single unknown, called as Prandtl's stress function $\phi(x, y)$. This function is differentiable and associated to the torsional stresses directly with the equation 3.8. It is assumed that the Prandtl's stress function is related to displacement by the relation 3.10.

$$\phi(x, y) = 2G\theta u(x, y) \tag{3.10}$$

After simplifying the equation 3.7 and 3.10, we have the following form of a partial differential equation which is also known as Poisson's equation 3.11.

$$\frac{\partial^2 u}{\partial x^2} + \frac{\partial^2 u}{\partial y^2} = -1; \quad u = 0 \quad \text{on} \quad \Gamma \tag{3.11}$$

Also,

$$\frac{\tau_{xz}}{G\theta} = 2\frac{\partial u}{\partial x}, \frac{\tau_{yz}}{G\theta} = -2\frac{\partial u}{\partial y} \tag{3.12}$$

$$\theta = \frac{M_t}{GI_t}$$
$$I_t = 4 \int u(x, y) dx dy \tag{3.13}$$

Where, I_t is the torsional moment of inertia of the cross section (Polar Moment of Inertia), M_t is the torsional moment at the cross section, G denoting the Shear Modulus of rigidity of the material of blade. The above partial differential equation is solved in a Partial Differential Equation toolbox in MATLAB ®. It is done so by first importing the airfoil profile from XFoil. The PDE modeler of the toolbox plots the airfoil profile naming the edges and the plane in the airfoil. A particular NACA airfoil is thus imported in the PDE modeler using a `decsg` function and from the PDE modeler, it is exported to the PDE model program with the help of `geometryFromEdges` function in MATLAB ®figure 3.2a. Boundary conditions are given to the PDE solver, using the `applyBoundaryCondition` function in MATLAB®, and the coefficients are specified according to the differential equations and are given in the table 3.3. Mesh elements are generated in the `generateMesh` function and the maximum size of the element is specified using the 'hmax' variable. Other parameters for the mesh is included in the table 3.1. Finally, the numerical solution is obtained by the `solvepde` function in MATLAB®and is solved to find out torsional stress τ_{xz} and τ_{yz}. Important parameters for the solver are included in the table 3.2
A case example of a NACA2412 airfoil is given in the following figure, where the solution for Prandtl function u is plotted in the figure 3.2c and 3.3c.

With the help of the Prandtl function solved numerically using the inbuilt MATLAB ®functions, torsional moment of inertia of any airfoil can be evaluated, by integrating the displacement function $u(x, y)$ over the surface of the airfoil as in the equation 3.13.

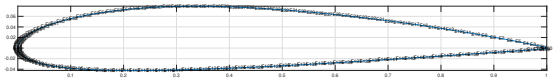

(a) Geometry in the PDE modeler with planes and edges

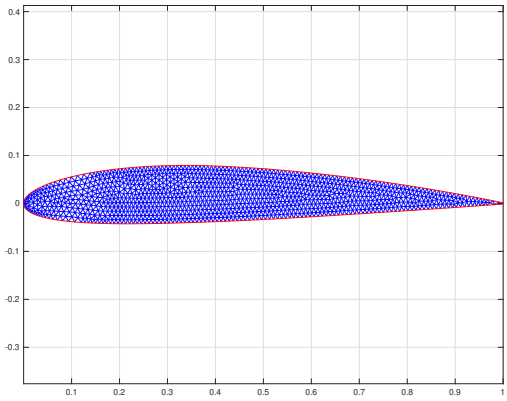

(b) Meshing using the in-built MATLAB ®function

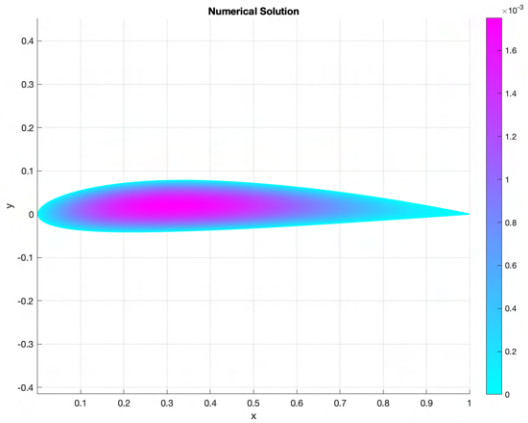

(c) Prandtl function solution to PDE

Figure 3.2: Case Example: NACA 2412

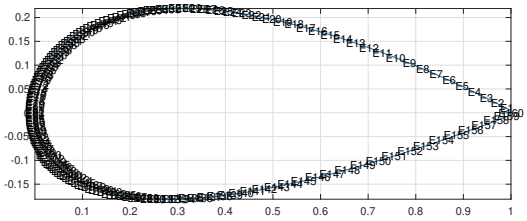

(a) Geometry in the PDE modeler with planes and edges

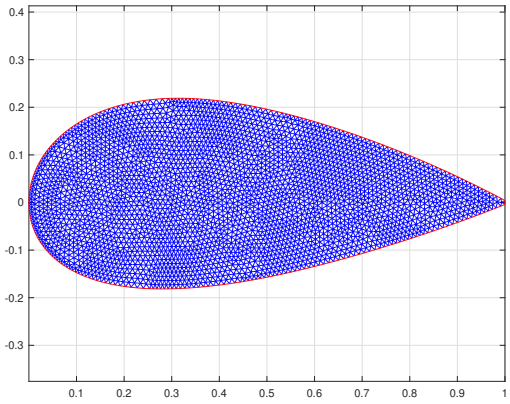

(b) Meshing using the in-built MATLAB ®function

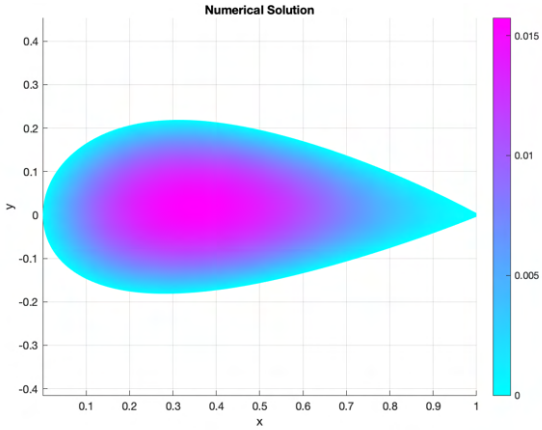

(c) Prandtl function solution to PDE

Figure 3.3: Case Example: NACA 2440

Absolute Tolerance	1e-6
Relative Tolerance	1e-3
Residual Tolerance	1e-4
Maximum Iterations	25
Minimum Step	1.5259e-05
Residual Norm	∞
Max Shift	100

Table 3.2: Solver Properties for the case example

m	0
d	0
c	1
a	0
f	1

Table 3.3: Coefficients for the Poisson's Equation

3.4. Cantilever Beam Model

Most important task in the structural modeling is computation of the moments and internal stresses from the aerodynamic and centrifugal loadings of the blade.

3.4.1. Aerodynamic Moments

The aerodynamic forces, namely Thrust(T) and Torque forces(Q) are obtained from the Blade Element Momentum code from the last section and were imported to the structural module. Elemental Thrust ($\frac{dT}{dr}$) and Torque ($\frac{dQ}{dr}$) are computed for each each cross section and is imported in the structural part of the code. These loadings were assumed to be acting on the center of pressure of airfoil section. In order to obtain the stresses, it is important to find the center of pressure of each airfoil section.
Center of pressure is defined as a point on the airfoil section where the resultant moment due to aerodynamic forces is zero, hence, center of pressure is not necessarily located at the Quarter chord of the airfoil section. Figure 3.4 explains the difference more clearly between quarter chord and the center of pressure of the airfoil.

Center of pressure can be computed using the definition and following relations for a given airfoil.

$$\begin{aligned} M'_{\mathrm{LE}} &= -\frac{c}{4}N' + M'_{c/4} \\ &= -x_{\mathrm{ac}}N' \end{aligned} \tag{3.14}$$

$$\begin{aligned} C_L &= \frac{L}{1/2\rho_\infty V_\infty^2 S} \\ C_D &= \frac{D}{1/2\rho_\infty V_\infty^2 S} \\ C_M &= \frac{M}{1/2\rho_\infty V_\infty^2 Sc} \end{aligned} \tag{3.15}$$

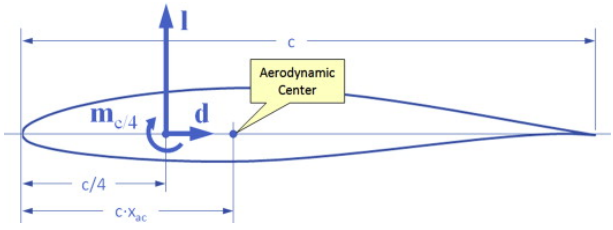

Figure 3.4: Location of Center of Pressure[34]

Here, N' is the vertical forces acting on the airfoil and $M'_{c/4}$ is the Moment at the quarter chord of the airfoil section. It is to be noted that for a small angle of attack α, N' can be approximated by:

$$N' = Lcos(\alpha) + Dsin(\alpha) \tag{3.16}$$

Simplifying all the above equations, location of Center of Pressure (x_{cp}) can be evaluated by the following:

$$x_{cp} = c\left[\frac{1}{4} - \frac{C_{m,c/4}}{C_l\cos(\alpha) + C_d\sin(\alpha)}\right] \tag{3.17}$$

Where, α is the angle of attack of airfoil, C_l and C_d representing the lift and drag coefficients at particular cross section and $C_{m,c/4}$ denoting the moment coefficient at quarter chord. It is to be noted that the x_{cp} denotes the distance from the leading edge of the airfoil along the chord, hence, in the code, center of pressure was computed by dividing chord into the ratio of $\frac{x_{cp}}{c}$ and $1 - \frac{x_{cp}}{c}$.

Moment due to aerodynamic forces at a particular section r_0 can be computed using the following equation.

$$\overrightarrow{M_A} = \int_{r_o}^{R} \left(\overrightarrow{r_{cp}} - \overrightarrow{r_{0,cen}}\right) \times \left(\overrightarrow{F_T} + \overrightarrow{F_Q}\right) \tag{3.18}$$

Here, $\overrightarrow{r_{cp}}$ is the radial vector from the center of the propeller blade to the center of pressure of cross section at radius r, $\overrightarrow{r_{cen}}$ denotes the radial vector from the center of propeller blade to the geometric center of the cross section at which aerodynamic moments needs to be evaluated. The total amount of aerodynamic moment acting at the cross section at r_0 is sum of all the moments acting on the blade from cross-section radius r_0 to tip radii R, hence is given by equation 3.18. It is further illustrated in detail in figure 3.5, where the aerodynamic center is represented by a triangle and the centroid by a star. The first airfoil section is used as a reference in this image, and the $\overrightarrow{r_{0,cen}}$ is calculated as a vector from the origin to the centroid of the reference section. Later, the vectors $\overrightarrow{r_{cen}}$ and $\overrightarrow{r_{cp}}$ emanating from the origin to the centroid and aerodynamic centers are assessed.

3.4.2. Centrifugal Moment

The centrifugal forces (F_c) is a major source of the moments especially in the case of swept propeller blades. Due to a high rotational speeds, the centrifugal forces can be extremely high which can cause catastrophic results, if not taken account of. In order to compute the centrifugal forces at a certain cross section r_0, firstly, it is necessary to evaluate contribution of centrifugal force at each of blade section. Centrifugal force at a certain section at radial distance r is given by:

$$dF_c = \rho A\omega^2 r dr \tag{3.19}$$

Where, ρ denoting the density of the blade material, A representing the area of cross section of the blade, ω denoting the rotational speed and r radial distance of the section from the center of propeller. The centrifugal force is assumed to be acting on the centroid of the airfoil (geometric center) as it is taken as a force acting on a point mass accumulated at the center. Moreover, as there is a direct axial stress in the beam due to the centrifugal loads, the total centrifugal force needs to computed at each section and is evaluated by integrating the above equation.

$$F_c = \int_{r_0}^{R} \rho A\omega^2 r dr \tag{3.20}$$

Furthermore, in order to compute the centrifugal moment (M_c) at a particular cross section r_0, all the centrifugal forces needs to be integrated from a radius r_0 to tip radii R. Moreover, centrifugal moment needs to be defined about the centroid of the airfoil section and later, added to the aerodynamic moment to evaluate the total moment. Hence, the centrifugal moment is given by the equation 3.21.

$$\begin{aligned} \vec{M}_c &= \int_{r_0}^{R} (\vec{r} - \vec{r}_0) \times \overrightarrow{dF_C} \\ \vec{M}_C &= \int_{r_0}^{R} \left(\overrightarrow{r_{cen}} - \overrightarrow{r_{0,cen}}\right) \times \left(\rho A\omega^2 r dr \overrightarrow{e_r}\right) \end{aligned} \tag{3.21}$$

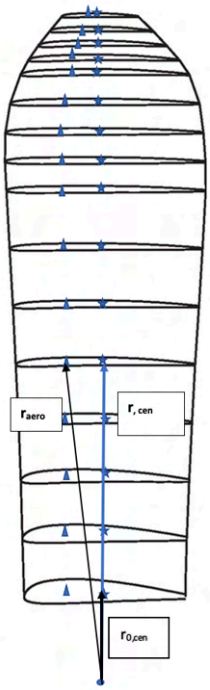

Figure 3.5: Illustration of the radial vectors originating from aerodynamic and centrifugal forces

Where, $\overrightarrow{r_{cen}}$ denotes the vector from the center of propeller blade to a centroid of radial section of the blade and $\overrightarrow{r_{0,cen}}$ denoting the vector to the centroid of the radial section where stress needs to be computed. It is explained more clearly with the help of figure 3.5.

3.4.3. Estimation of Stress

Total moment is the sum of centrifugal moment and aerodynamic moment, and is added vectorially as the moments have three different components along the X, Y, Z directions. The total moment due to all forces are given by:

$$\begin{aligned} \vec{M}_A &= \vec{M}_T + \vec{M}_Q \\ \vec{M} &= \vec{M}_C + \vec{M}_A \end{aligned} \tag{3.22}$$

Where, $\vec{M}$ represents the total moment acting at a section of the propeller blade. Hereafter, it is important to note that each section of the blade is stacked along the pitch change axis with a certain pitch angle. Hence, each section of the blade has its own neutral axis which is assumed to be parallel to the chord of airfoil, and is passing through the center of airfoil section. To evaluate the stress and deformations on the blade, the moment M is decomposed into the Local Coordinate System where the three components are along the blade axis ζ and two principal axis across cross section namely, ξ and η. Figure 3.6 gives an example for a Local Coordinate System at particular radial section r with ξ axis being parallel to the chord and η axis perpendicular to the chord in the plane of cross section. It is important to note that the origin in the Local coordinate System is at the centroid of the airfoil section, which is also taken as a reference point to evaluate the moments due to loadings.

Unit vectors along the local axis are given by equation 3.23:

$$\begin{aligned} \overrightarrow{e_\xi} &= [0, \cos(\beta), \sin(\beta)] \\ \overrightarrow{e_\eta} &= [0, \cos(\beta + \pi/2), \sin(\beta + pi/2)] \\ \overrightarrow{e_\zeta} &= \overrightarrow{e_\xi} \times \overrightarrow{e_\eta} = [1, 0, 0] \end{aligned} \tag{3.23}$$

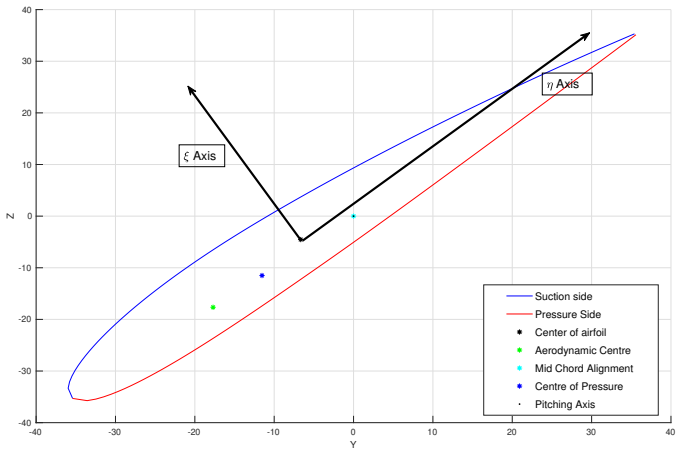

Figure 3.6: Local Coordinate System at radial section r

Where, β denotes the pitch angle of the airfoil section at certain radius. Consequently, the moments can be decomposed into three components along the blade axis, and two principal axes of the cross section:

$$M_\xi = \vec{M} \cdot \vec{e}_\xi; \quad M_\eta = \vec{M} \cdot \vec{e}_\eta; \quad M_\zeta = \vec{M} \cdot \vec{e}_\zeta \tag{3.24}$$

Deformations and the stresses in the blades are composed of two mutually dependent processes, namely bending and torsion. Bending stresses are treated according to the Euler-Bernoulli theory, taken into account large deflections. While the torsional stresses are accounted by applying the Saint-Venant theory of Torsion, neglecting warping effects. All the cross sections along the blade are solid, and as a result, warping of the cross sections along the blade is neglected in the calculation of stress.[28]

Using the above moments in LCS, the axial and shear stresses can be computed. In a beam subjected to a moment M in direction perpendicular to the cross section is

$$\sigma = \frac{My'}{I}$$

where, y' is the distance of the point where stress is evaluated from the centroid of the cross section, and I denoting the moment of inertia of the beam in direction of loading. Sum of axial stress is due to two bending moments (M_ξ and M_η) and also, direct centrifugal force (F_c) causing an axial stress. Axial stress thus, can be given by the equation 3.25

$$\sigma = \frac{F_C}{A} + \frac{M_\xi}{I_\xi}\eta - \frac{M_\eta}{I_\eta}\xi \tag{3.25}$$

Surprisingly, it is important to note that the axial stress due to M_ξ and stress due to M_η are of opposite signs. It can be explained with the help of figure 3.7. There are two bending moments acting along η axis and ξ axis on the section. To explain the signs, it is necessary to have a look at the first quadrant ($\eta > 0$ and $\xi > 0$). In this section, a positive moment in η axis (M_η) produces a compressible stress in the first quadrant. Similarly, a positive moment in ξ axis (M_ξ) produces a tensile stress in the first quadrant. Hence, for the first quadrant as, the tensile stress is taken to be positive, the stress corresponding to M_ξ has a positive sign, while stress corresponding to M_η has a negative sign.

A torsional moment along the blade axis (M_ζ) give rise to the shear stresses, which is also important to resolve. Amount of shear stresses is although lower in general, as the torsional moment occurs due to the aerodynamic forces only. However, shear stress can still increase the von-Mises stress along the blade and is necessary to resolve. The shear stress due to a torsional moment is give by equation 3.26.

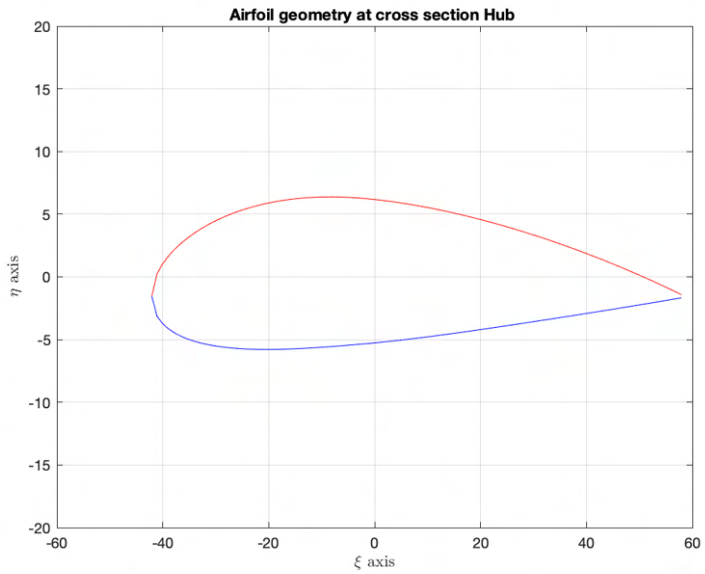

Figure 3.7: Hub section ($r = 0.2R$) in Local Coordinate System (LCS)

$$\tau = \frac{2M_\zeta}{I_t}|\nabla u| \tag{3.26}$$

From equation 3.12 and 3.26, the shear stress components can be given as

$$\begin{aligned} \tau_{xz} &= \frac{2M_\zeta}{I_t}\frac{\partial u}{\partial x} \\ \tau_{yz} &= -\frac{2M_\zeta}{I_t}\frac{\partial u}{\partial y} \end{aligned} \tag{3.27}$$

The terms $\frac{\partial u}{\partial x}$ and $\frac{\partial u}{\partial y}$ were computed in the previous subsection, by discretizing poisson's equation on the given airfoil section. As there are high number of mesh elements across the airfoil, it is not possible to find the terms $\frac{\partial u}{\partial x}$ and $\frac{\partial u}{\partial y}$ along the boundary of the airfoil, it is easier to evaluate maximum ∇u in each section, and replace in the 3.27, to compute the maximum shear stress along the section. It is important to note that, all the moment of inertia (I) and area terms (A) are the ones from airfoil of a chord length c, instead of the normalized coordinate terms.
With the help of *von - Mises equivalent stress* (σ_{eq}), which can be used as a parameter in the optimization is obtained by the relation 3.28.

$$\sigma_{eq} = \sqrt{\sigma^2 + 3(\tau_{xz}^2 + \tau_{yz}^2)} \tag{3.28}$$

It is important to note that the presented structural model has a non-linear geometry along the blade axis, however, the constitutive relations between stress and strains remains linear. The nonlinear geometric model was chosen as it gives an advantage to work for an optimized blade axis. As the optimized blade axis is not known, it can have a high sweep angles and curvature, hence, Blade axis can assume any arbitrary shape given with sweep angles and can be later, utilized in the optimization.

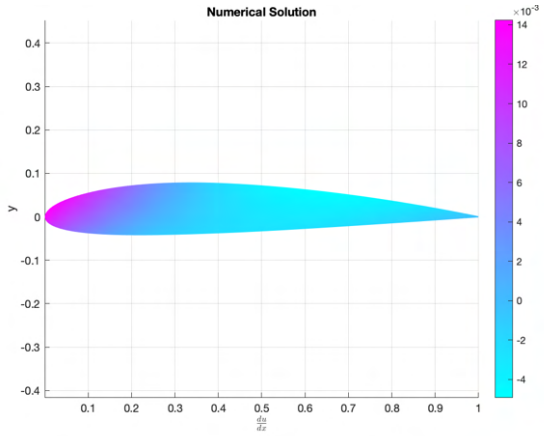

(a) Solution of $\frac{\partial u}{\partial x}$ on the airfoil

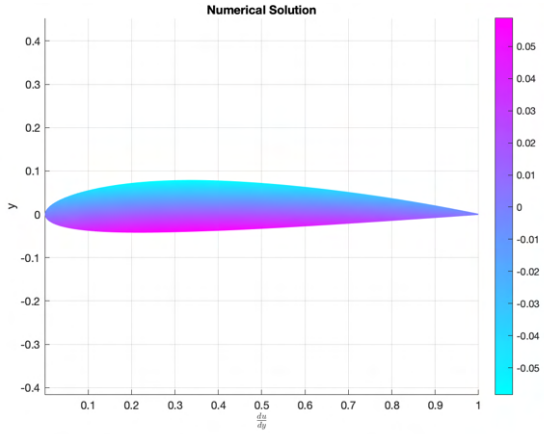

(b) Solution of $\frac{\partial u}{\partial y}$ on the airfoil

Figure 3.8: Solution of ∇u on the airfoil section

4

Model Verification and Validations

A verification and validation routine is carried out in order to make the model reliable and to instill some confidence in the results. Firstly, in the section 4.1, the new geometry of the given propeller is presented. Secondly, in section 4.2, CFD results from the propeller blade are discussed and the simulation setup for structural simulation is presented. Finally in the section 4.3, the low fidelity structural model is verified by quantitative comparison with the high fidelity results from FEM. With these validation and verification steps, the results in chapter 5 can be used to draw conclusions of this study.

4.1. Propeller Blade Geometry

The selection of the propeller used for verification is critical for the outcomes of the verification process. The propeller used as a baseline in this study is the TUD-XPROP, also known as XPROP (figure 4.1). CFD and experimental results are available for this particular propeller, allowing the validation and verification of the numerical models used, and thereby results can be assessed with confidence.

The diameter of XPROP is 0.4064 m, and the number of blade is varying from 3 to 6, depending upon whether the propeller is used in a regenerative or a propulsive mode. Although the aeroacoustic effects are more pronounced with a larger number of blades, a 6-bladed propeller is used in the aircraft optimization study. However, for the current validations, a three-bladed propeller is used because it can be used in both the regenerative and propulsive cases, and validations can be performed for both. The propeller pitch setting can be changed manually, which changes the geometry of the propeller blade. For the reference case, the pitch setting was taken to be 20 ° which can be changed depending upon the propulsive or regenerative case. This implies that at the reference radius $r/R_p = 0.7$ (at non dimensional radius = 0.7) pitch setting of the propeller blade is set to 20 °. For numerical analysis, the blades are divided into 25 uniformly distributed cross sections across the blade. Each of these XPROP-blade cross sectional shapes is depicted in the Appendix A. Figure 4.2 depicts the radial distributions of twist and chord for a single XPROP blade. XPROP can be classified as a straight-bladed propeller since no blade sweep was present in the design.

From the standpoint of structures, it is important to note that a portion of the propeller blade is located in the spinner of the blade model, as shown in the figure 4.3. This is significant because the low fidelity model is designed for an isolated blade, and since the initial two airfoil sections are located inside the geometry's spinner, they will not be able to produce any thrust or torque in the high fidelity simulation. Indeed, this can result in minor differences between the high and low fidelity results. In order to ameliorate differences, the loads are extracted from high fidelity CFD simulations and are imported to the low fidelity simulation, such that both the models have same aerodynamic loads. The airfoil geometries corresponding to all 25 radial stations are imported into the program to build the low fidelity model for XPROP. After providing a chord distribution, the program evaluates important centers including centroid, center of pressure, pitch twist axis, and aerodynamic centers. Each airfoil geometry is then twisted and rotated with the pitch angle shown in the figure 4.2. All the centers, for rotated axis can be directly computed by multiplying the rotational matrix with the coordinates of the centers.

(a) TUD XPROP-3 Propeller

(b) TUD XPROP-6 Propeller

Figure 4.1: Propeller Models[14]

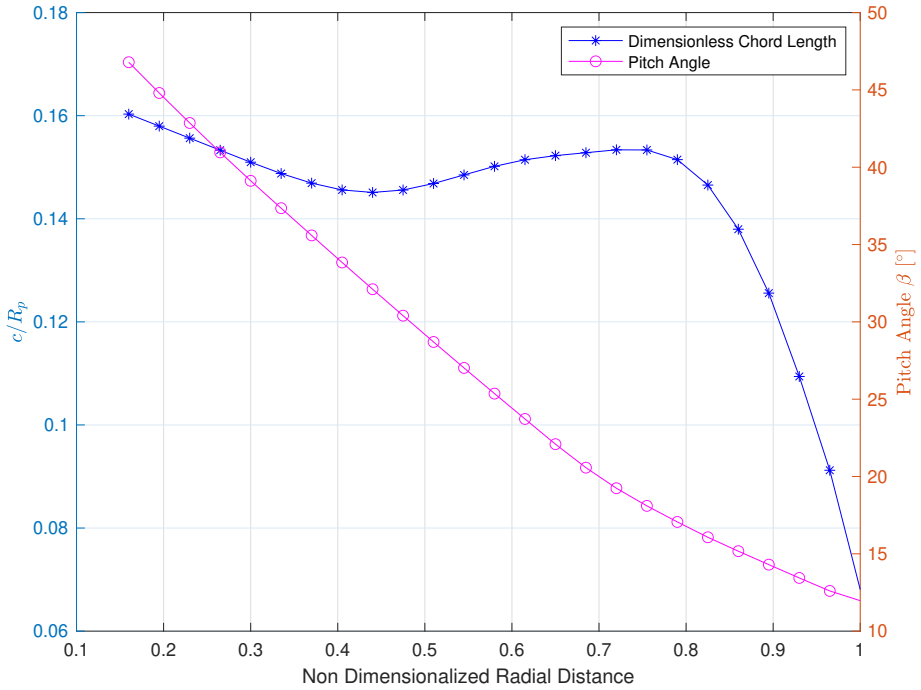

Figure 4.2: Radial distribution of pitch and chord of XPROP blades

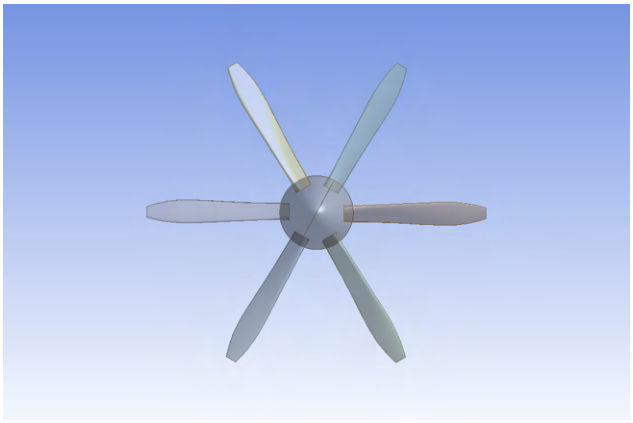

Figure 4.3: CAD Geometry of XPROP propeller

Operating Condition	Propulsive	Regenerative
Advance Ratio (J)	1.2	1.9
Velocity (v)	30	30
Pitch Angle (β_0)	30	30
Blade Count (B)	3	3

Table 4.1: XPROP: Operating conditions for propulsive and regenerative mode

A general rotational matrix, at a radial station with pitch angle θ can be given:

$$R(\theta) = \begin{bmatrix} \cos(\theta) & -\sin(\theta) \\ \sin(\theta) & \cos(\theta) \end{bmatrix} \tag{4.1}$$

And, the new coordinates of the centers and airfoil profile is evaluated using equation 4.2

$$\begin{bmatrix} x' \\ y' \end{bmatrix} = \begin{bmatrix} \cos(\theta) & -\sin(\theta) \\ \sin(\theta) & \cos(\theta) \end{bmatrix} \cdot \begin{bmatrix} x \\ y \end{bmatrix} \tag{4.2}$$

Neutral axis of the section is assumed to be parallel to the chord and passing through the centroid of airfoil section. The moment of inertia is computed in the program, about the centroid using a non dimensionalized airfoil section, as explained in the chapter 3. Figure 4.4 depicts a XPROP blade designed for the low fidelity code using the given radial airfoil sections, with reference pitch setting β_0 =20 °.

Varying the reference pitch angle β_0 can cause the propeller to switch from propulsive to regenerative mode. In the propulsive mode, the thrust and torque produced by the propeller are positive as an amount of forward force is required to propel the airplane. While in regenerative mode, a negative thrust and torque are produced, which can assist the aircraft in slowing down and generating energy by producing negative torque that can be stored. The table 4.1 shows the XPROP blade operating conditions for the propulsive and regenerative cases for current validations. It is important to note that for the validations, the same pitch angle is considered for both modes in order to obtain a contrast between two cases with the same geometry.

The XPROP propeller blade modeled by the low fidelity model for reference pitch angle 20 ° is given in the figure 4.5. When operated at $J = 1.2$, this blade is in propulsive mode, but when operated at $J =$ 1.9 , it is in regenerative mode.

4.2. High Fidelity Simulation Setup

In this section, the high fidelity simulation setup is described. For this case, one way coupling method is used for aerodynamic simulations and structural simulation is performed. This means that the CFD simulation of XPROP was performed using ANSYS ®Fluent 2019 R3 to import the aerodynamic

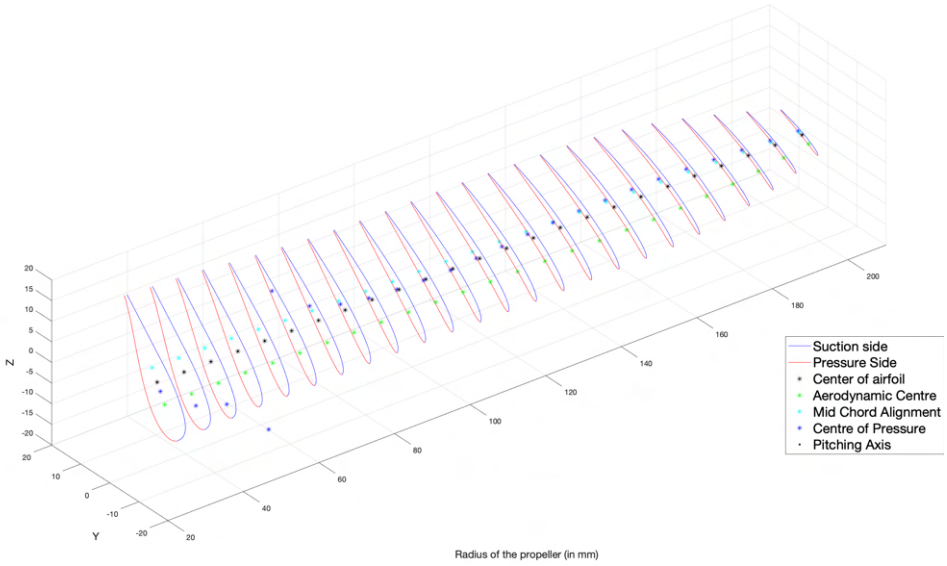

Figure 4.4: XPROP blade from the low fidelity model β_0 =20°

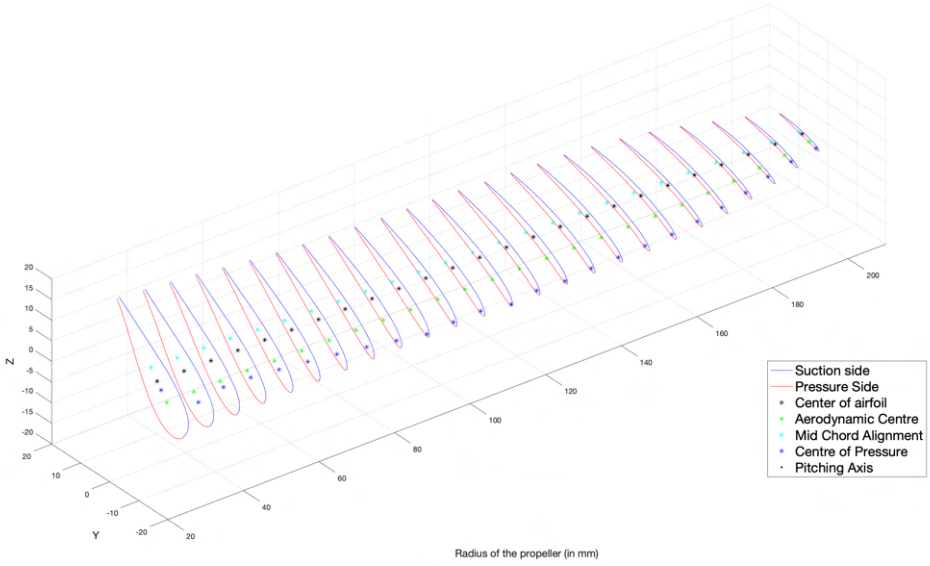

Figure 4.5: XPROP blade from the low fidelity model β_0 =30°

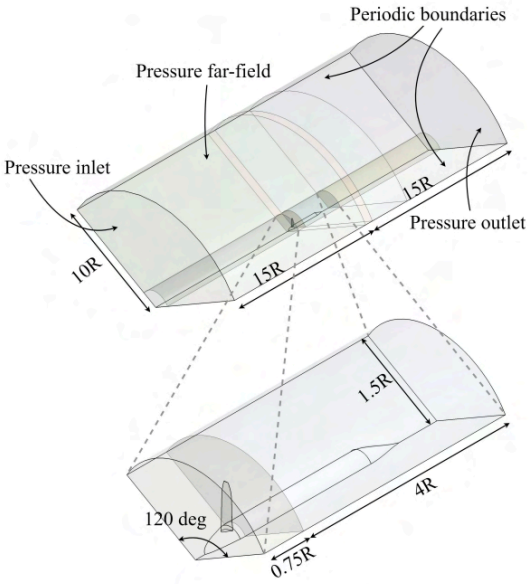

Figure 4.6: Numerical Domain and Boundary Conditions[14]

loads and later, these loads were imported to the structural simulations in Static Structural Module of ANSYS®Mechanical 2019 R3.

4.2.1. CFD Simulations

CFD simulations are required for obtaining the aerodynamic results for the propeller. These simulations were provided from Goyal et al. [14] and were imported to the ANSYS Workbench ®.

The RANS equations for compressible flow were solved using ANSYS ®Fluent 2019 R3 which is a commercial, unstructured, finite volume, cell-centered solver. Uniform inflow conditions were examined with the simulations solving for a single bladed wedge domain in steady manner using a multi reference frame approach. Figure 4.6 depicts the numerical domain and the boundary conditions used for the both, regenerative and propulsive mode. The height of domain in vicinity of the propeller blade is $1.5R$, and the total height of the domain is $10R$.

Wedge angle is set to 120°, so as the analysis can be done for a single blade. It was also made sure that the boundaries of the domain are sufficiently far away to keep the influence of the boundary conditions on the flow properties near the propeller blade minimum.[12,35] Pressure inlet, pressure outlet, pressure far field boundary conditions were used in combination with a conformal periodic boundary condition for the side boundaries.[14] The propeller blade and spinner was modeled as no slip walls, while the nacelle was modeled as moving wall, to keep it stationary in the absolute frame. The turbulence modeling was based on the Spalart-Allmaras method[36] with a modification proposed by Dacles-Mariani et al. [37].

Grid generation was accomplished with the aid of ANSYS meshing. Triangular wall mesh was used adjacent to no slip wall regions, along with layers of semi-structured prismatic and tetrahedral elements. To reduce the total number of elements, an unstructured hexagonal mesh was created in the slipstream and upstream of the propeller. The first-layer thickness of the inflation layers was adjusted to maintain the $y^+ \leq 1$required by the Spalart-Allmaras turbulence model. The grid density in the entire domain was controlled by no-slip wall refinement and domain volume refinement. The grid dependence study is presented in detail in Goyal et al. [14], while in the present study the domain and simulation is imported for computing the aerodynamic loads on the propeller blade.

The pressure distribution and wall shear stress distribution over the propeller blade for the propulsive mode and regenerative mode case are depicted in 4.7 and 4.8 respectively. Pressure distribution results

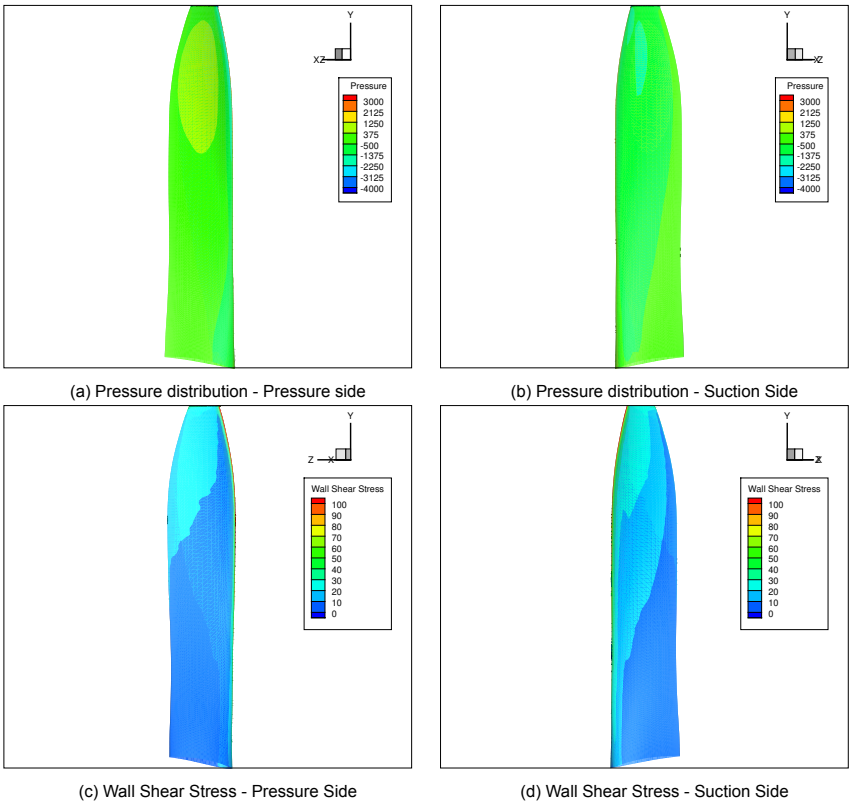

(a) Pressure distribution - Pressure side

(b) Pressure distribution - Suction Side

(c) Wall Shear Stress - Pressure Side

(d) Wall Shear Stress - Suction Side

Figure 4.7: CFD Results for XPROP in propulsive regime $J = 1.2$

can be directly imported into FEM simulations and coupled with structural simulations. Wall shear is, however, ignored in FEM simulations because it is not possible to directly import the wall shear stresses to the structural simulations. Shear stress, on the other hand, is essential for determining aerodynamic loads, which are later fed into the low fidelity model to calculate thrust and torque forces. As a result, these findings are critical for the structural model.

4.2.2. Structural Simulation - FEM

The structural simulations were carried out in the Static Structural module of ANSYS®Mechanical 2019 R3. These simulations were performed on the isolated propeller blade in order to make a clear comparison with low fidelity results, which can only be performed on the isolated blade and not on the entire XPROP geometry. The geometry of the entire propeller is imported, and all bodies other than the single blade are suppressed to create a single bladed geometry. Because the pressure field only corresponds to a portion of the blade, from the spinner to the tip of the blade. A face split command was used to divide the blade faces of XPROP into two parts, one inside the spinner and one outside the spinner. This is depicted in the figure 4.9a.

Following that, a material is chosen and assigned to the propeller blade; for the current study, default material 'Structural Steel' was assigned as the material to the propeller; the structural steel's properties are listed below in the table. 4.2.

The boundary conditions are then described in the analysis. A rotational velocity is given around the XPROP's center (at $0.16R$ distance from the blade's hub). The rotational velocity is estimated using the flight's advance ratio and airspeed. The hub section is fixed to resemble a Cantilever beam, and pressure loadings are imported from CFD simulations and applied to the corresponding suction side, pressure side, trailing edge, and blade tip. It should be noted that the pressure is applied to the portion of the blade that lies outside of the spinner geometry for which pressure fields are available. To import the pressure loads, a profile preserving mapping and triangulation method of weighing is used and

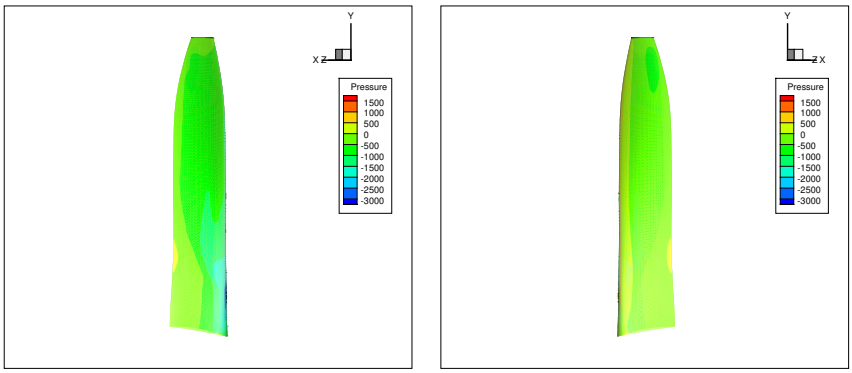

(a) Pressure distribution - Pressure side

(b) Pressure distribution - Suction Side

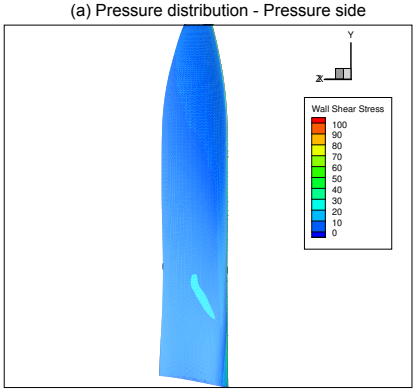

(c) Wall Shear Stress - Pressure Side

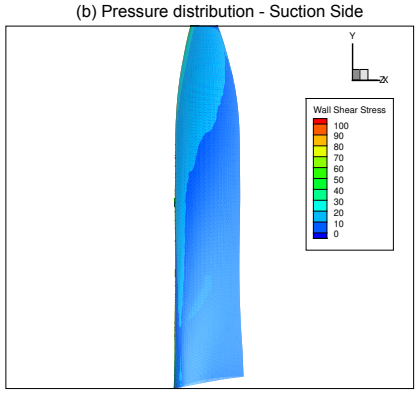

(d) Wall Shear Stress - Suction Side

Figure 4.8: CFD Results for XPROP in Regenerative regime ($J = 1.9$)

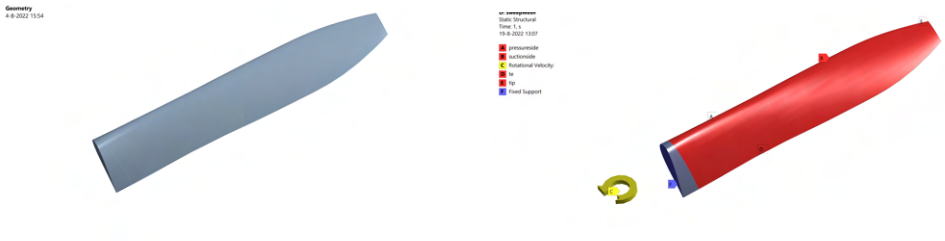

(a) Isolated propeller blade geometry

(b) Boundary Conditions for Structural simulations

Figure 4.9: Imported Loads on the propeller blade

Property	Value
Young's Modulus (Pa)	2e+11
Poisson's Ratio (-)	0.30000
Bulk Modulus (Pa)	1.6667e+11
Shear Modulus (Pa)	7.6923e+10
Isotropic Secant Coefficient of Thermal Expansion	1.2e-05
Compressive Ultimate Strength (Pa)	0
Compressive Yield Strength (Pa)	2.5e+08
Ultimate Strength (Pa)	4.6e+08
Tensile Yield Strength (Pa)	2.5e+08

Table 4.2: Material Properties of Structural Steel, ANSYS ®

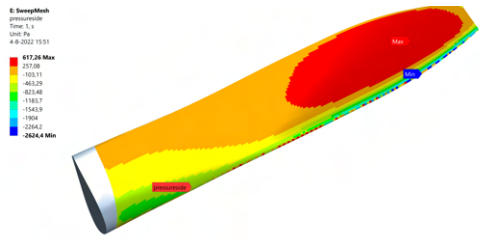

(a) Imported loads - Pressure Side

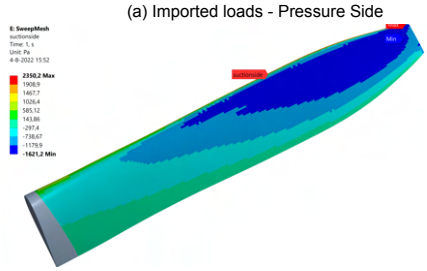

(b) Imported Loads - Suction Side

Figure 4.10: Imported Loads on the propeller blade $J = 1.2$

is given to the nodes of the FEM mesh. Because the pressure field is applied to the surface of the propeller blade, the surface transfer type setting is used. The boundary conditions are shown in the figure 4.9b. Imported Pressure loads on the blade are demonstrated in the figure 4.10. A mesh can be very important in the pressure loadings because the pressure loads are imported and interpolated on the nodes of the FEM mesh from the CFD mesh. As a result, a finer mesh on the pressure and suction sides is required.

FEM Mesh is an important consideration when validating results. As shown earlier in the figure 2.12, the element type and meshing method used can have a significant impact on the result. For the finite element analysis of the propeller blade, an unstructured mesh is required due to the twisted geometry of the blade and the airfoil's non-uniform cross section. The mesh was generated using the 'sweep method' which can easily maintain a high solver accuracy while reducing mesh cell counts significantly. The sweep method generates an initial mesh on the source surface, in this case the hub, using the local sizing method. The mesh is then swept from the source through the body, with an incremental distance or number of divisions specified as input. The source surface mesh is chosen as quadrilateral surface elements, resulting in a hexahedral volumetric mesh. A triangular surface element can also be chosen, resulting in a tetrahedral mesh in the volume. A quadrilateral surface mesh was chosen for more accurate results and was 'swept' from the hub surface to the tip of the blade. For the surface mesh, a 'quadratic' element order was used to encompass the midside nodes and capture the pressure on the blade surface precisely. Figure 4.11 shows a quadrilateral hub surface mesh with the quadratic element order, which was used in the sweep method to generate the mesh. A mesh independence study was performed by varying the element size on pressure, suction side and the fixed hub of the blade.

Mesh Independence Study

In the mesh study, the mesh was refined systematically on both the source surface mesh (Hub), which will be referred to as zone 1, and the pressure side, suction side, and tip of the blade, which will be referred to as zone 2. To compare different meshes, the element type and order on the surface mesh are also changed. The element size was varied in zone 1 from 3 mm to 0.5 mm, and in zone 2 from 4 mm to 0.8 mm. The number of elements and thus computational time increases significantly as the mesh element size decreases. A maximum stress value [MPa] was used as a mesh study convergence parameter for local convergence in the higher stress region. The total potential energy or total strain energy was used as a convergence parameter for global convergence. A mesh with triangular target surface elements in linear order was also compared to the other meshes for comparison and contrast.

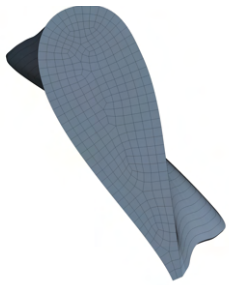

Figure 4.11: Hub Surface mesh

							Surface Mesh Type	
Mesh Number	Size : Zone 1	Size: Zone 2	Element number	CPU Time	Maximum Stress	TPE	Element Order	Element Type
Mesh 1	3 mm	4 mm	2200	4.203 s	16.558 MPa	0.0023082 J	Quadratic	Quadrilateral
Mesh 2	3 mm	3 mm	2900	5.656 s	16.604 MPa	0.0023098 J	Quadratic	Quadrilateral
Mesh 3	2 mm	3 mm	5394	9.375 s	16.616 MPa	0.002311 J	Quadratic	Quadrilateral
Mesh 4	1.5 mm	2 mm	13674	23.484 s	16.57 MPa	0.0023095 J	Quadratic	Quadrilateral
Mesh 5	1 mm	1 mm	55900	78.766 s	16.632 MPa	0.0023125 J	Quadratic	Quadrilateral
Mesh 6	0.5 mm	0.8 mm	257140	366.938 s	16.634 MPa	0.0023126 J	Quadratic	Quadrilateral
Mesh 7	1 mm	1 mm	55900	22.703 s	16.598 MPa	0.0023008 J	Linear	Quadrilateral
Mesh 8	1 mm	1 mm	95976	20.562 s	16.169 MPa	0.0022933 J	Linear	Triangular

Table 4.3: Mesh Independence Study

All mesh study results are presented in the table 4.3. It is worth noting that convergence parameters change significantly when the mesh is changed to linear element order; this is possibly due to the inability of pressure field interpolation on the linear nodes (FEM mesh with less mid nodes unable to interpolate pressure field).

Mesh Convergence parameters are plotted further in the figure 4.12. The meshes with the linear element order, are observed from the figure 4.12b and 4.12a to become an outliers, as the parameters tends to deviate from the other mesh results. From the remaining meshes, mesh with 55900 elements tends to be converged, and the total potential energy and maximum stress parameters tends to be converged thereafter. It is evident from figure 4.12c that computational time increases largely, if the mesh is refined more. Hence, the mesh with 55900 elements corresponding to Mesh 5 from the table 4.3 is chosen for the further analysis.

The figure 4.13 depicts a final converged mesh for both propulsive and regenerative regimes. It is also worth noting that the mesh is automatically coarser near the hub surface because no pressure fields are imported near the hub, whereas it becomes denser in regions away from the hub. This is a meshing feature of the Sweep function, and the software automatically meshes the blade accordingly.

4.3. Low Fidelity Model Verification

In this section, the structural predictions by FEM and low fidelity methods are compared to analyze their reliability in the propulsive and the regenerative regimes. Flowchart in figure 4.14 explains the process of validations of the low fidelity structural code.

For the validations, BEM model with higher accuracy is available,[14] therefore, for the aerodynamic loadings in the low fidelity structural model, data from corrected BEM model was imported. Moreover, the aerodynamic loadings were also computed by post processing the CFD simulations in Tecplot ®and compared with the given data before being imported to Low fidelity model to compare differences. Python scripts for post processing of CFD results are provided in Appendix E. It should be noted that CFD data includes the effects of wall shear stress, which cannot be imported into ANSYS ®High Fidelity FEM simulations. As a result, two cases—one with Pressure and Wall Shear included and another with just Pressure field—were evaluated in post-processing CFD simulations. The comparison between the low fidelity BEM findings and the post-processed CFD findings for the XPROP in the propulsive regime is shown in the figure 4.15. It is clear that wall shear has a negligible effect on the aerodynamic loads and can be disregarded. The structural model was validated using CFD data without wall shear in order to estimate aerodynamic loads, which are exactly the same loads that were applied to the high fidelity

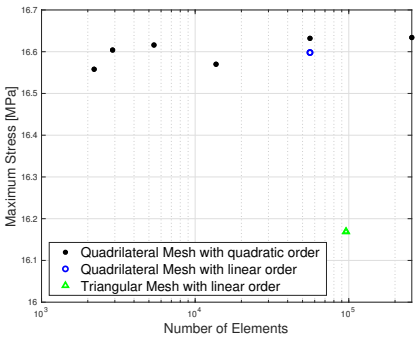

(a) Local Convergence - Maximum Stress

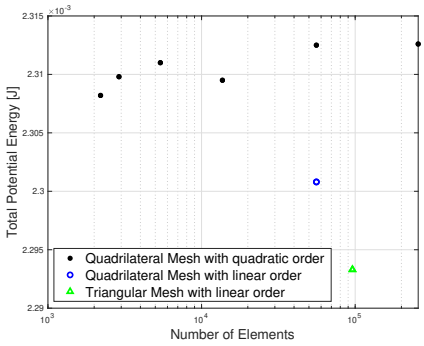

(b) Global Convergence - Total Potential Energy

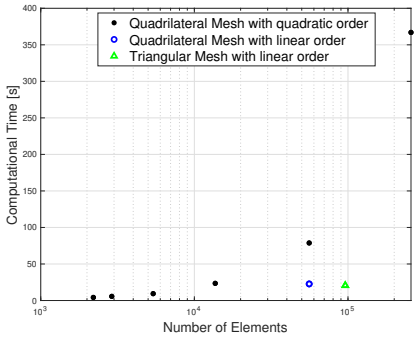

(c) Computational Time Mesh

Figure 4.12: Mesh Independence Study

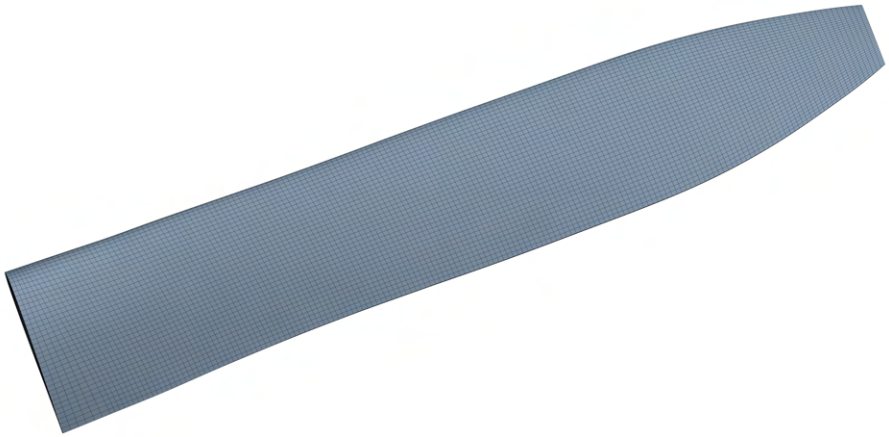

Figure 4.13: XPROP converged mesh

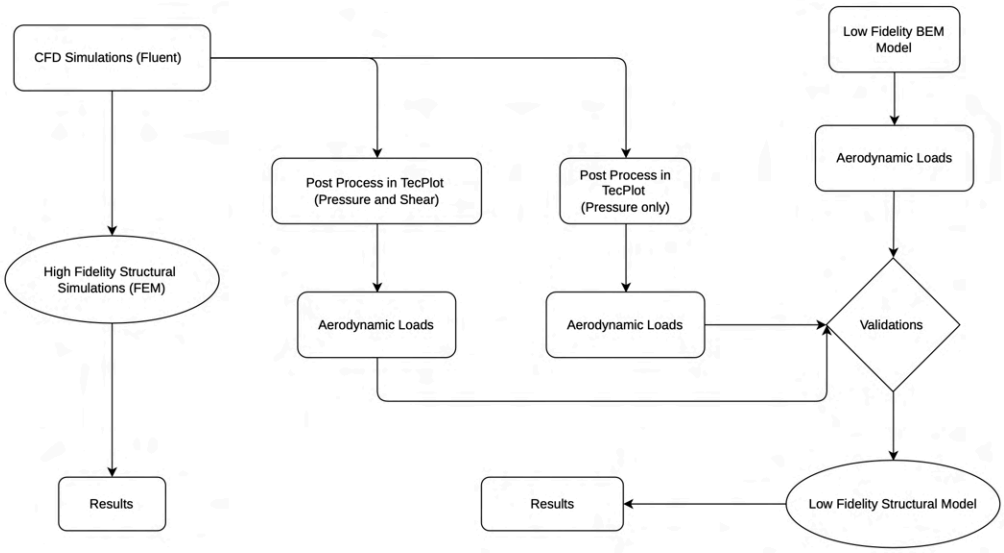

Figure 4.14: Validation Process for the low fidelity structural model

simulations. Similar results for the propeller in the regenerative regime were also achieved, proving that a low fidelity BEM model is effective and produces same results.

4.3.1. Propulsive Regime

Both the numerical methods are compared and contrast for the propulsive regime, at $v = 30\,\text{m/s}$, $\beta_0 = 30\,^\circ$ and an advance ratio $J = 1.2$

It should be noted that blade profile in low-fidelity model is the exactly opposite of high-fidelity model, hence is a mirror image as seen in the figures. The structural results of high and low fidelity models are examined and compared. To begin the comparison, only centrifugal loading were compared, as shown in the figure 4.16. It is evident from the figure, that the low fidelity results matches closely, with FEM simulations with the maximum stress of 11.26 MPa occurring at 40% radial section. It is important to highlight that, in contrast to FEM results, the low fidelity model is unable to correctly depict contours

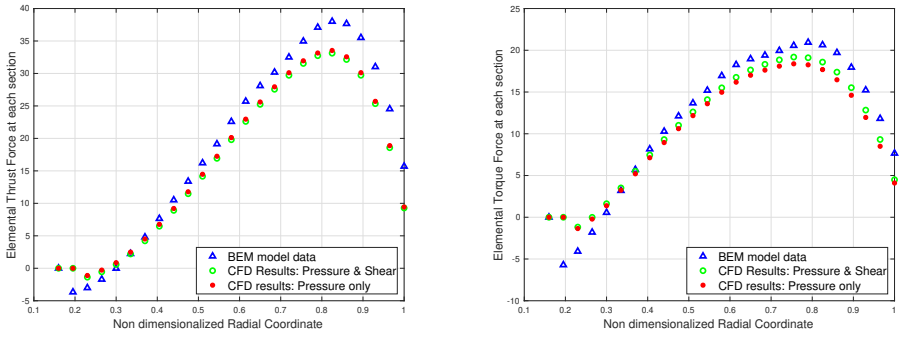

(a) Elemental Thrust evaluated from BEM and CFD methods (b) Elemental Torque evaluated from BEM and CFD methods

Figure 4.15: Aerodynamic Load validations for XPROP in propulsive regime

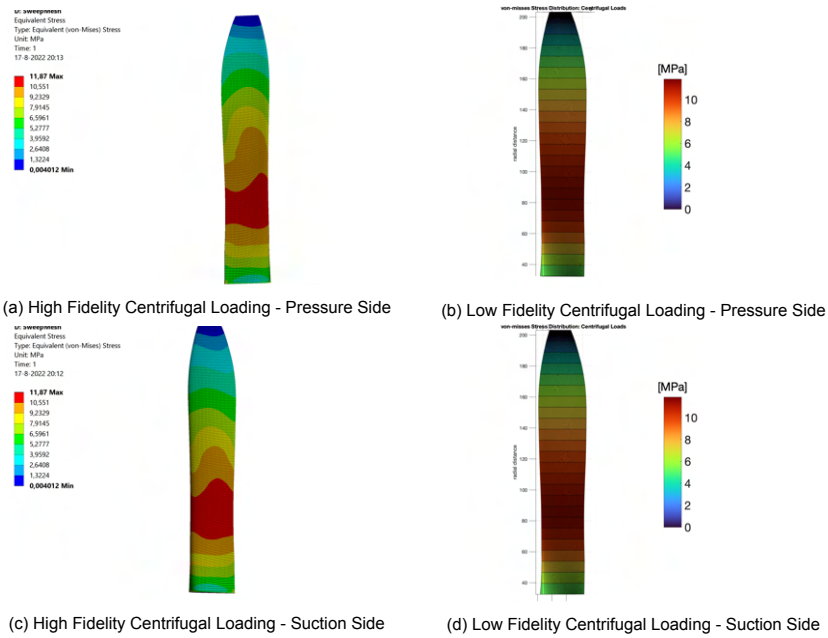

(a) High Fidelity Centrifugal Loading - Pressure Side

(b) Low Fidelity Centrifugal Loading - Pressure Side

(c) High Fidelity Centrifugal Loading - Suction Side

(d) Low Fidelity Centrifugal Loading - Suction Side

Figure 4.16: Equivalent von-Mises Stress in Propulsive Regime: Centrifugal Loadings

due to its inability to interpolate stress between two radial sections.

The following analysis evaluated purely aerodynamic loadings without centrifugal loads, as illustrated in the figure 4.16. It was discovered that the low fidelity model correctly predicts maximum stresses with an error of less than 2 percent. The maximum von-Mises stress in the blade determined using FEM was found out to be 6.21 MPa, compared to 6.1 MPa in the low fidelity model. The low fidelity model captures the trends fairly well, as shown by the contours in 4.16.

Finally, both aerodynamic and centrifugal loads were combined to replicate pragmatic propeller blade loads, and both models were compared. The acquired results are presented in the figure 4.18, which indicates a comparable pattern between two models. The low fidelity model underpredicts the von-Mises stresses by roughly 2 percent when compared to the FEM model, owing to small variations in the aerodynamic and centrifugal stress. It reliably predicts the general stress distribution trends yet again with maximum stress varies from 16.28 MPa in the low fidelity model to 16.63 MPa in the FEM model. These variances are primarily caused by the following factors:

1. The cantilever beam model is unable to appropriately estimate the stress distribution. In the low fidelity model, aerodynamic load is assumed to be a point load, whereas in high fidelity simulations, aerodynamic force is dispersed throughout the propeller blade.

2. The current model does not account for changes in propeller stress caused by deflections. The propeller blade could deflect from its original shape as stress increases, resulting in a change in bending moments that is not considered in the low-level model. This effect is more pronounced when extremely high stress is present (as in swept blades), resulting in high deflections.

4.3.2. Regenerative Mode

Similar to Propulsive case, a validation was done for the regenerative case as well. Regenerative regime was operated at at $v = 30$ m/s, $\beta_0 = 30\,^\circ$ and an advance ratio 1.9.

The stress distribution in the regeneration regimes was also investigated first, only with centrifugal loads, as shown in the figure 4.19. It was verified that the low fidelity model accurately estimated the stresses caused by centrifugal loads. The maximum von-Mises stress of 4.49 MPa was recorded at 40 percent of radial section, which corresponds to 4.72 MPa in high fidelity calculations. It should be highlighted that the low fidelity model, due to its inability to interpolate across radial sections, is unable to match the contours but provides an exceptionally near estimate of the stresses.

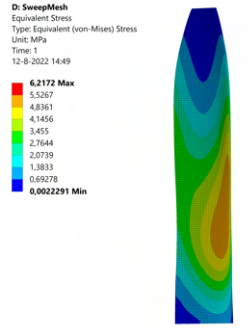

(a) High Fidelity Aerodynamic Loading - Pressure Side

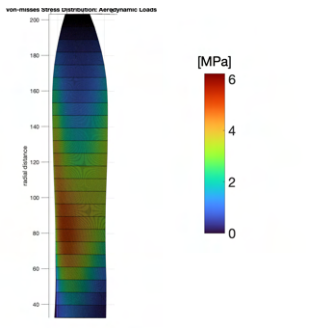

(b) Low Fidelity Aerodynamic Loading - Pressure Side

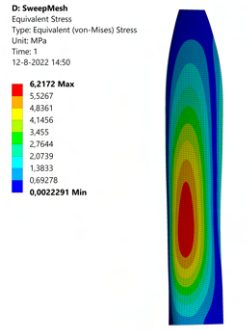

(c) High Fidelity Aerodynamic Loading - Suction Side

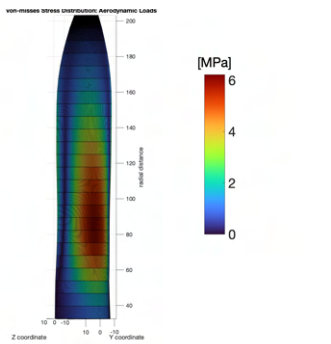

(d) Low Fidelity Aerodynamic Loading - Suction Side

Figure 4.17: Equivalent von-Mises Stress in Propulsive Regime: Aerodynamic Loading

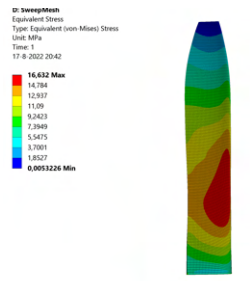

(a) High Fidelity Combined Loading - Pressure Side

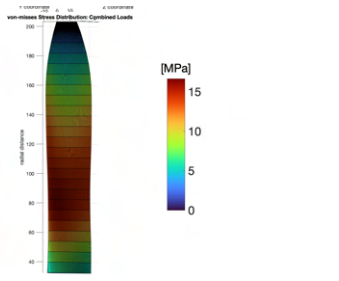

(b) Low Fidelity Combined Loading - Pressure Side

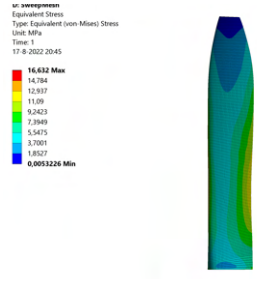

(c) High Fidelity Combined Loading - Suction Side

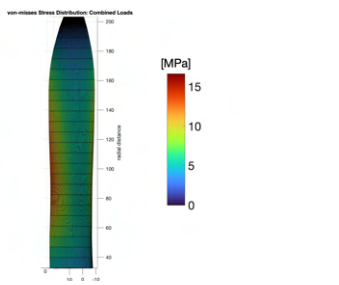

(d) Low Fidelity Combined Loading - Suction Side

Figure 4.18: Equivalent von-Mises Stress in Propulsive Regime: Combined Loading

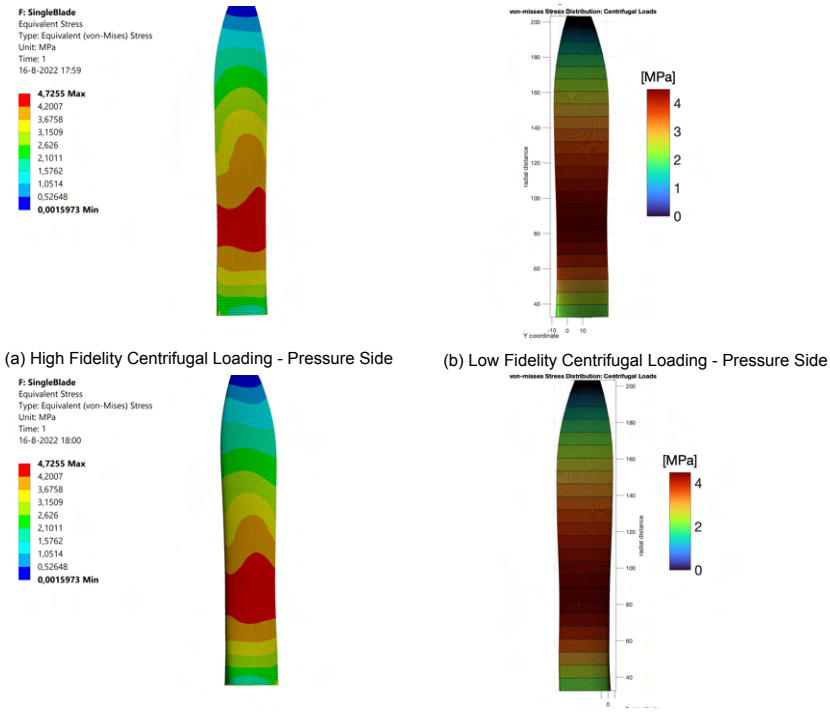

(a) High Fidelity Centrifugal Loading - Pressure Side

(b) Low Fidelity Centrifugal Loading - Pressure Side

(c) High Fidelity Centrifugal Loading - Suction Side

(d) Low Fidelity Centrifugal Loading - Suction Side

Figure 4.19: Equivalent von-Mises Stress in Regenerative Regime: Centrifugal Loadings

Regime	Loading	Maximum Stress : High Fidelity	Maximum Stress : Low Fidelity	Error Margin
Propulsive Mode	Centrifugal Loads only	11.87 MPa	11.26 MPa	5.139%
	Aerodynamic Loads only	6.21 MPa	6.1 MPa	1.77%
	Combined Loads	16.632 MPa	16.28 MPa	2.11%
Regenerative Mode	Centrifugal Loads only	4.72 MPa	4.49 MPa	4.87%
	Aerodynamic Loads only	2.74 MPa	2.89 MPa	-5.47%
	Combined Loads	7.15 MPa	7.31 MPa	-2.18%

Table 4.4: Comparison of High-fidelity and low-fidelity maximum stresses

The stress distribution due to purely aerodynamic loads was then investigated in the following analysis. The results are illustrated in figure 4.20, where it is observed that the low fidelity model appropriately quantifies the stress distributions, but over predicts the maxima by 5 percent. Low fidelity model replicates the main trends of stress distribution, the maximum von-Mises stress in the low fidelity model differs from 2.89 MPa in the low fidelity model to 2.74 MPa in the high fidelity simulations.

Finally, to replicate propeller blade loads, both aerodynamic and centrifugal loads were combined, and both models were compared. The obtained results are shown in the figure 4.21, which shows a similar pattern between two models. Due to small differences in the aerodynamic and centrifugal stress distribution, the low fidelity model overpredicts the von-Mises stresses by approximately 2.3 percent when compared to the FEM model. It predicts the basic stress distribution trends once more, however the maximum stress changes from 7.31 MPa in the low fidelity model to 7.15 MPa in the high fidelity FEM model.

Table 4.4 displays the comparison of high-fidelity and low-fidelity model in a tabular form.

Following validations from the straight blade regenerative and propulsive regimes, it is reasonable to conclude that the low-fidelity model is accurate enough to capture major trends in stress distribution. It offers a robust, fast and precise structural tool to produce stress distributions, which can be easily employed in the aerodynamics and aeroacoustics framework to perform the design optimizations.

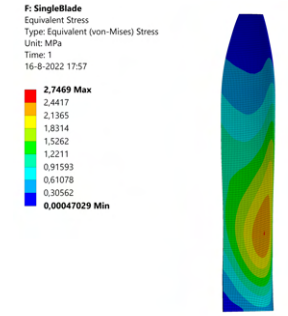

(a) High Fidelity Aerodynamic Loading - Pressure Side

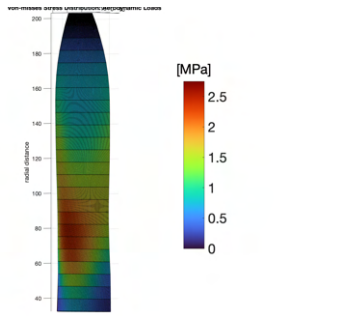

(b) Low Fidelity Aerodynamic Loading - Pressure Side

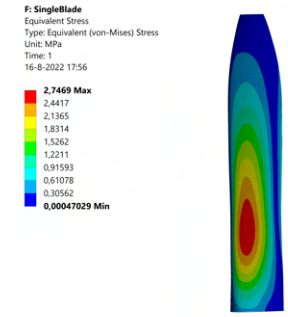

(c) High Fidelity Aerodynamic Loading - Suction Side

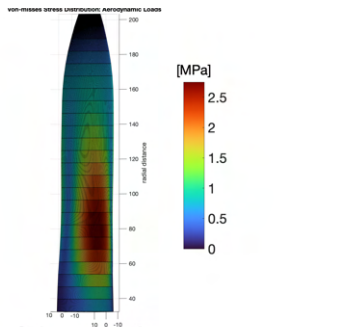

(d) Low Fidelity Aerodynamic Loading - Suction Side

Figure 4.20: Equivalent von-Mises Stress in Regenerative Regime: Aerodynamic Loading

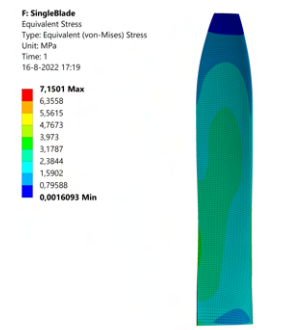

(a) High Fidelity Combined Loading - Pressure Side

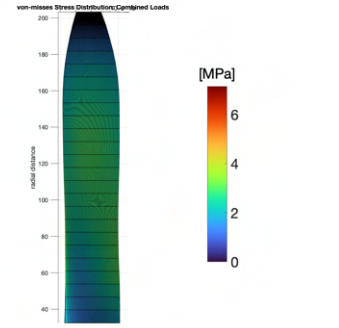

(b) Low Fidelity Combined Loading - Pressure Side

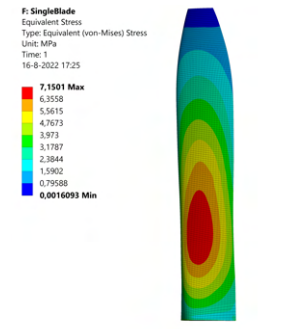

(c) High Fidelity Combined Loading - Suction Side

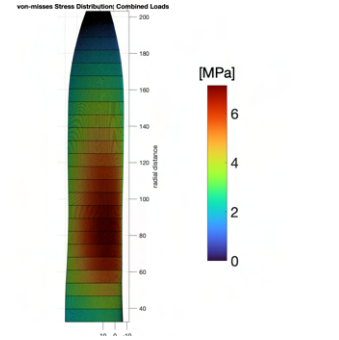

(d) Low Fidelity Combined Loading - Suction Side

Figure 4.21: Equivalent von-Mises Stress in Regenerative Regime: Combined Loading

5

Sensitivity Study of Structural Performance

The numerical findings of the low fidelity model are presented in this chapter, and the variation of stress distribution with various physical parameters is investigated. Based on these findings, the numerical model is further consolidated by comprehending the physics underlying the structural analysis of a propeller blade. The advance ratio (J) was altered and investigated in the section 5.1, the reference propeller pitch(β_0) was varied in the section 5.2, and the influence of sweep (γ_0) on structural stress was investigated in the section 5.3.

5.1. Varying Advance Ratio

To begin, the propeller's advance ratio was varied and stress distribution over the blade was examined. This is done while maintaining a constant airspeed, implying that the rotational velocity of the propeller was altered. The table 5.1 shows various operating locations with varying rotational velocity. The rotational velocity (ω) of the propeller changes as the advance ratio (J) is altered, causing the centrifugal loads to vary. Furthermore, changing the rotational speed alters the tangential velocity at each radial section (V_t) of the propeller, which changes the angle of attack (α) and hence the aerodynamic loadings of the propeller. Therefore, as a result of the change in propeller advance ratio, both the aerodynamic and centrifugal load changes, resulting in a change in von-Mises stress and deflections in the propeller blade. It is important to keep in mind that the blade is chosen to be XPROP with reference blade pitch β_0 was set to 30°.

It is expected that when the advance ratio decreases, the centrifugal loads and, consequently, the centrifugal moment and von-Mises stress across the blade will increase. For the detailed comparison the three cases with $J = 0.6$, $J = 0.9$ and $J = 1.2$ are discussed in detail. It is worth mentioning that direct moments due to centrifugal forces (M_C), Thrust Forces (M_T) and the torque forces (M_Q) are termed as Global Moments, whilst the moments corresponding to the local axis in rotated frame M_η, M_ξ and M_ζ are termed as Local Moments. The maximum von-Mises stress along the radial stations with varying advance ratios is depicted in Figure 5.1. The von-Mises stress decreases with increasing

Advance Ratio (J)	Propeller (RPM)	Airspeed (m/s)
0.6	7382	30
0.7	6327	30
0.8	5536	30
0.9	4921	30
1	4429	30
1.1	4026	30
1.2	3691	30

Table 5.1: Operating points with varied advance ratio

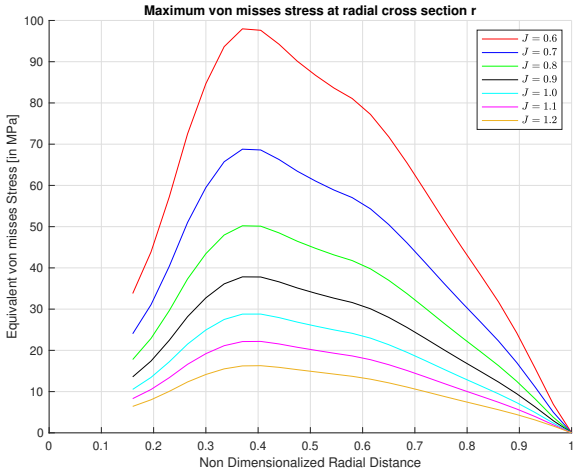

Figure 5.1: Variation of maximum von-Mises stress with varying advance ratios

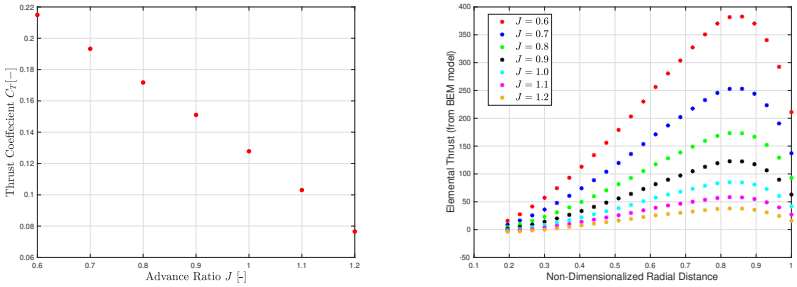

(a) Variation of Thrust Coefficient with Advance ratio

(b) Variation of elemental thrust with Advance ratio

Figure 5.2: Varying aerodynamic loading with advance ratio

advance ratio and is proportional to the square of rotational velocity (ω), similar to the centrifugal loads.

It is observed that with increase in advance ratio, the thrust coefficient decreases, as the rotational speed of propeller blade decreases, which ultimately leads to reduction in elemental thrust and torque forces. This is depicted in the figure 5.2a, where thrust coefficient (C_T) is plotted at varying advance ratios (J). Elemental Thrust forces are also plotted at each section of the blade, and is displayed in the figure 5.2b. Therefore, with increase in advance ratio, both aerodynamic and centrifugal loads decreases, which results in lower von-Mises stress on the propeller blade.

5.1.1. Global and Local Bending Moments

All the advance ratios ranging from $J = 0.6$ to $J = 1.2$, falls into the category of propulsive regime. This is evident from the figure 5.2a, where the thrust coefficients are illustrated, as the thrust coefficients of all the regimes is positive, propeller is operating in propulsive regime. With increase in advance ratio of propeller, rotational velocity of the propeller decreases. This causes weaker centrifugal forces and, as a result, decreased von-Mises stress.

The aerodynamic moments diminishes from the hub part of the blade to the tip and become zero at the tip, while the centrifugal moments remains zero. This occurs because the airfoils are stacked with their centroid along the same axis, resulting in a zero moment about the neutral axis (passing through the centroid). With increase in advance ratio, rotational velocity decreases, which in turn, also reduces inflow velocity at every radial section. This results to decrease in lift and drag at the airfoil sections, which ultimately leads to reducing the aerodynamic forces and aerodynamic bending moments namely; thrust and torque moments as shown in the figure 5.3c for a higher advance ratio of

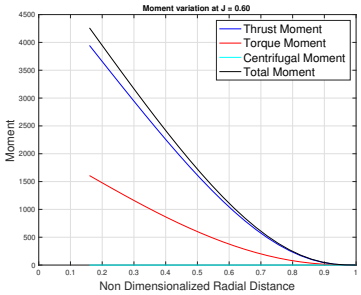

(a) Variation of Global Moments - Advance ratio 0.6

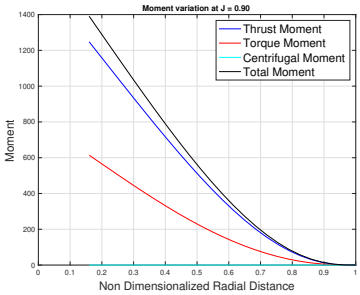

(b) Variation of Global Moments - Advance ratio 0.9

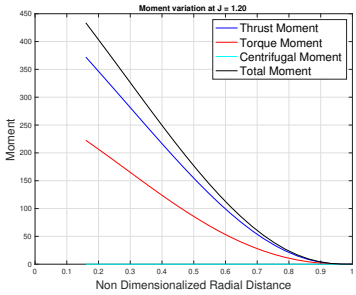

(c) Variation of Global Moments - $J = 1.2$

Figure 5.3: Variation of Global Moments for varying advance ratios

$J = 1.2$. The variation of global moments are illustrated in the figure 5.3, and variation of local moments in the local Cartesian system is given in the figure 5.4. It is to be noted that local moments, remains in the negative direction with magnitude diminishing towards the tip of blade. The torsional moments are also shown, however the magnitude of the torsional moment remains low in all the cases, and it do not produces significant shear stresses.

5.1.2. Stress Distribution at hub

Figure 5.6 depicts the variation of von-Mises stress on the propeller hub section with varying advance ratios. It is interesting to note that the pressure side of the propeller blade has larger stresses than the suction side, which is explained by the negative local moments (see figure 5.4). On the suction side, due to the negative local bending moments stress are compressive in nature, while on the pressure side stresses are tensile. Along with these two kinds of stress, the direct centrifugal stress also acts on the propeller which is tensile in nature. This results in adding bending stress on suction side and subtracting bending stresses on pressure side to the direct centrifugal stress. As the advance ratio is increased, difference between stress at suction side and pressure side reduces to lower values, implying that the bending moments are decreased, and results in lower bending moment stresses. It is also evident from the figure 5.6 that direct centrifugal stress dominates over the bending moment stresses in all these cases, as the overall stress remains tensile in nature. Therefore, it can be said that the centrifugal loads dominates over the aerodynamic forces in this case.

5.1.3. Stress distribution on propeller blades

The stress distribution across the blade are depicted in the figure 5.7.

For the case of lower advance ratio of $J = 0.6$, maximum von-Mises stress of 96 MPa occurs on the pressure side of the blade at around 40 % of the radial section, which diminishes as the radius increases towards the tip of blade as seen in the figure 5.7a. On the suction side, the stress are significantly lower than the pressure side, however, at the trailing edge von-Mises stress increase to higher values due to the aerodynamic moments. The suction side remains with low stress as the centrifugal tensile stresses are neutralized with the compressive stresses due to bending moments as displayed in the figure 5.7b.

As the advance ratio is increased to $J = 0.9$, maximum von-Mises stress decreases to 38 MPa,

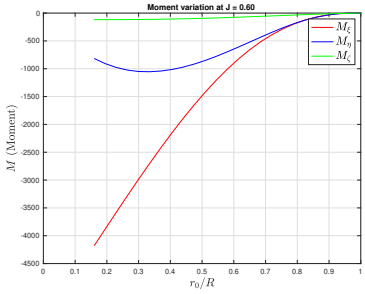

(a) Variation of Local Moments - Advance ratio 0.6

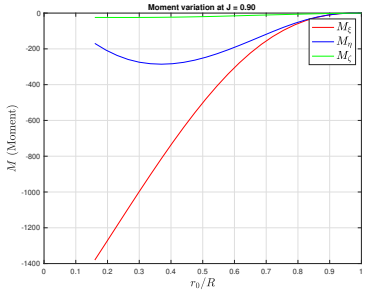

(b) Variation of Local Moments - Advance ratio 0.9

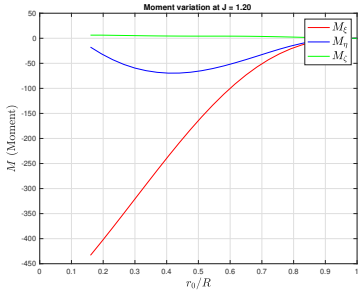

(c) Variation of Local Moments - $J = 1.2$

Figure 5.4: Variation of Local Bending Moments for varying advance ratios

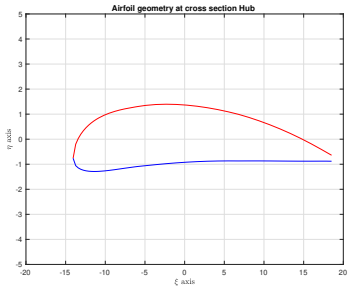

Figure 5.5: Hub profile in the local Cartesian system

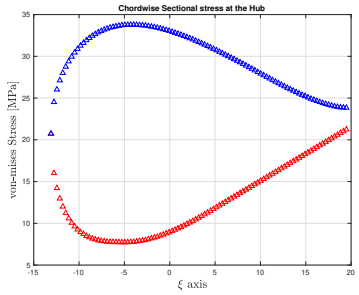

(a) Variation of the von-Mises stress at the hub of the propeller

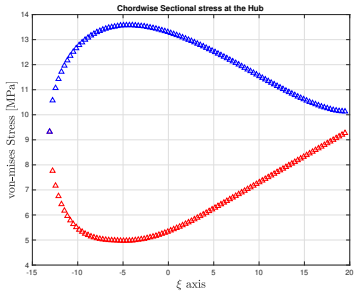

(b) Variation of the von-Mises stress at the hub of the propeller

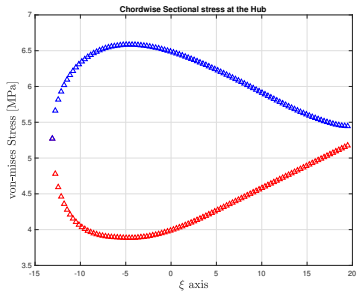

(c) Variation of the von-Mises stress at the hub of the propeller

Figure 5.6: Variation of the von-Mises stress in Local axis with varying advance ratios J

occurring on the pressure side (figure 5.7c), at similar radial section and diminishing towards the tip of blade. Suction side of blade is displayed in the figure 5.7d, which remains fairly uniform with lower stresses, in the center and a stress concentration zone on the trailing edge around 40 % of the radial section.

For further higher advance ratio $J = 1.2$, maximum von-Mises stress decreases to 17 MPa. Similar to the other two cases, maximum stress occurs on the pressure side as well (figure 5.7e), at a radial section of 40 % and stress diminishing towards the tip of blade. However, it is interesting to observe the suction side in figure 5.7f, where the stress varies from trailing edge to leading edge. With a decrease in rotational velocity, the centrifugal stress decreases. Aerodynamic bending moments nullifies the centrifugal stresses and thus suction side remains fairly uniform, with a slight increase in stresses near the trailing and leading edge of the blade.

Appendix B includes the propeller blade stress contours for all advance ratios ranging from 0.6 to 1.2 .

5.2. Varying Reference Pitch Angle

In order to have a closer look at the variation of aerodynamic loads while maintaining the centrifugal load constant, the reference propeller pitch (β_0) sensitivity study needs to be done. At a constant advance ratio, as the propeller pitch is varied, the angle of attack at propeller sections varies, which results in varied aerodynamic performance and loads. Hence, the reference pitch of the propeller is modified as the next parameter.

The propeller reference pitch β_0 is defined at a radial section of 70 percent, and same twist angle is given to the blade as last case, which results in varying the angle of attack α at all the radial sections. This is accomplished while maintaining constant airspeed 30 m/s at an advanced ratio of 1.2 . This particular advance ratio was chosen so that the propeller blade can be in propulsive or regenerative regime depending upon the reference propeller pitch. Thus with a constant advance ratio, and varying propeller pitch, centrifugal stresses remain constant while aerodynamic loads change, resulting in a change in von-Mises stress and propeller blade deflections. The reference propeller pitch varies from

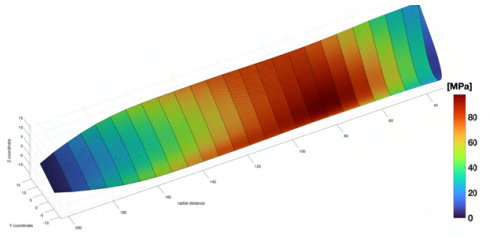

(a) von-Mises stress distribution Pressure Side - $J = 0.6$

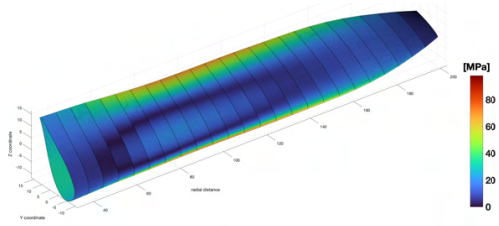

(b) von-Mises stress distribution Suction Side - $J = 0.6$

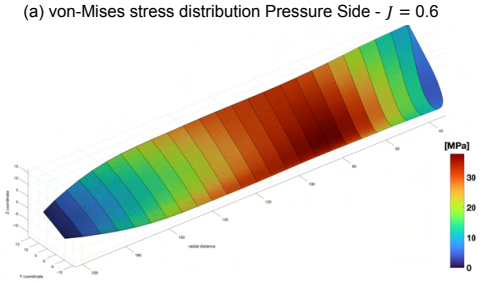

(c) von-Mises stress distribution Pressure Side - $J = 0.9$

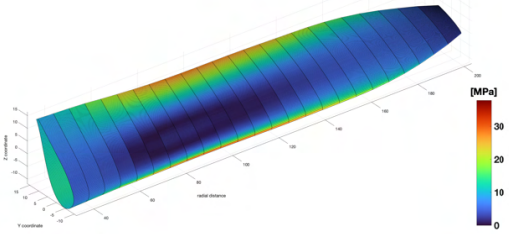

(d) von-Mises stress distribution Suction Side - $J = 0.9$

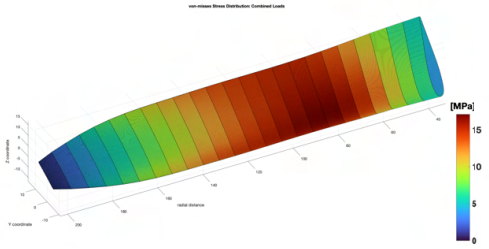

(e) von-Mises stress distribution Pressure Side - $J = 1.2$

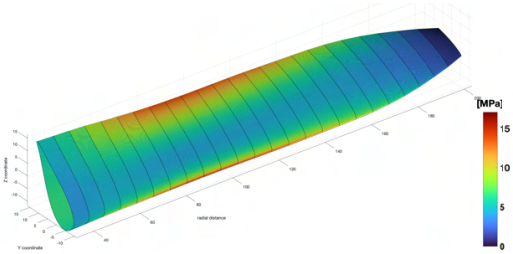

(f) von-Mises stress distribution Suction Side - $J = 1.2$

Figure 5.7: Stress Distribution on the propeller blade with varying advance ratios J

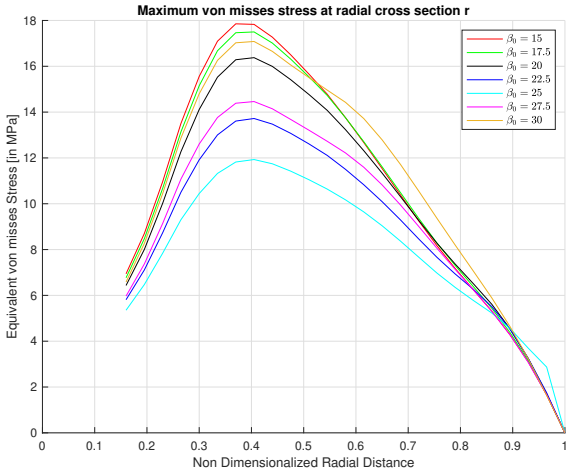

Figure 5.8: Maximum von-Mises stress on radial sections with varying Reference pitch

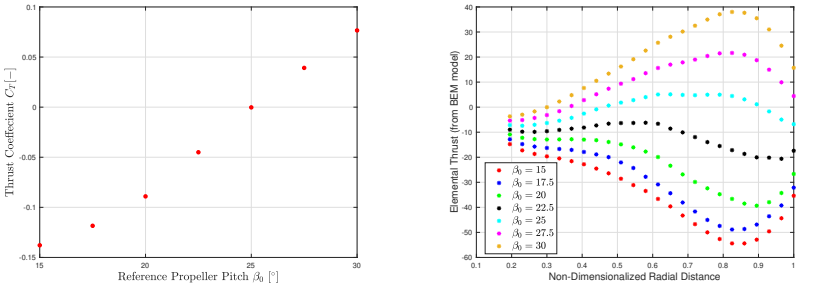

(a) Variation of Thrust Coefficient with Propeller pitch

(b) Variation of elemental thrust with Propeller pitch

Figure 5.9: Varying aerodynamic loading with propeller pitch

β_0 = 15° to 30°. The figure 5.8 depicts the variation of maximum von-Mises stresses over the radial sections with change in reference pitch. Interestingly, when the reference pitch is increased from 15° to 25°, the von-Mises stress decreases initially, but as the reference pitch is increased further from 25° to 30°, the maximum stress grows. The aerodynamic loads from the BEM model shows that for lower pitch angles (β_0 = 15° and 25°), elemental thrust at radial sections is negative, resulting in negative thrust and torques in the lower pitch angles, implying that the propeller is operating in the regenerative regime.

Variation of the Thrust Coefficient (C_T) with reference propeller pitch (β_0) is depicted in the figure 5.9a, it is evident that with increase in propeller pitch, the thrust coefficient increases, and it becomes positive at propeller pitch of 25° and higher, implying that propeller is operating in propulsive regime after 25° propeller pitch. It is also observed in the figure 5.9b, where the elemental thrust is plotted with radial sections at varying propeller pitch. It is evident from the figure that propeller pitch β_0 = 25° to 30°, provides positive elemental thrust forces, implying propulsive regime.

In order to understand the flow physics and structural stresses, the three cases with pitch 15°, 22.5° and 30° are discussed in detail in the following sections. The case of pitch 15° falls into regenerative regime while 30° propeller pitch case falls into propulsive regime.

5.2.1. Global and Local Bending Moments

In this section, variation of the global and local moments for varying propeller pitch is discussed. The global moments in all three cases follows a similar pattern as of varying advance ratios and are depicted in the figure 5.10. Global moments diminishes towards the tip of the blade. As the propeller pitch

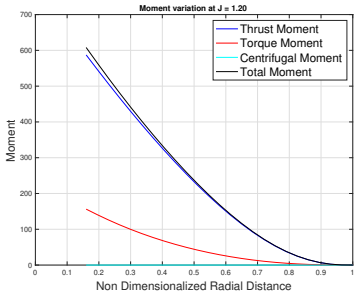

(a) Variation of Global Moments - β_0 = 15 °

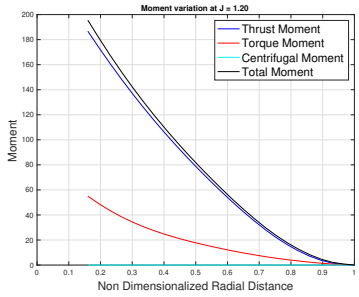

(b) Variation of Global Moments - β_0 = 22.5 °

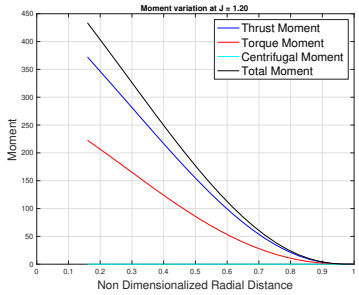

(c) Variation of Global Moments - β_0 = 30 °

Figure 5.10: Variation of Global bending moments with propeller pitch

increases, the global moment decreases first for the case of $\beta_0 = 22.5\,°$, but later increase, with increase in propeller pitch (for the case of $\beta_0 = 30\,°$). This is due to the magnitude of overall aerodynamic loads, as the propeller pitch is increased from 15 ° to 22.5 °, thrust magnitude decreases (see figure 5.9b) and later increases for the case of 30 °. As the propeller starts to operate from regenerative regime to propulsive regime, magnitude aerodynamic loads on the propeller decreases as it reaches around $C_T = 0$, and then increases for propulsive regime.

Figure 5.11 displays the variation of local bending moments with increase in propeller pitch. It is observed again, that the local moments in magnitude diminished towards the tip of the blade. It is very interesting to observe that sign of the local bending moments is positive in first two cases of β_0 = 15 ° and β_0 = 22.5 °, while bending moment becomes negative in the other case. This is directly an effect of the directions of aerodynamic loads. In the first two cases, the propeller is operating in regenerative regime generating negative thrust, while in the last case the propeller is operating the propulsive regime and producing a positive thrust, resulting in change in signs of local bending moments.

5.2.2. Stress Distribution at Hub

The variation of stress at the hub section is shown in the figure 5.12. In contrast to the advance ratio investigations, propeller is operating in regenerative regime in first two cases of propeller pitch investigations. Due to which, the sign of local moment changes to positive, implying that the bending moments results in producing tensile stresses on suction side and compressive stresses on pressure side, which causes the hub stress to 'flip' upside down as compared to the cases in advance ratio studies. This is depicted in the figure 5.12a and 5.12b. In the last case, the propeller is operating in the propulsive regime and the local bending moments are negative, resulting in the tensile stress on pressure side and compressive stress on suction side, and the hub stress distribution is similar as in the case of advance ratio sensitivity studies as seen in the figure 5.12c.

5.2.3. Stress distribution on propeller blades

The stress distribution across the blade are depicted in the figure 5.13.

For the case of lower propeller pitch of β_0 = 15 °, maximum von-Mises stress of 18 MPa occurs on the suction side of the blade at around 40 % of the radial section, which diminishes as the radius

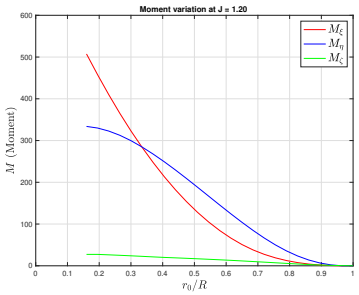

(a) Variation of Local Moments - β_0 = 15 °

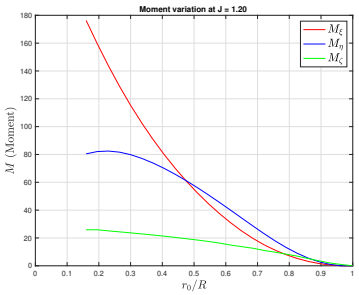

(b) Variation of Local Moments - β_0 = 22.5 °

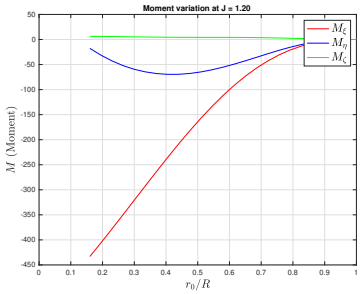

(c) Variation of Local Moments - β_0 = 30 °

Figure 5.11: Variation of Local bending moments with propeller pitch

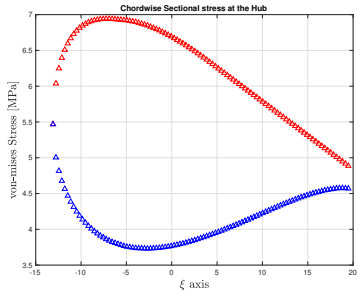

(a) Variation of the von-Mises stress at the hub of the propeller - β_0 = 15 °

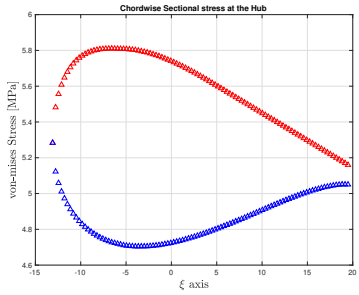

(b) Variation of the von-Mises stress at the hub of the propeller - β_0 = 22.5 °

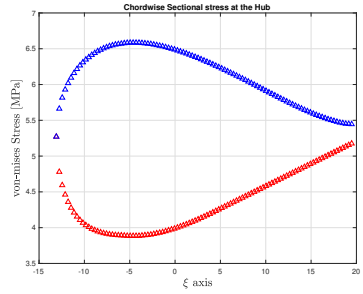

(c) Variation of the von-Mises stress at the hub of the propeller - β_0 = 30 °

Figure 5.12: Variation of the hub stress with varying propeller pitch

increases towards the tip of blade as seen in the figure 5.13b. On the pressure side, the stress is significantly lower than the suction side and remains fairly uniform along the surface. The pressure side remains with low stress as the centrifugal tensile stresses are neutralized with the compressive stresses due to bending moments as seen in the figure 5.13a.

As the propeller pitch is increased to β_0 = 22.5 °, maximum von-Mises stress decreases to 13.5 MPa, occurring on the suction side as well (figure 5.13d), at similar radial section and diminishing towards the tip of blade. Pressure side of blade is seen in the figure 5.13d, which remains fairly uniform with lower stresses, in the center, but still an increase in stress as compared to previous case can be observed on suction side.

For further higher propeller pitch β_0 = 30 °, maximum von-Mises stress rises to 17 MPa as the propeller changes its regime to propulsive. Unlike other two cases, maximum stress occurs on the pressure side (figure 5.13e), at a radial section of 40 % and stress diminishing towards the tip. It is interesting to observe the suction side as well in figure 5.13f, where the stress varies from trailing edge to leading edge, however slight rise and a stress concentration zone near the trailing edge is also observed. Aerodynamic moments are higher than the previous case, resulting in the compressive stress on suction side, which are neutralized by the direct centrifugal tensile stress.

Overall stress remains tensile in nature as no 'neutral' axis is observed of zero stress, and therefore, the centrifugal direct stresses (tensile) dominates over the bending stresses (compressive on one side and tensile on other) due to aerodynamic loads. This implies that propeller in these cases were also dominated by the centrifugal loads.

Appendix C contains the propeller blade stress contours for all reference pitch angle ranging from 15 ° to 30 °.

5.3. Varying Sweep Angle

The sweep is implemented on the propeller blades to achieve a better aeroacoustic performance. Before employing a low-fidelity model into a design optimization, it is crucial to ensure that it is functioning satisfactorily for the swept propeller blades. Therefore, sweep of the blade γ_0 is varied in the final part of the analysis, and the effect on the von-Mises stresses is observed. Comparison is done while maintaining the propeller's operating conditions; the advance ratio J is set to 1.2 , the reference pitch is set to 30 °, and the airspeed is set to 30 m/s. The sweep at the tip of the blade (γ_0) varies from 0 ° to 25 °. It is important to note that the correct aerodynamic loads for the swept blades from the low fidelity model was not available; thus, aerodynamic loads corresponding to straight blades are used to evaluate stress which were distributed over the radial sections at certain sweep. As a result, the main goal of this section is to predict correct trends with a higher sweep in the blade rather than exact stress values.

$$\gamma(r) = \frac{\gamma_0}{2}\left(3\left(\frac{r-R}{R_H-R}\right)^2 - \left(\frac{r-R}{R_H-R}\right)^3\right) \tag{5.1}$$

The centroid of each radial section is now present at a specified offset from the reference section, given by MCA from the equation 2.19, and do not lie on the same axis, which signifies that as the sweep angle grows, a centrifugal bending moment that was not present in any of the previously stated examples would develop. Sweep distribution of blade is defined according to the equation 5.1, where γ_0 is the value of sweep at the propeller tip, R is the tip radius, R_H being the hub radius and r being the section where sweep is distributed.

As the sweep angle of the blade increases, the centrifugal bending moments also increase, leading to increased von-Mises stress along the blade. Aerodynamic bending moments also varies by a small fraction, as the location of aerodynamic centers changes, resulting in a small change in aerodynamic moments. However, this change is significantly small as compared to the centrifugal bending moments, as the aerodynamic loads are smaller.

Variation of the maximum von-Mises stress along the radial sections with a varied sweep angles is displayed in the figure 5.14. It can be seen that for a highly swept blade, the maximum stress reaches a high value up to 160 MPa, which can be detrimental to the propeller blade and result in a massive disaster for the aircraft. It is critical to keep the stress within a certain range to avoid structural failure of the propeller blade. It should also be noted that these stresses correspond to the blade having structural steel as the propeller material, which is not typical. The use of a lower density material, such

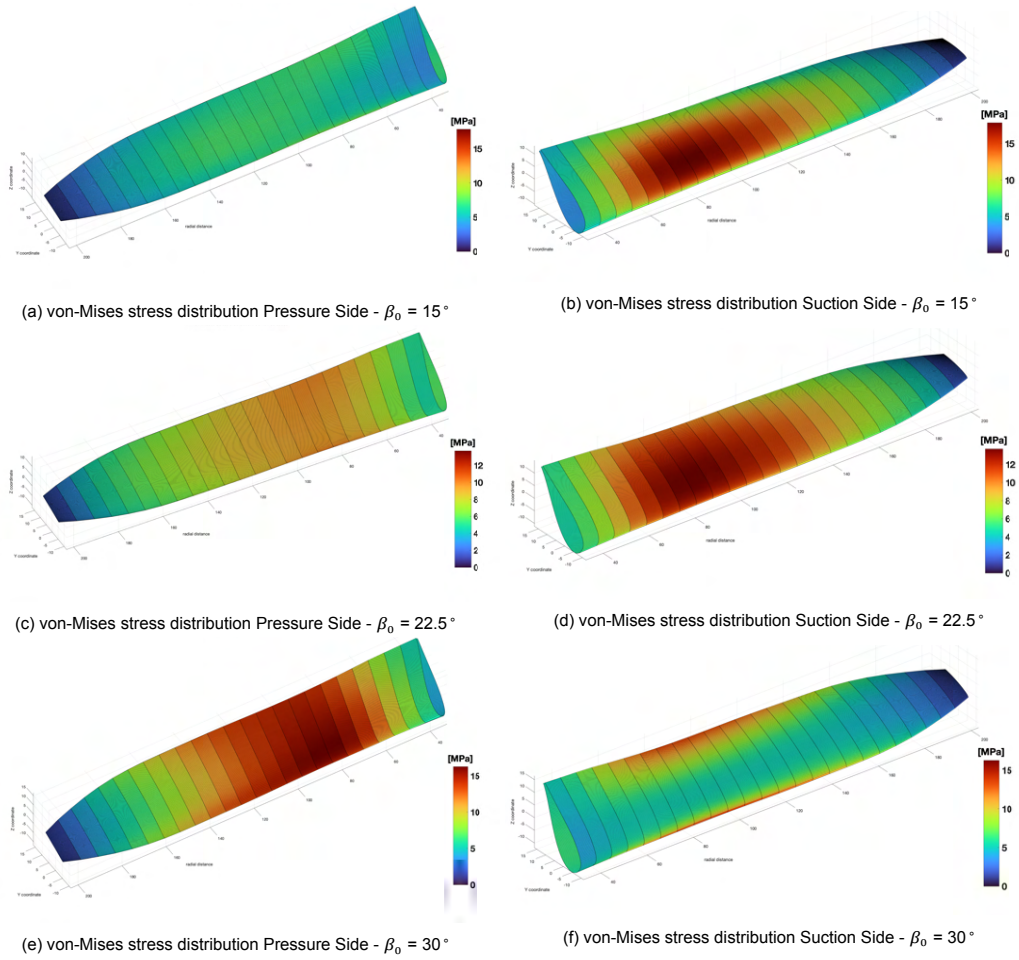

(a) von-Mises stress distribution Pressure Side - β_0 = 15 °

(b) von-Mises stress distribution Suction Side - β_0 = 15 °

(c) von-Mises stress distribution Pressure Side - β_0 = 22.5 °

(d) von-Mises stress distribution Suction Side - β_0 = 22.5 °

(e) von-Mises stress distribution Pressure Side - β_0 = 30 °

(f) von-Mises stress distribution Suction Side - β_0 = 30 °

Figure 5.13: Stress Distribution on the propeller blade with varying propeller pitch β_0

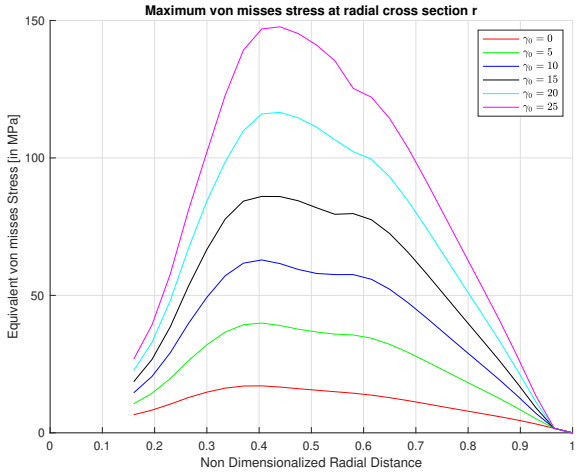

Figure 5.14: Maximum von-Mises stress on radial sections with varying Sweep angle

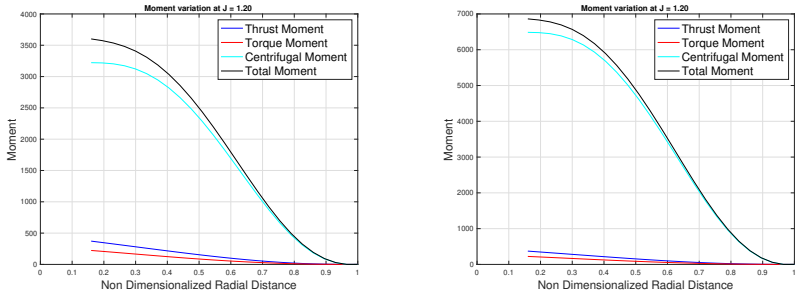

(a) Variation of Global Moments - $\gamma_0 = 10\,°$

(b) Variation of Global Moments

Figure 5.15: Variation of Global Moments with varied sweep γ_0

as titanium, aluminum or carbon fiber, can significantly reduce structural stress up to 30 percent of these values.

In order to understand the flow physics and structural stresses, the cases with sweep of 10 ° and 20 ° are discussed in detail in the following sections.

5.3.1. Global and Local Moments

The figures 5.15 and 5.16 show how the Global and Local moments vary with varying sweep. The presence of centrifugal bending moments, which dominate over aerodynamic moments, is clearly visible in both the cases. The centrifugal moments decrease as the offset between the later airfoil sections and the reference station decreases, as does the centrifugal force acting on the later radial stations. It can be observed that the centrifugal bending moments increases with increase in sweep angle, while the aerodynamic bending moments remains the same as there is no change in the aerodynamic loads. It is evident that centrifugal bending moments dominates over the aerodynamic moments.

Similar to previous cases in propulsive regime, the local moments are negative as seen in figure 5.16; however, the magnitude of the moments is extremely large because the centrifugal moments are higher. It is also observed that in this case, even the torsional moment (shown in green in the plot) can produce a slight higher stress of up to 0.6 MPa.

The figure 5.17 depicts the variation of stress along the hub section with varied sweep. It is observed that the pressure side has higher stresses due to negative local moments, whereas the suction side stress drops to almost zero at 60 percent chordwise distance from the leading edge in the case of $\gamma_0 = 10\,°$ and at 70 percent chordwise distance from the leading edge in the case of $\gamma_0 = 20\,°$. This implies

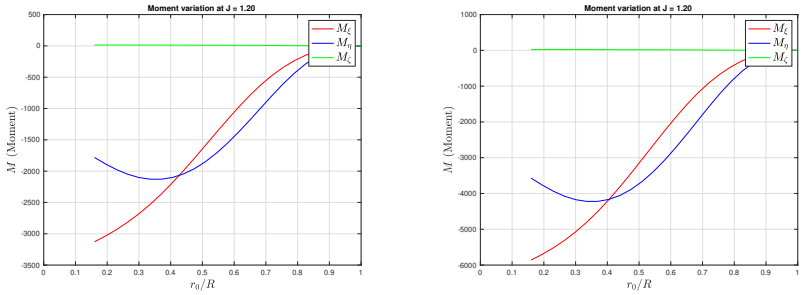

(a) Variation of Local Moments - $\gamma_0 = 10\,°$

(b) Variation of Local Moments

Figure 5.16: Variation of Local Moments with varying sweep $\gamma_0 =$

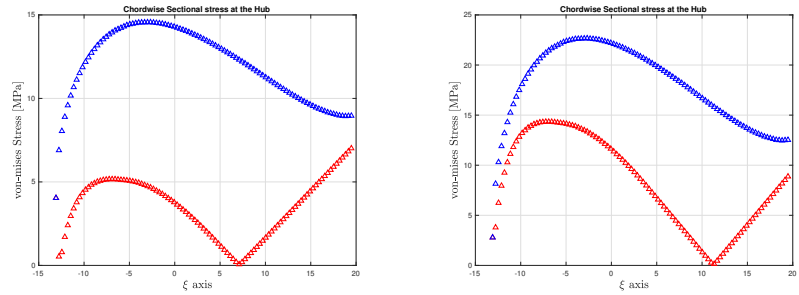

(a) Variation of the von-Mises stress at the hub of the propeller - $\gamma_0 = 10\,°$

(b) Variation of the von-Mises stress at the hub of the propeller - $\gamma_0 = 20\,°$

Figure 5.17: Variation of the hub von-Mises stress in Local axis with sweep

the presence of very high compressive bending stresses, which cancel out the direct centrifugal tensile stress and cause the stress to become zero. The von-Mises stresses on the suction side increase and then decrease, resulting in a local maxima on the suction side. This is because compressive bending stresses dominates over direct centrifugal tensile stresses, and overall stress becomes compressive (negative), as was seen earlier in the case of skewed marine propeller in the figure 2.12; however, in the figure 5.17a the von-Mises stresses are plotted, which changes the sign and plots the magnitude according to the equation 3.28. With an increase in sweep to $\gamma_0 = 20\,°$, profile stress remains relatively similar to the previous case, with amplified stresses on the hub section reaching up to 24 MPa. This is direct result of higher bending moments present in the case of $\gamma_0 = 20\,°$, which results in increase in von-Mises stresses.

The von-Mises stress contour plots are depicted in 5.18. For the case of $\gamma_0 = 10\,°$, maximum stress of 62 MPa is observed on the pressure side of the blade at 40 percent of the radial section. A very high variation of stress on the suction side confirms the presence of a significant amount of bending moment stress in the case. A 'neutral axis' with almost negligible stress is present on the suction side at 60 percent of the chordwise coordinate, which explains why stress is compressive before 60 percent of the chordwise coordinate and tensile after. A stress concentration zone forms at 40 percent of the blade, corresponding to the local maximum caused by compressive stresses.

In case of $\gamma_0 = 20\,°$, maximum stress of 115 MPa is observed on the suction side of the blade at 40 percent of the radial section. A 'neutral axis' with almost negligible stress is present on the suction side at 70 percent of the chordwise coordinate, which explains why stress is compressive before 70 percent of the chordwise coordinate and tensile thereafter. It is worth noting that the maximum von-Mises stress occurs on the suction side of the blade, at 40 percent of the radial section and 30 percent of the chordwise coordinate, which is in a zone dominated by compressive stresses. As a result, it is concluded that bending moments for the present case are so large that the maximum stress in the blade is compressive rather than tensile, and occurs on the suction side of the blade.

It has been established from the results with varying physical parameters that the structural model

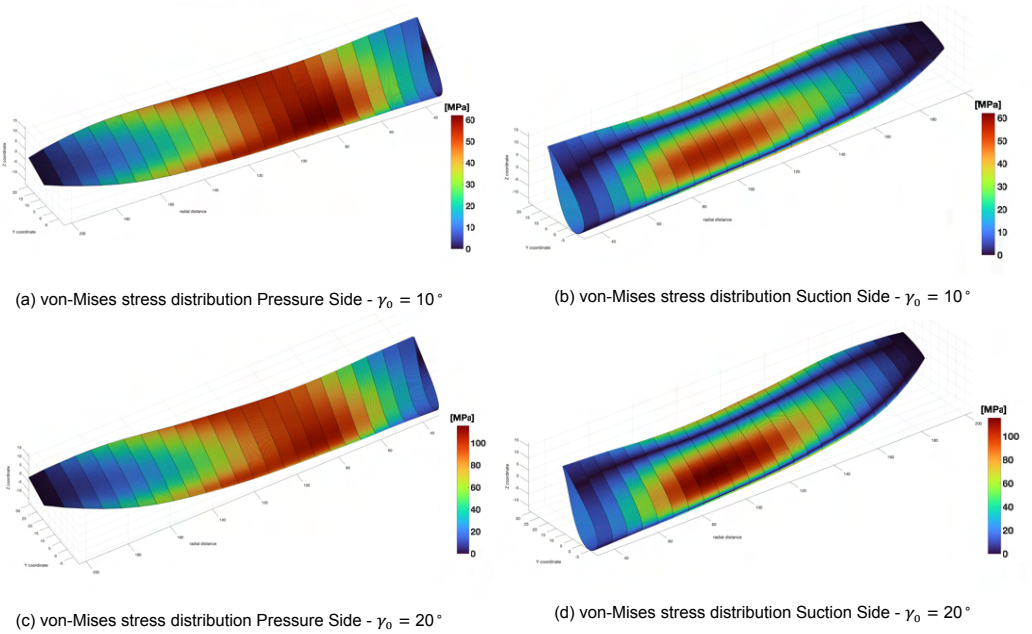

(a) von-Mises stress distribution Pressure Side - $\gamma_0 = 10\,°$

(b) von-Mises stress distribution Suction Side - $\gamma_0 = 10\,°$

(c) von-Mises stress distribution Pressure Side - $\gamma_0 = 20\,°$

(d) von-Mises stress distribution Suction Side - $\gamma_0 = 20\,°$

Figure 5.18: Stress Distribution on the propeller blade with varying sweep

works well with different blade geometries: varying airfoil profile, sweep, and chord of propeller. It is important to note that validation for the swept blades was not performed due to limited resources and time constraints, but varying sweep angles predict uniform trends, indicating that the model works satisfactorily for the swept blades. To be on the safe side, it is recommended to validate the case of swept propeller blades. Appendix D contains the propeller blade stress contours for sweep angle ranging 0 ° to 25 °.

6

Conclusions

Based on the thesis findings, main goals are accomplished and the conclusions are drawn. In this chapter, the conclusions and recommendations for the future studies are presented in the section 6.1 and 6.2 respectively.

6.1. Conclusions

The main goal of the thesis was to quantify the stress on the propeller blade for a general airfoil with varying planform chord, twist, and sweep distribution in order to investigate the structural strength of the propeller. In comparison to a high fidelity FEM model, which can take several minutes, a low fidelity structural model is developed that provides the stress distribution along the propeller in a limited computational time and power (30 s). A mathematical model was proposed for the analysis and design of general propeller blades, which takes the aerodynamic loads from the low fidelity BEM model as input and provides the stress distribution on the blade as output. To account for bending and torsional deformations of the blade, the model is based on Euler-Bernoulli beam theory and Saint-Venant torsion theory respectively. The model treats aerodynamic and inertial loads as static loads. The proposed model can be easily integrated and coupled into the framework of aerodynamics and aeroacoustics, and thus, can be used in the optimization studies to generate optimal propeller blade.

A thorough validation and verification process is carried out, and the low fidelity structural results are compared with high fidelity simulations in order to build some confidence in the low fidelity results. Fluid structure interaction simulations were performed using the one-way coupling method, in which the pressure was imported from the CFD simulations (ANSYS®Fluent) to the FEM simulations (ANSYS®Mechanical). First, the aerodynamic loads from the low fidelity model are evaluated against aerodynamic loads from CFD simulations after post processing. Finally, the structural stresses from low level model and high fidelity FEM simulations are compared. The TUD-XPROP propeller blade was validated in both propulsive and regenerative regimes. Comparisons reveal that the low fidelity model predicts correct trends, underestimating maximum equivalent stresses by 2 percent in the propulsive case and overestimating the maximum equivalent stress by 2.5 percent in regenerative case. It was critical to observe that the model adequately predicts stress due to both inertial loads, and aerodynamic loads.

A sensitivity analysis is also carried out to explore the impact of blade sweep, propeller pitch, and advance ratio on the structural characteristics of isolated propeller blades using a low fidelity structural model. According to the findings of these investigations, as advance ratios grows, the equivalent maximum stress drops. This is a direct outcome of inertial loads, since as advance ratio increases, rotational speed decreases, resulting in lower inertial and aerodynamic loads. It was observed that the centrifugal loads dominates over the aerodynamic loads, at all advance ratios ranging from $J = 0.6$ to 1.2. Additionally, the pitch of the propeller was changed; as the reference pitch angle rises, the maximum stress on the blade first decreases, then tends to rise afterward. This is because aerodynamic loads have changed; at lower pitch angles, the majority of radial stations have a negative angle of attack and are thus operating in a regenerative regime, which causes the maximum stress to initially decrease as pitch rises. The regime changes from regenerative to propulsive as the pitch angles rise,

increasing the angle of attacks at the radial stations as well. This shift in regime causes a change in the direction of aerodynamic loads, raising the maximum stress in the propeller. The impact of the sweep on the propeller blade is later examined. Maximum stresses rise with an increase in sweep angle. The presence of large centrifugal bending moments explains this, which results in high compressible stress on the suction side and high tensile stress on the pressure side. It was concluded that in all the cases observed in the sensitivity study, centrifugal loads dominates over the aerodynamic loads.

6.2. Recommendations

Based on the thesis findings, several recommendations for the future studies are made:

- It may be of interest to check the results for the sweep with correct aerodynamic loads from the low level model and a higher fidelity model using CFD-FEM coupled simulations, which was not possible due to the time constraints of the current project. Finally, an experimental validation would be more useful in establishing a pathway from numerical analysis to final functional prototype.
- This research was carried out for steady rectilinear flight in cruising conditions with constant aerodynamic loads. Before developing a prototype, it is critical to evaluate both the instationary loads in a general flight and the effects of aerodynamic loads during climb and descent operations, where the aircraft operates at non-zero angle of attack.
- Another aspect is during a curved flight path, as the external gyroscopic inertial loads can be present, which has been neglected in the present study. These are time varying sinusoidal loads that can be detrimental for the propeller at very high rotational velocities, which only occurs in the curved flight path.
- The current model did not take the dynamics and aeroelastic stability of the blade into account. Unsteady phenomena such as flight flutter and static divergence must be investigated since they may be detrimental for flight. Along with these analyses, free vibration investigations can be carried out. A separate time domain analysis is required for these studies, which can be performed in the unsteady analysis of the propeller.
- To determine the life cycle of the propeller blades, fatigue investigations must be done. It has been shown in prior examples that a propeller can fail due to fatigue even when there is no irregularity or extreme vibration in flight, as in the case of Muhammad et al. [38]. This is due to fatigue induced after a number of cycles of use, which eventually led to crack initiation and propeller blade failure
- To obtain a propeller blade geometry with optimal aerodynamic and aeroacoustic performance, the proposed structural model must be implemented and combined with an aerodynamic and aeroacoustic framework. Optimization studies must be carried out in order to determine the optimal propeller blade geometry that can withstand aerodynamic and inertial loads.

Bibliography

[1] Robert Peterson. “Regional Turboprop resurgence continues; Jet demand shifts upward”. In: *Aircraft Engineering and Aerospace Technology* 80.2 (2008). DOI: 0.1108/aeat.2008.12780baf.008. URL: https://doi.org/10.1108/aeat.2008.12780baf.008.

[2] LLM Veldhuis. “Review of propeller-wing aerodynamic interference. ICAS 2004-6.3.1”. Undefined/Unknown. In: *24th International Congress of the Aeronautical Sciences, Yokohama, Japan*. 2004.

[3] John T. Bonet et al. “Environmentally Responsible Aviation (ERA) Project - N+2 Advanced Vehicle Concepts Study and Conceptual Design of Subscale Test Vehicle (STV) Final Report”. In: 2011.

[4] Advisory Council for Aviation Research and Innovation in Europe (ACARE). *Realising Europe’s vision for aviation: Strategic research & innovation agenda*. 2020.

[5] Benjamin J. Brelje and Joaquim R.R.A. Martins. “Electric, hybrid, and turboelectric fixed-wing aircraft: A review of concepts, models, and design approaches”. In: *Progress in Aerospace Sciences* 104 (2019), pp. 1–19. ISSN: 0376-0421. DOI: https://doi.org/10.1016/j.paerosci.2018.06.004. URL: https://www.sciencedirect.com/science/article/pii/S0376042118300356.

[6] Mark D. Guynn et al. “Advanced Single-Aisle Transport Propulsion Design Options Revisited”. In: *2013 Aviation Technology, Integration, and Operations Conference*. DOI: 10.2514/6.2013-4330. eprint: https://arc.aiaa.org/doi/pdf/10.2514/6.2013-4330. URL: https://arc.aiaa.org/doi/abs/10.2514/6.2013-4330.

[7] Wouter de Haan. “Impact of Blade Sweep on Aerodynamic and Aeroacoustic Performance Optimization of Isolated Propellers”. English. In: 2021. URL: https://tudelft.on.worldcat.org/oclc/1267972217.

[8] Stijn Burger. “Multi-Fidelity Aerodynamic and Aeroacoustic Sensitivity Study of Isolated Propellers”. English. In: 2020. URL: http://resolver.tudelft.nl/uuid:7abef8ee-c15c-4e36-ade6-33daa3262386.

[9] Timo Keil. “A sensitivity study on the effect of blade sweep on the trade-off between propeller efficiency and noise with panel method analysis”. English. In: 2021. URL: http://resolver.tudelft.nl/uuid:39e67ba0-3409-4069-be3e-f1f12443a9ff.

[10] Antonio Pagano et al. “Multi-Objective Aeroacoustic Optimization of an Aircraft Propeller”. In: *12th AIAA/ISSMO Multidisciplinary Analysis and Optimization Conference*. 2008. DOI: 10.2514/6.2008-6059. eprint: https://arc.aiaa.org/doi/pdf/10.2514/6.2008-6059. URL: https://arc.aiaa.org/doi/abs/10.2514/6.2008-6059.

[11] Fred E Weick. *Aircraft propeller design*. eng. New York: McGraw-Hill, 1930. ISBN: 993-010410-0.

[12] Tomas Sinnige et al. “Aerodynamic Performance of a Wingtip-Mounted Tractor Propeller Configuration in Windmilling and Energy-Harvesting Conditions”. In: *AIAA Aviation 2019 Forum*. 2019. DOI: 10.2514/6.2019-3033. eprint: https://arc.aiaa.org/doi/pdf/10.2514/6.2019-3033. URL: https://arc.aiaa.org/doi/abs/10.2514/6.2019-3033.

[13] Tomas Sinnige. “Aerodynamic and Aeroacoustic Interaction Effects for Tip-Mounted Propellers: An Experimental Study”. English. PhD thesis. Delft University of Technology, 2018. ISBN: 978-94-9301-446-6. DOI: 10.4233/uuid:214e1e9a-c53e-47c7-a12c-b1eb3ec8293b.

[14] Jatinder Goyal et al. “Aerodynamic and Aeroacoustic Characteristics of an Isolated Propeller at Positive and Negative Thrust”. In: *AIAA AVIATION 2021 FORUM*. 2021. DOI: 10.2514/6.2021-2187. eprint: https://arc.aiaa.org/doi/pdf/10.2514/6.2021-2187. URL: https://arc.aiaa.org/doi/abs/10.2514/6.2021-2187.

[15] David Erzen, Matej Andrejasic, and Tadej Kosel. “An Optimal Propeller Design for In-Flight Power Recuperation on an Electric Aircraft”. In: *2018 Aviation Technology, Integration, and Operations Conference*. DOI: 10.2514/6.2018-3206. eprint: https://arc.aiaa.org/doi/pdf/10.2514/6.2018-3206. URL: https://arc.aiaa.org/doi/abs/10.2514/6.2018-3206.

[16] JS Carlton. “8 - Theoretical methods ‚Äì propeller theories”. In: *Marine Propellers and Propulsion (Second Edition)*. Ed. by JS Carlton. Second Edition. Oxford: Butterworth-Heinemann, 2007, pp. 168–204. ISBN: 978-0-7506-8150-6. DOI: https://doi.org/10.1016/B978-075068150-6/50010-3. URL: https://www.sciencedirect.com/science/article/pii/B9780750681506500103.

[17] Xin Geng et al. “Analysis of Thrust-Scaled Acoustic Emissions of Aircraft Propellers and Their Dependence on Propulsive Efficiency”. English. In: *32nd Congress of the International Council of the Aeronautical Sciences*. ICAS 2021. 32nd Congress of the International Council of the Aeronautical Sciences, ICAS 2021 ; Conference date: 06-09-2021 Through 10-09-2021. International Council of the Aeronautical Sciences, 2021.

[18] Xinqiang Liu and Weiliang He. “Performance Calculation and Design of Stratospheric Propeller”. In: *IEEE Access* 5 (2017), pp. 14358–14368.

[19] Donald B. Hanson. “Helicoidal Surface Theory for Harmonic Noise of Propellers in the Far Field”. In: *AIAA Journal* 18.10 (1980), pp. 1213–1220. DOI: 10.2514/3.50873. URL: https://doi.org/10.2514/3.50873.

[20] B. Magliozzi. “Noise characteristics of model counter-rotating Prop-Fans”. In: *11th Aeroacoustics Conference*. 2012. DOI: 10.2514/6.1987-2656. eprint: https://arc.aiaa.org/doi/pdf/10.2514/6.1987-2656. URL: https://arc.aiaa.org/doi/abs/10.2514/6.1987-2656.

[21] O. Gur and A. Rosen. “Comparison between blade-element models of propellers”. In: *The Aeronautical Journal (1968)* 112.1138 (2008), pp. 689–704. DOI: 10.1017/S0001924000002669.

[22] Jacob Willem Cohen. “On stress calculations in helicoidal shells and propeller blades”. In: (1955).

[23] JE Conolly. “Strength of propellers.” In: *Trans RINA* 103 (1974), pp. 139–204.

[24] James H Ma. “Stresses in marine propellers”. In: *Journal of Ship Research* 18.04 (1974), pp. 252–264.

[25] P Atkinson. “PREDICTION OF MARINE PROPELLER DISTORTION AND STRESSES USING A SUPERPARAMETERIC THICK-SHELL FINITE-ELEMENT MODEL”. In: *Royal Institution of Naval Architects Suppl Papers* 115 (1973).

[26] JS Carlton. “Marine propeller blade stresses”. In: *Transactions (TM)—Institute of Marine Engineers* 96.63 (1984).

[27] 18th Proc. ITTC. *Report of Propulsor Committee*. 1987.

[28] Jurij Sodja et al. “Design of Flexible Propellers with Optimized Load-Distribution Characteristics”. In: *Journal of Aircraft* 51.1 (2014), pp. 117–128. DOI: 10.2514/1.C032131. eprint: https://doi.org/10.2514/1.C032131. URL: https://doi.org/10.2514/1.C032131.

[29] R. MacNeill. “Optimisation of Propellers for UAV Powertrains”. eng. In: *53rd AIAA/SAE/ASEE Joint Propulsion Conference, Atlanta, GA, July 10,Äê12, 2017*. American Institute of Aeronautics and Astronautics, 2017, pp. 1–1. ISBN: 1624105114.

[30] Raymond J Roark et al. *Roark’s formulas for stress and strain*. eng. 8th ed. McGraw-Hill’s AccessEngineering. New York: McGraw-Hill, 2012. ISBN: 9780071742474.

[31] Russel C Hibbeler. *Mechanics of materials*. eng. 3. ed.. Upper Saddle River, N.J.: Prentice Hall, 1997. ISBN: 0-13-256983-3.

[32] Kirad Abdelkader, Zebbiche Toufik, and Boun-jad Mohamed. “Torsional stress in non-circular cross sections by the finite element method”. In: *Advances in Mechanical Engineering* 7.5 (2015), p. 1687814015581979. DOI: 10.1177/1687814015581979. eprint: https://doi.org/10.1177/1687814015581979. URL: https://doi.org/10.1177/1687814015581979.

[33] J. N. (Junuthula Narasimha) Reddy. *An introduction to the finite element method*. eng. 3. ed.. McGraw-Hill series in mechanical engineering. Boston: McGraw-Hill, 2006. ISBN: 0-07-246685-5.

[34] Snorri Gudmundsson. “Chapter 8 - The Anatomy of the Airfoil”. In: *General Aviation Aircraft Design*. Ed. by Snorri Gudmundsson. Boston: Butterworth-Heinemann, 2014, pp. 235–297. ISBN: 978-0-12-397308-5. DOI: https://doi.org/10.1016/B978-0-12-397308-5.00008-8. URL: https://www.sciencedirect.com/science/article/pii/B9780123973085000088.

[35] Tom C. A. Stokkermans et al. “Validation and Comparison of RANS Propeller Modeling Methods for Tip-Mounted Applications”. In: *AIAA Journal* 57.2 (2019), pp. 566–580. DOI: 10.2514/1.J057398. eprint: https://doi.org/10.2514/1.J057398. URL: https://doi.org/10.2514/1.J057398.

[36] P. SPALART and S. ALLMARAS. “A one-equation turbulence model for aerodynamic flows”. In: *30th Aerospace Sciences Meeting and Exhibit*. DOI: 10.2514/6.1992-439. eprint: https://arc.aiaa.org/doi/pdf/10.2514/6.1992-439. URL: https://arc.aiaa.org/doi/abs/10.2514/6.1992-439.

[37] Jennifer Dacles-Mariani et al. “Numerical/experimental study of a wingtip vortex in the near field”. In: *AIAA Journal* 33.9 (1995), pp. 1561–1568. DOI: 10.2514/3.12826. eprint: https://doi.org/10.2514/3.12826. URL: https://doi.org/10.2514/3.12826.

[38] Mohd Moesli Muhammad et al. “FRACTURE FAILURE ANALYSIS OF A MARINE PROPELLER SHAFT”. In: *Defence S and T Technical Bulletin* 13 (Oct. 2020), pp. 240–246.

A

Blade Cross sections

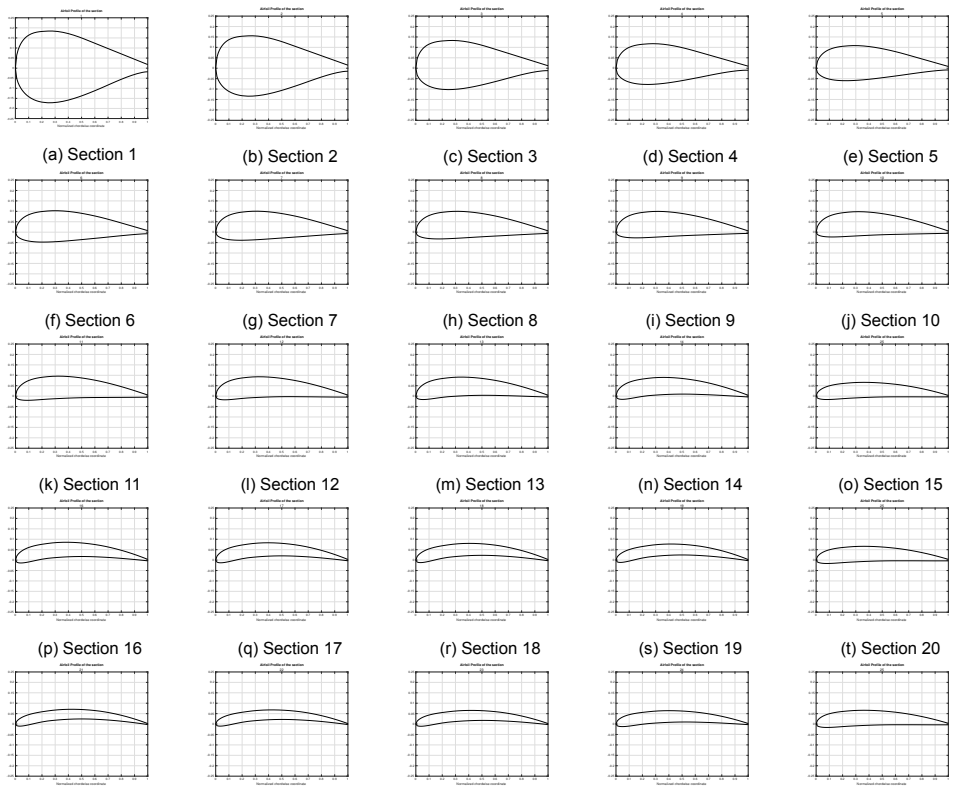

(a) Section 1 (b) Section 2 (c) Section 3 (d) Section 4 (e) Section 5

(f) Section 6 (g) Section 7 (h) Section 8 (i) Section 9 (j) Section 10

(k) Section 11 (l) Section 12 (m) Section 13 (n) Section 14 (o) Section 15

(p) Section 16 (q) Section 17 (r) Section 18 (s) Section 19 (t) Section 20

(u) Section 21 (v) Section 22 (w) Section 23 (x) Section 24 (y) Section 25

Figure A.1: Blade cross sections at 25 radial sections of XPROP propeller (untwisted)

B

Sensitivity Results Contour plots: Advance Ratio

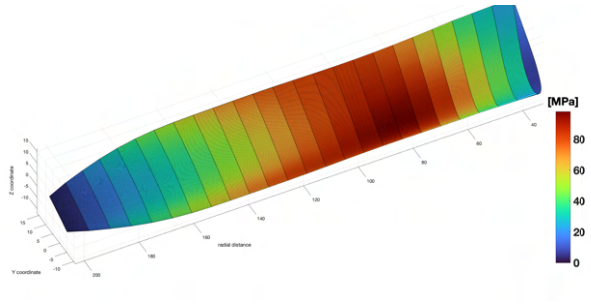

(a) Pressure Side : $J = 0.6$

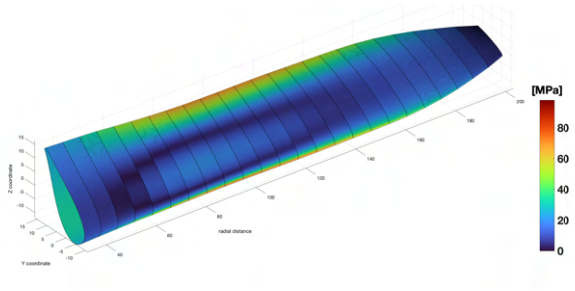

(b) Suction Side : $J = 0.6$

Figure B.1: von-Mises stress contours with $J = 0.6$

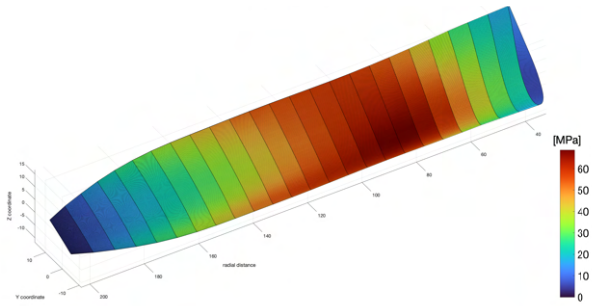

(a) Pressure Side : $J = 0.7$

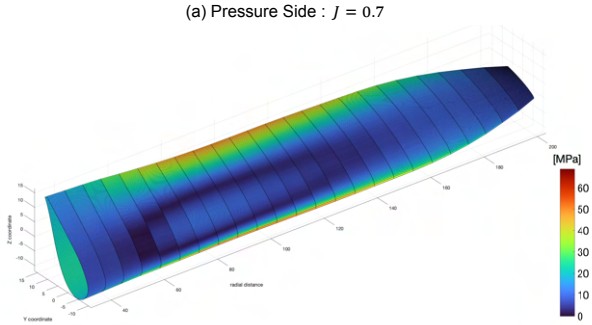

(b) Suction Side : $J = 0.7$

Figure B.2: von-Mises stress contours with $J = 0.7$

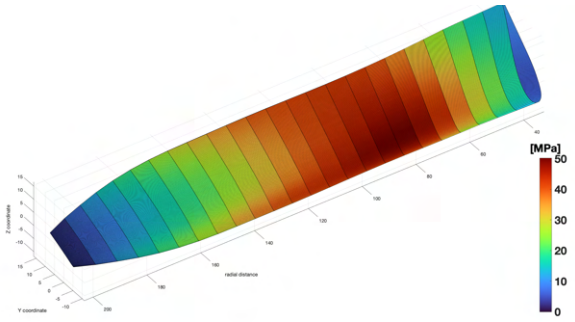

(a) Pressure Side : $J = 0.8$

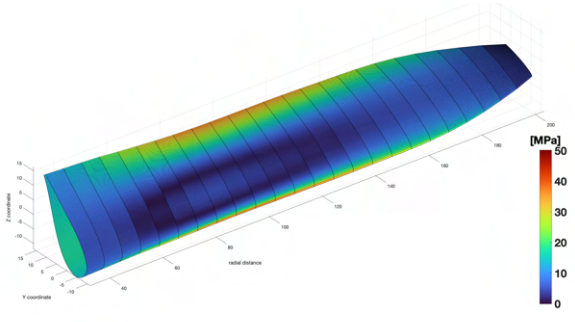

(b) Suction Side : $J = 0.8$

Figure B.3: von-Mises stress contours with $J = 0.8$

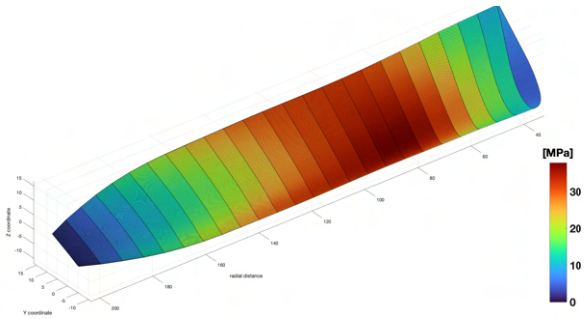

(a) Pressure Side : $J = 0.9$

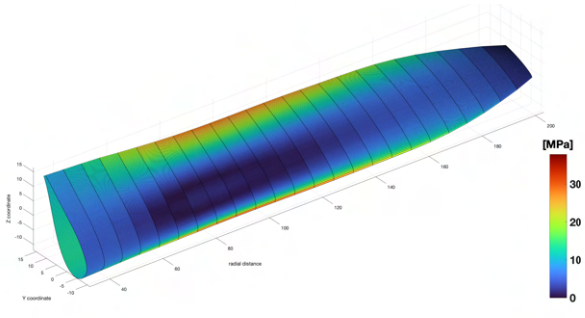

(b) Suction Side : $J = 0.9$

Figure B.4: von-Mises stress contours with $J = 0.9$

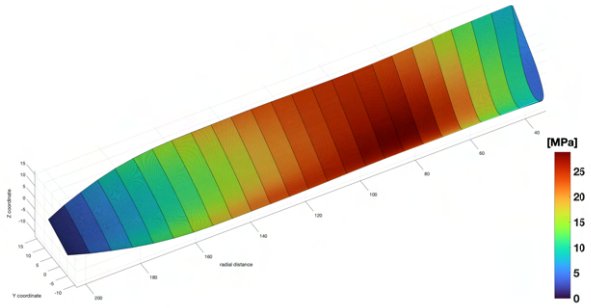

(a) Pressure Side : $J = 1.0$

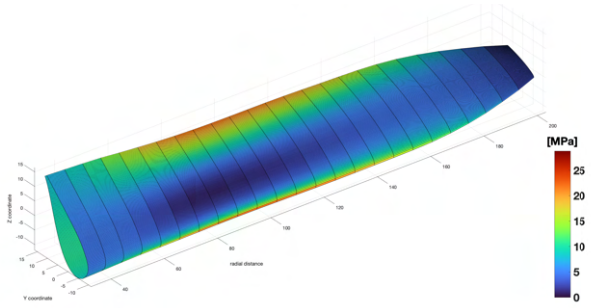

(b) Suction Side : $J = 1.0$

Figure B.5: von-Mises stress contours with $J = 1.0$

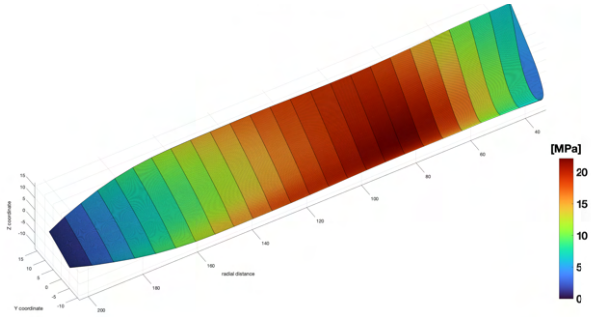

(a) Pressure Side : $J = 1.1$

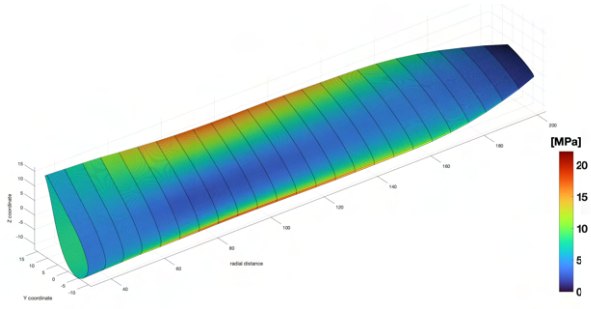

(b) Suction Side : $J = 1.1$

Figure B.6: von-Mises stress contours with $J = 1.1$

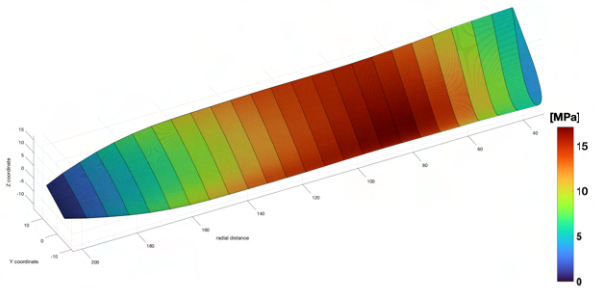

(a) Pressure Side : $J = 1.2$

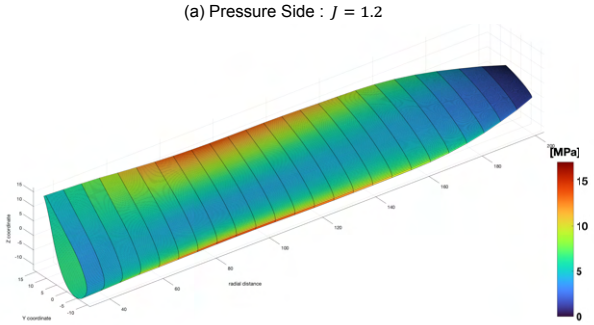

(b) Suction Side : $J = 1.2$

Figure B.7: von-Mises stress contours with $J = 1.2$

C

Sensitivity Results Contour plots: Propeller Pitch

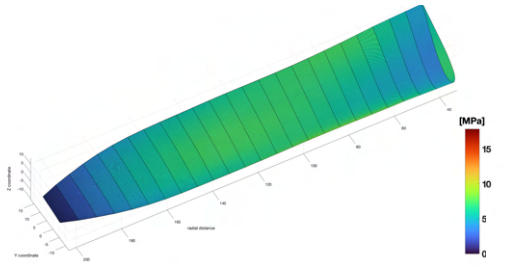

(a) Pressure Side : $\beta_0 = 15$

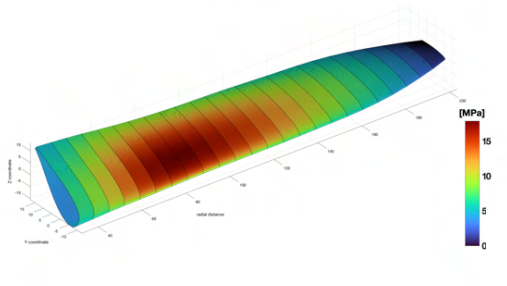

(b) Suction Side : $\beta_0 = 15$

Figure C.1: von-Mises stress contours with $\beta_0 = 15$

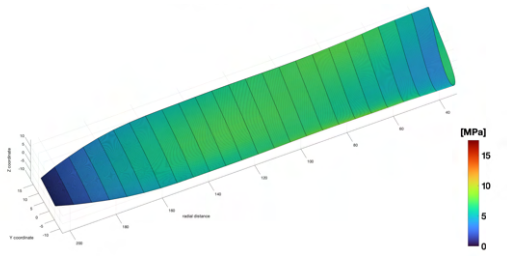

(a) Pressure Side : $\beta_0 = 17.5$

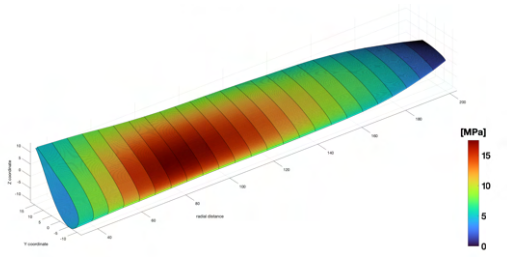

(b) Suction Side : $\beta_0 = 17.5$

Figure C.2: von-Mises stress contours with $\beta_0 = 17.5$

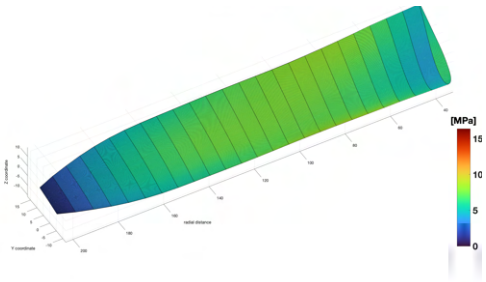

(a) Pressure Side : $\beta_0 = 20$

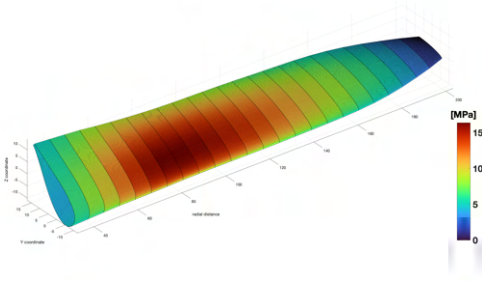

(b) Suction Side : $\beta_0 = 20$

Figure C.3: von-Mises stress contours with $J = 20$

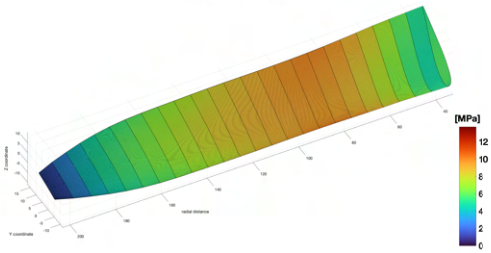

(a) Pressure Side : $\beta_0 = 22.5$

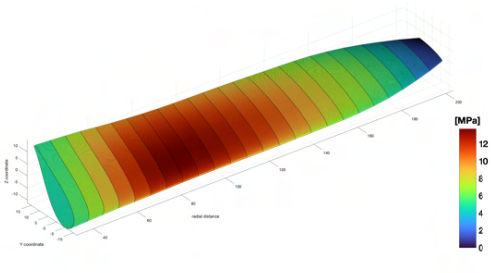

(b) Suction Side : $\beta_0 = 22.5$

Figure C.4: von-Mises stress contours with $\beta_0 = 22.5$

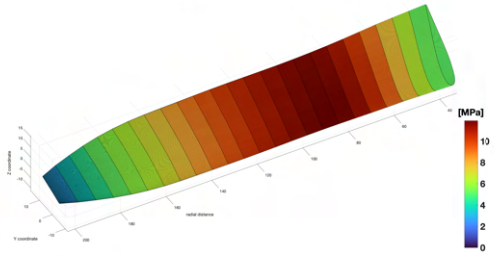

(a) Pressure Side : $\beta_0 = 25$

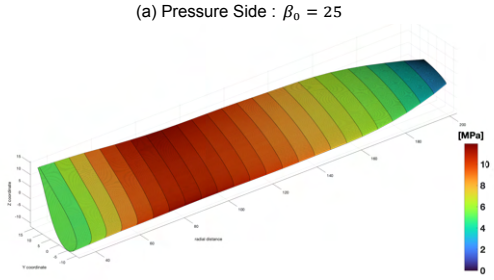

(b) Suction Side : $\beta_0 = 25$

Figure C.5: von-Mises stress contours with $\beta_0 = 25$

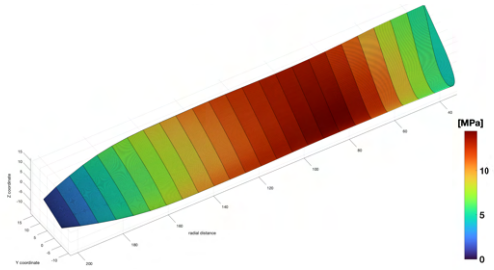

(a) Pressure Side : $\beta_0 = 27.5$

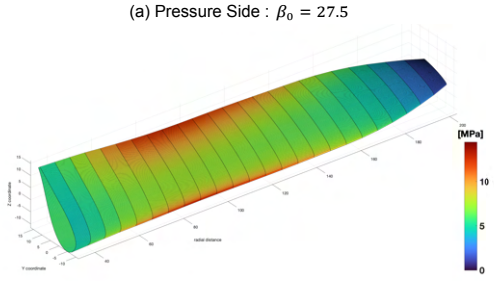

(b) Suction Side : $\beta_0 = 27.5$

Figure C.6: von-Mises stress contours with $\beta_0 = 27.5$

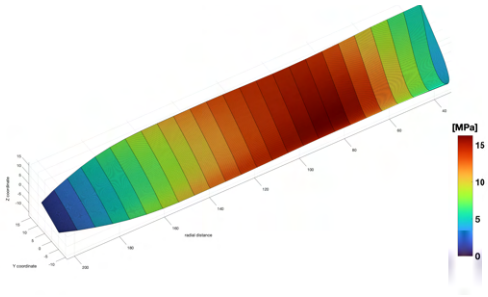

(a) Pressure Side : $\beta_0 = 30$

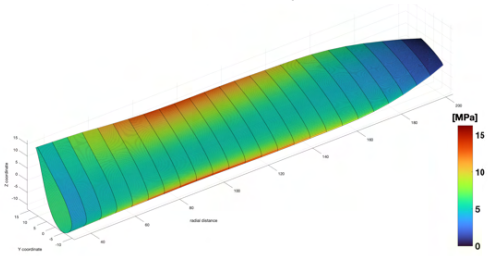

(b) Suction Side : $\beta_0 = 30$

Figure C.7: von-Mises stress contours with $\beta_0 = 30$

D

Sensitivity Results Contour plots: Blade Sweep

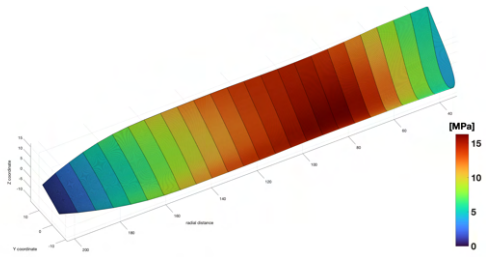

(a) Pressure Side : $\gamma_0 = 0$

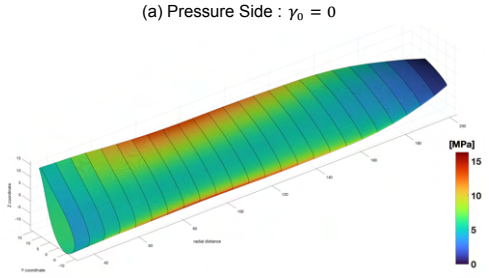

(b) Suction Side : $\gamma_0 = 0$

Figure D.1: von-Mises stress contours with $\gamma_0 = 0$

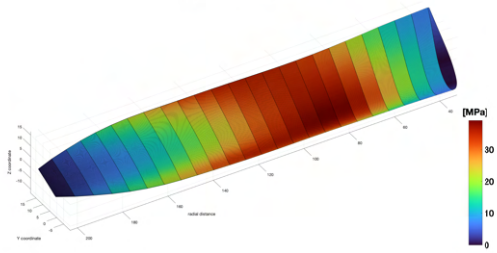

(a) Pressure Side : $\gamma_0 = 5$

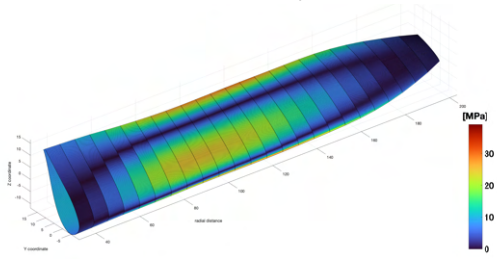

(b) Suction Side : $\gamma_0 = 5$

Figure D.2: von-Mises stress contours with $\gamma_0 = 5$

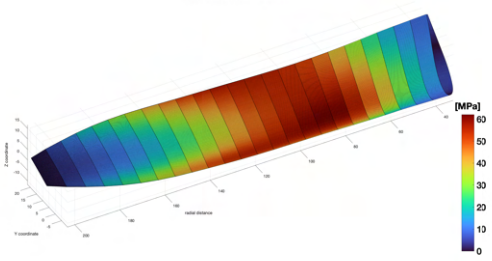

(a) Pressure Side : $\gamma_0 = 10$

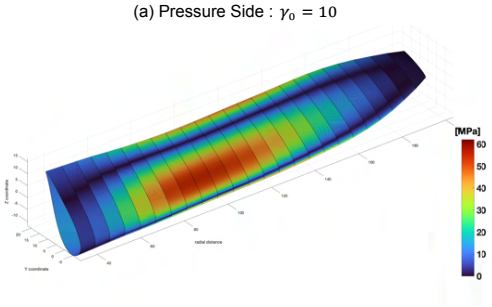

(b) Suction Side : $\gamma_0 = 10$

Figure D.3: von-Mises stress contours with $\gamma_0 = 10$

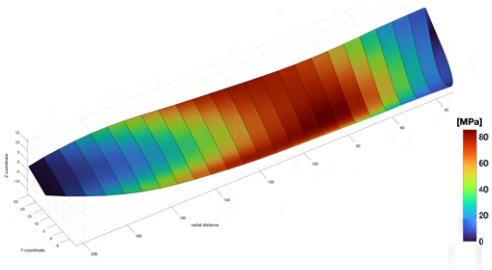

(a) Pressure Side : $\gamma_0 = 15$

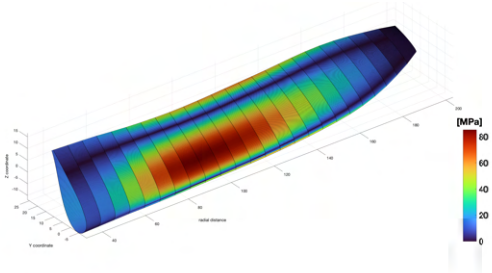

(b) Suction Side : $\gamma_0 = 15$

Figure D.4: von-Mises stress contours with $\gamma_0 = 15$

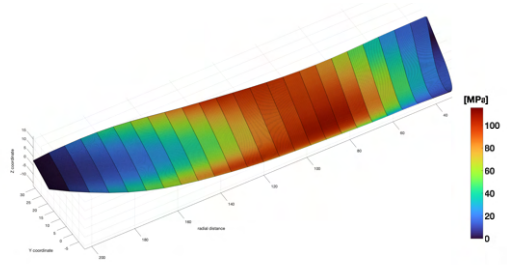

(a) Pressure Side : $\gamma_0 = 20$

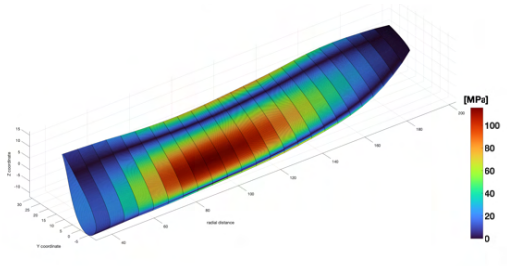

(b) Suction Side : $\gamma_0 = 20$

Figure D.5: von-Mises stress contours with $\gamma_0 = 20$

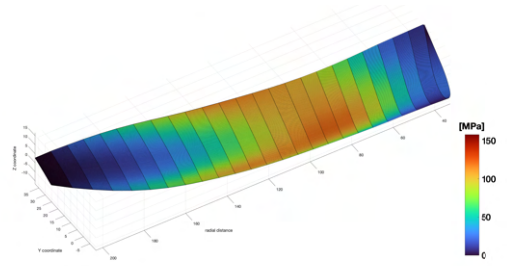

(a) Pressure Side : $\gamma_0 = 25$

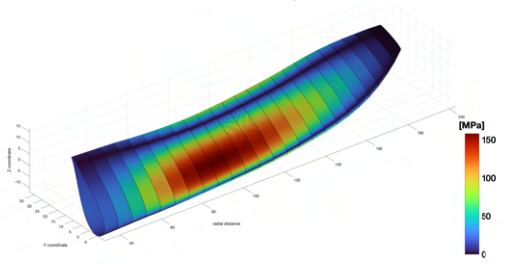

(b) Suction Side : $\gamma_0 = 25$

Figure D.6: von-Mises stress contours with $\gamma_0 = 25$

E

Post Processing Python Script with TecPlot ®

```
##############################################################################
## Author - Jatinder Goyal (j.goyal@tudelft.nl)
##############################################################################
import pandas as pd
import tecplot as tp
from pylab import *
from tecplot.constant import *
from scipy.integrate import simps

##############################################################################
def ActiveFieldMap(str):
    rg = tp.active_frame().plot().num_fieldmaps
    fdMaps = tuple(range(rg))
    bladeSurface = [tp.active_frame().dataset.zone(name) for name in [str]]
    tp.active_frame().plot().fieldmaps(fdMaps).show = False
    tp.active_frame().plot().fieldmaps(bladeSurface).show = True
    tp.macro.execute_command('$!RedrawAll')
    tp.active_frame().plot().view.psi = 0
    tp.active_frame().plot().view.theta = 0
    tp.macro.execute_command('$!RedrawAll')
    tp.active_frame().plot().view.fit_data(consider_blanking=True)


# End Macro.

# Uncomment the following line to connect to a running instance of Tecplot 360:
tp.session.connect()
Rp = 0.2032  # propeller Radius[m]

# J = np.array([0.60,0.75,1.10,1.20,1.40,1.90]) #AdvanceRatio
# pitch = np.array([15,15,15,30,30,30]) # pitch angle [deg]
# V     = np.array([30,30,30,30,30,30]) # freestream velocity[m/s]
# B     = np.array([3,3,3,3,3,3]) #No. of blades [-]

J = np.array([1.20])
pitch = np.array([30])
V = np.array([30])
B = np.array([3])

min_rR = 0.195
max_rR = 0.999
rR_n = 24
outputFile = '../DataOutput/ThrustTorque_perBlade_J{:.2f}V{}B{}pitch{}.csv'

casFile = '../J{:.2f}_V{}B{}pitch{}/J{:.2f}_V{}B{}pitch{}-2.cas'
datFile = '../J{:.2f}_V{}B{}pitch{}/J{:.2f}_V{}B{}pitch{}-2-10000.dat'
for j in range(len(J)):
```

```
    ## Load CFD Data
    tp.data.load_fluent(case_filenames=[casFile.format(J[j], V[j], B[j], pitch[j], J[j], V[j],
B[j], pitch[j])],
                        data_filenames=[datFile.format(J[j], V[j], B[j], pitch[j], J[j], V[j],
B[j], pitch[j])],
                        append=False)

    ## Define variables needed for post-processing
    tp.data.operate.execute_equation(equation='{{R}} = {:f}'.format(Rp),
                                     value_location=ValueLocation.Nodal)
    tp.data.operate.execute_equation(equation='{x/R<sub>p</sub>} = {X}/{R}',
                                     value_location=ValueLocation.Nodal)
    tp.data.operate.execute_equation(equation='{y/R<sub>p</sub>} = {Y}/{R}',
                                     value_location=ValueLocation.Nodal)
    tp.data.operate.execute_equation(equation='{z/R<sub>p</sub>} = {Z}/{R}',
                                     value_location=ValueLocation.Nodal)

    # Assign Non-dimensionalised coordinate system
    tpplot = tp.active_frame().plot()
    tpplot.axes.x_axis.variable = tp.active_frame().dataset.variable("x/R<sub>p</sub>")
    tpplot.axes.y_axis.variable = tp.active_frame().dataset.variable("y/R<sub>p</sub>")
    tpplot.axes.z_axis.variable = tp.active_frame().dataset.variable("z/R<sub>p</sub>")
    tpplot.view.magnification = 0.9
    tp.macro.execute_command('$!RedrawAll')

    ## Select Active domains for the slicing
    ActiveFieldMap('blade_pressure')
    sliceP = []
    for y in np.linspace(min_rR, max_rR, rR_n):
        slice = tp.data.extract.extract_slice(
            origin=(0, y, 0),
            normal=(0, 1, 0),
            source=tp.constant.SliceSource.SurfaceZones,
            dataset=tp.active_frame().dataset)

        slice.name = 'blade_P: r/R={}'.format(y)
        sliceP.append(slice)

    ###############################################################################################
    ActiveFieldMap('blade_suction')
    sliceS = []
    for y in np.linspace(min_rR, max_rR, rR_n):
        slice = tp.data.extract.extract_slice(
            origin=(0, y, 0),
            normal=(0, 1, 0),
            source=tp.constant.SliceSource.SurfaceZones,
            dataset=tp.active_frame().dataset)

        slice.name = 'blade_S: r/R={}'.format(y)
        sliceS.append(slice)
    ###############################################################################################
    ActiveFieldMap('blade_te')
    sliceT = []
    for y in np.linspace(min_rR, max_rR, rR_n):
        slice = tp.data.extract.extract_slice(
            origin=(0, y, 0),
            normal=(0, 1, 0),
            source=tp.constant.SliceSource.SurfaceZones,
            dataset=tp.active_frame().dataset)

        slice.name = 'blade_TE: r/R={}'.format(y)
        sliceT.append(slice)

    thrust = []
    torque = []
    rR = []
    for y in range(len(sliceP)):
        # for y in [40]:

        x_P = sliceP[y].values('X').as_numpy_array()
        idx_P = np.argsort(x_P)
```

```
        x_P = x_P[idx_P]
        z_P = sliceP[y].values('Z').as_numpy_array()[idx_P]
        y_P = sliceP[y].values('y/R<sub>p</sub>').as_numpy_array()[idx_P]
        P_P = sliceP[y].values('Pressure').as_numpy_array()[idx_P]
        ST_P = sliceP[y].values('Wall Shear Stress').as_numpy_array()[idx_P]

        z_S = sliceS[y].values('Z').as_numpy_array()
        idx_S = np.argsort(z_S)
        z_S = z_S[idx_S]
        x_S = sliceS[y].values('X').as_numpy_array()[idx_S]
        P_S = sliceS[y].values('Pressure').as_numpy_array()[idx_S]
        ST_S = sliceS[y].values('Wall Shear Stress').as_numpy_array()[idx_S]

        x_T = sliceT[y].values('X').as_numpy_array()
        z_T = sliceT[y].values('Z').as_numpy_array()
        P_T = sliceT[y].values('Pressure').as_numpy_array()
        ST_T = sliceT[y].values('Wall Shear Stress').as_numpy_array()

        T = simps(P_P,z_P) - simps(P_S,z_S) - simps(P_T,z_T)
                - simps(ST_P,x_P) - simps(ST_S,x_S)- simps(ST_T,x_T)
        Q = (simps(P_P,x_P) - simps(P_S,x_S) - simps(P_T,x_T)
                + simps(ST_P, z_P) + simps(ST_S, z_S) + simps(ST_T,z_T))*y_P[1]*Rp
        thrust.append(T)
        torque.append(Q)
        rR.append(y_P[1])

    df = pd.DataFrame(data={"r_R": rR, "T": thrust, "Q": torque})
    df.to_csv(outputFile.format(J[j], V[j], B[j], pitch[j]), sep=',',index=False)
```